(4)

Applied Research Laboratory

Technical Report

THE STRUCTURE OF REYNOLDS STRESS
IN THE NEAR WALL REGION OF A
TURBULENT PIPE FLOW

by

Paul Chevrin
Howard Petrie
Steven Deutsch

PENNSTATE

1855

(4)

The Pennsylvania State University
APPLIED RESEARCH LABORATORY
P.O. Box 30
State College, PA 16804

THE STRUCTURE OF REYNOLDS STRESS IN THE NEAR WALL REGION OF A TURBULENT PIPE FLOW

by

Paul Chevrin
Howard Petrie
Steven Deutsch

Technical Report No. TR 90-003
March 1990

Supported by:
Office of Naval Research

L.R. Hettche, Director
Applied Research Laboratory

Approved for public release; distribution unlimited

UNCLASSIFIED
SECURITY CLASSIFICATION OF THIS PAGE

REPORT DOCUMENTATION PAGE

1a. REPORT SECURITY CLASSIFICATION Unclassified	1b. RESTRICTIVE MARKINGS
2a. SECURITY CLASSIFICATION AUTHORITY	3. DISTRIBUTION / AVAILABILITY OF REPORT
2b. DECLASSIFICATION / DOWNGRADING SCHEDULE	
4. PERFORMING ORGANIZATION REPORT NUMBER(S) TR-90-003	5. MONITORING ORGANIZATION REPORT NUMBER(S)
6a. NAME OF PERFORMING ORGANIZATION Applied Research Laboratory The Pennsylvania State Univ.	6b. OFFICE SYMBOL (*If applicable*) ARL
7a. NAME OF MONITORING ORGANIZATION	
6c. ADDRESS (*City, State, and ZIP Code*) P.O. Box 30 State College, PA 16804	7b. ADDRESS (*City, State, and ZIP Code*)
8a. NAME OF FUNDING / SPONSORING ORGANIZATION Office of Naval Research	8b. OFFICE SYMBOL (*If applicable*) ONR
9. PROCUREMENT INSTRUMENT IDENTIFICATION NUMBER	
8c. ADDRESS (*City, State, and ZIP Code*) 800 North Quincy Street Arlington, VA 22217	10. SOURCE OF FUNDING NUMBERS PROGRAM ELEMENT NO. / PROJECT NO / TASK NO. / WORK UNIT ACCESSION NO.

11. TITLE (*Include Security Classification*)
THE STRUCTURE OF REYNOLDS STRESS IN THE NEAR WALL REGION OF A TURBULENT PIPE FLOW

12. PERSONAL AUTHOR(S)
P. A. Chevrin, H. L. Petrie, S. Deutsch

13a. TYPE OF REPORT	13b. TIME COVERED	14. DATE OF REPORT (*Year, Month, Day*)	15. PAGE COUNT
technical	FROM _____ TO _____		151

16. SUPPLEMENTARY NOTATION

17. COSATI CODES			18. SUBJECT TERMS (*Continue on reverse if necessary and identify by block number*)
FIELD	GROUP	SUB-GROUP	Reynolds stress, turbulent pipe flow, glycerine, near wall

19. ABSTRACT (*Continue on reverse if necessary and identify by block number*)

The structure of the Reynolds stress in the near-wall region of a fully developed turbulent pipe flow was investigated. The working fluid was glycerine, the high viscosity of which makes the viscous sublayer much larger than in water or air. The Reynolds number of the experiment, based on the diameter of the pipe, was close to 9000. The 0.285 m diameter test-section is located 25 diameters downstream of the contraction to ensure a fully developed flow. A trip ring is used to fix the location of transition at the entrance of the pipe. The test-section was built of acrylic to allow optical access for a laser Doppler velocimeter (LDV). Single-point LDV measurements as close as one wall unit from the wall were made. Agreement with previous investigations was excellent.

20. DISTRIBUTION / AVAILABILITY OF ABSTRACT	21. ABSTRACT SECURITY CLASSIFICATION
☒ UNCLASSIFIED/UNLIMITED ☐ SAME AS RPT ☐ DTIC USERS	Unclassified
22a. NAME OF RESPONSIBLE INDIVIDUAL	22b. TELEPHONE (*Include Area Code*) 814/865-6344 / 22c. OFFICE SYMBOL ARL

DD FORM 1473, 84 MAR — 83 APR edition may be used until exhausted. All other editions are obsolete.

SECURITY CLASSIFICATION OF THIS PAGE
UNCLASSIFIED

A two-component LDV and a one-component fiber-optics LDV were combined to measure the two-point velocity correlation in the wall region. Separation distances as large as 900 wall units in the streamwise direction and 64 wall units in the normal direction were investigated. The effect of velocity bias on the correlation coefficient was studied and it was found to be small in the conditions of this experiment. Two-dimensional maps of the correlation coefficient between streamwise velocity and radial velocity were measured for 6 different distances of the two-components LDV from the wall. The results indicate that the turbulent structures resemble horsehoe vortices whose inclination angle to the wall increases as their distance from the wall increases. A simple model of the flow based on this interpretation was constructed. Agreement with experimental results was very good.

ABSTRACT

The structure of the Reynolds stress in the near-wall region of a fully developed turbulent pipe flow was investigated. The working fluid was glycerine, the high viscosity of which makes the viscous sublayer much larger than in water or air. The Reynolds number of the experiment, based on the diameter of the pipe, was close to 9000. The 0.285 m diameter test-section is located 25 diameters downstream of the contraction to ensure a fully developed flow. A trip ring is used to fix the location of transition at the entrance of the pipe. The test-section was built of acrylic to allow optical access for a laser Doppler velocimeter (LDV). Single-point LDV measurements as close as one wall unit from the wall were made. Agreement with previous investigations was excellent.

A two-component LDV and a one-component fiber-optics LDV were combined to measure the two-point velocity correlation in the wall region. Separation distances as large as 900 wall units in the streamwise direction and 64 wall units in the normal direction were investigated. The effect of velocity bias on the correlation coefficient was studied and it was found to be small in the conditions of this experiment. Two-dimensional maps of the correlation coefficient between streamwise velocity and radial velocity were measured for 6 different distances of the two-component LDV from the wall. The results indicate that the turbulent structures resemble horseshoe vortices whose inclination angle to the wall increases as their distance from the wall increases. A simple model of the flow based on this interpretation was constructed. Agreement with experimental results was very good.

TABLE OF CONTENTS

TABLE OF CONTENTS (continued)

LIST OF TABLES

LIST OF FIGURES

LIST OF FIGURES (continued)

ACKNOWLEDGEMENTS

It is a true pleasure to acknowledge the many people who have contributed to this work.

I would like to thank the entire staff of the Garfield Thomas Water Tunnel for their constant support.

My thanks go to Dr. S. Abdallah, Dr. H. L. Petrie and Dr. R. Wells, whose expertise was an invaluable asset.

The acquisition of the two-point correlations was especially long and repetitive. The help of Brian Kelly in this task made it enjoyable.

My greatest thanks, though, go to Dr. S. Deutsch, who guided me during the completion of this work. He has taught me more than just fluid mechanics; he has given me the desire to explore it further.

This investigation was made under a subcontract with Cornell University, with Dr. J. L. Lumley as principal investigator. Financial support was provided by the Office of Naval Research through SRO IV, under the supervision of Dr. M. M. Reischmann.

à mon père

Chapter 1

INTRODUCTION

1.1 Historical Background

Ever since Prandtl developed boundary layer theory, the behavior of fluid flows close to solid boundaries has been a primary area of research in fluid mechanics. In particular, turbulent boundary layers have been intensively studied because of their practical importance. However, apart from a few qualitative results obtained through dimensional reasoning, little progress has been made.

The evolution of our understanding has been marked by three periods. In the first half of the century, turbulence was viewed essentially as a stochastic phenomenon, characterized by a mean velocity and a random fluctuating velocity. The fluctuating part of the flow, consisting of a continuous range of scales, was regarded as a turbulent fluid medium. It was seen to interact with the mean field through the concept of eddy diffusivity (Taylor, 1915). This representation of turbulence led in the 1940's to the development of the statistical theory of isotropic homogeneous turbulence as a simplified but representative case. This approach produced many important concepts. Among these, the main result is that the behavior of small eddies is independent of the large scale turbulent motion (Kolmogorov, 1941). Research on statistical turbulence theory has been pursued until now (Lesieur, 1986), but its scope is limited: it is now recognized that in practical applications, the homogeneous part of the flow does not govern its large-scale dynamics, i.e., the dynamics of the large eddies.

The second period began in the 1950's, when researchers noticed the intrinsically non-homogeneous character of turbulence, e.g., the discovery of internal intermittency by Klebanoff (1954). At that time it became clear that the notion of a turbulent fluid medium was not adequate. Researchers began to realize that there is no such thing as turbulence, but merely turbulent flows, i.e., the energetic eddies are strongly dependent on the nature of the flow itself (Townsend, 1956). However, the description and measurement of turbulent flows still relied heavily on long-time averaging, an operation which does not recognize the individuality of turbulent eddies. At about the same time, the importance of the wall region for the generation of turbulence in wall-bounded flows was uncovered. The wall region is defined as that part of the flow where non-dimensionalization by inner variables—kinematic viscosity and wall shear stress—leads to a universal velocity profile. Laufer (1954), in an investigation of a fully developed turbulent pipe flow, found that the production of turbulent energy reaches a maximum around $y^+ = 12$. The continuous supply of turbulent energy necessary to counteract viscous dissipation originates mainly in this region. Throughout the 1950's, subsequent investigations confirmed the universality of this finding.

Realizing the importance of the wall region, a group of researchers led by Kline at Stanford University investigated it, using flow visualization. Their discovery of quasi-deterministic structures in this region marks the beginning of the third period, which covers the last thirty years.

1.2 Quasi-deterministic Nature of Turbulent Boundary Layer Flows

Kline and his group systematically investigated the wall region of a turbulent boundary layer using flow visualization. Their experimental facility consisted of

a low Reynolds number open channel flow. Kline and Runstadler (1959), using dye injection through thin slots, were able to show that the wall region possesses a distinct structure and a definite, non-regular, time-dependent motion. They later employed the hydrogen-bubble technique and obtained extensive visual and quantitative results. This effort culminated in the paper by Kline et al. (1967). In the region $0 < y^+ < 10$, they observed that the bubbles were collected along long streaks oriented in the streamwise direction. These streaks were shown to be regions of low streamwise velocity which formed an irregularly distributed pattern in the spanwise direction. Kline et al. attributed their presence to the existence of pairs of counter-rotating streamwise vortices. The interaction of the streaks with the wall region occurred through a sequence of gradual outflow, lift-up, oscillations and final breakup with a sudden ejection of low speed fluid from the wall. Kline et al. referred to the entire process as "bursting."

The position of the low speed streaks on the wall appeared random in time and in space, but the visualizations indicated an average spanwise spacing of approximately $y^+ = 100$. The ejection process occurred mostly in the region $10 < y^+ < 30$. Kline et al. (1967) suggested that bursting could be the result of an instability mechanism in the buffer layer. They discovered that the greatest part of momentum transport between the inner and outer layer occurred during bursting. This means that bursting plays an essential part in the turbulence production process.

The Stanford study was complemented by the work of Corino and Brodkey (1969). These investigators used flow visualization to study the near wall region of a fully developed turbulent pipe flow. They covered a large range of Reynolds numbers, from 5300 to 52000. Their technique involved suspending solid particles in a liquid and photographing the particle motion with a high speed motion

picture camera moving at the mean flow velocity. In essence, they confirmed the findings of Kline et al. (1967), although they perceived the viscous sublayer as essentially passive. Fluid elements were observed to be intermittently ejected outward from the wall region. This ejection created a zone of high shear at the interface between the low speed fluid element and high speed fluid entering from the upstream outer region. When the ejected element entered the high shear zone, it interacted with the outer flow to produce intense, apparently chaotic velocity fluctuations. Corino and Brodkey (1968) identified this process with the bursting event of Kline et al. (1967), but they did not find evidence that ejections resulted from an instability mechanism. They also observed an event called the sweep, in which a fluid element with a velocity close to the local mean entered the field of view from upstream. The study showed that the number and intensity of ejections increased with increasing Reynolds number, and that the ejection frequency scaled with inner variables. In addition, it confirmed the results of Kline et al. (1967) that most of the turbulent production occurs during bursting: they estimated that the ejections account for approximately 70% of the Reynolds stress measured by Laufer (1954).

These two studies marked the beginning of a systematic search for quasi-deterministic structures in turbulent shear flows, and also initiated a new interest in flow visualization techniques. Flow visualization is well adapted to situations where spatial and temporal fluid motions occur simultaneously with random phase. In these situations, data from a fixed sensor, such as a hot wire or a pressure transducer, are difficult to interpret. However, flow visualization has limitations:

- It is a qualitative technique. It has been difficult to extract reliable and accurate quantitative information from visual data.

- It easily leads to misinterpretation in three-dimensional and unsteady flows, in particular when the visual data are stored in two dimensions (pictures or video).

- Visually observed events might not be representative patterns of the flow. On the contrary, an event characteristic of the flow might be totally missed by the flow visualization technique.

By the beginning of the 1970's these limitations and the need for quantitative results became apparent. Most subsequent investigations resorted to conventional measuring techniques, sometimes associated with flow visualization.

The major difficulty with quantitative measurement of the flow field in the near-wall region is its very small size. In most cases, this difficulty has been alleviated—at least partially—by enlarging the wall region. This can be achieved by increasing the wall length scale ν/u_τ, i.e., either by decreasing the friction velocity or by increasing the kinematic viscosity. Most investigators, for practical reasons, have adopted the first solution: since the friction velocity is a decreasing function of streamwise distance in a turbulent boundary layer, a simple way of achieving a small friction velocity is to use a very long facility.

Rao et al. (1971) studied a turbulent boundary layer in air over a wide range of Reynolds numbers, using hot wire anemometry. They were particularly interested in the bursting frequency. Their burst detection method was designed to detect the periods of large amplitude of the high-pass filtered derivative of the streamwise velocity. They found that the mean burst frequency scales with outer rather than inner variables and concluded that the dynamics of the wall region of a turbulent boundary layer can be understood only on the basis of a coupling between the inner and the outer layer.

Kim, Kline and Reynolds (1971), after further refining the hydrogen bubble flow visualization technique, combined it with hot wire anemometry. They tagged the hot-wire signal when a turbulent burst was observed to pass over the hot wire. They noticed that several ejections, as defined by Corino and Brodkey (1969), can occur in one burst. Their results confirmed the findings of Rao et al. (1971) that the bursting frequency scales with outer variables. They also showed that essentially all the turbulence production occurs during bursting.

Willmarth and Lu (1972) concentrated their effort on developing a scheme able to detect the passage of a burst from the hot wire signal itself. They studied a turbulent boundary layer at the two Reynolds numbers of 4230 and 38000. They noticed that the bursting process, beginning with the lift-up of a low speed fluid element, has a characteristic signature. An event was thus said to occur when the streamwise fluctuating velocity u, measured by a hot wire located at a distance $y^+ = 16.8$ above the wall, was decreasing and smaller than $T\overline{u^2}$, where T is a constant. This allowed them to define an indicator function:

$$\phi(T,t) = \begin{cases} 1 & \text{when an event is detected} \\ 0 & \text{otherwise} \end{cases}$$

and the conditional average of a quantity z:

$$\overline{z}_c = \frac{\int_0^{+\infty} z\,\phi(T,t)\,dt}{\int_0^{+\infty} \phi(T,t)\,dt}$$

where t represents time. Using this method, Willmarth and Lu found that the events detected with the above criterion make a large contribution to the production of turbulent energy. In a subsequent article, Lu and Willmarth (1973) modified their detection scheme, so that an event was said to occur when

the product of the streamwise component u by the normal component v of the fluctuating velocity was greater than a certain threshold H:

$$|uv| > H$$

They showed that this criterion is a better indication of the Reynolds stress activity. They found that the events corresponding to u negative and v positive—second quadrant in u-v coordinates—account for 77% of the long-time average Reynolds stress $\overline{uv}$, while those associated with u positive and v negative—fourth quadrant in u-v coordinates—account for 55% of $\overline{uv}$ (the first and third quadrants have a negative contribution to the Reynolds stress). Therefore they identified the second quadrant event with a burst and the fourth quadrant event with a sweep. Additionally they found that the bursting frequency scales with outer variables. From an analysis of their results, they proposed that the features of a turbulent boundary layer flow could be explained by the convection past the measuring station of a characteristic pattern such as hairpin vortices.

Blackwelder and Kaplan (1976) examined the wall structure of a turbulent boundary layer using conditional sampling of signals from hot wire rakes. Their detection technique is based on the observation that a burst corresponds to a period of intense turbulent activity. The Variable Interval Time Averaged (VITA) variance defined as:

$$Var(T,t) = \frac{1}{T}\left(\int_{T-t/2}^{T+t/2} u^2\,dt - \left(\int_{T-t/2}^{T+t/2} u\,dt\right)^2\right)$$

should therefore present a peak at the passage of a burst. They defined an indicator function of the form:

$$\phi(T,t) = \begin{cases} 1 & \text{if } Var > k\overline{u^2} \\ 0 & \text{otherwise} \end{cases}$$

Using conditional averaging in a manner similar to that of Willmarth and Lu (1972), they observed a high degree of coherence of the turbulence structures in a direction normal to the wall. They found that in regions of strong streamwise velocity deficit, the normal velocity is directed outwards whereas in regions of strong streamwise velocity excess, the normal velocity is directed inwards. Thus these two patterns were respectively associated with ejections and sweeps. Blackwelder and Kaplan confirmed the previous finding that the conditionally averaged Reynolds stress is an order of magnitude greater than its conventionally averaged value.

The work of Head and Bandyopadhyay (1981) marked an important step in our understanding of the dynamics of turbulent boundary layers. Their investigation of the structure of the outer region of a turbulent boundary layer provided new clues on the relationship between inner and outer layers. Using flow visualization, they studied in great detail the outer region of a turbulent boundary layer, for Reynolds numbers ranging between 500 and 17500. They injected smoke at the origin of the boundary layer so that the entire layer was visually marked. They found that the boundary layer is made up very largely of elongated hairpin vortices or vortex pairs originating in the wall region. These hairpin vortices are inclined at an average angle of 45° to the wall, have spanwise dimensions scaling with inner variables and a length scaling with outer variables. In view of these results, they suggested that the counter-rotating vortices observed in the wall region at low Reynolds number could be the legs of the vortex pairs they observed in the outer region.

Johansson and Alfredsson (1982) studied a fully developed turbulent channel flow for Reynolds numbers varying between 13800 and 48900. They investigated

in detail the character of the VITA detection technique introduced by Blackwelder and Kaplan (1976). They showed that this technique does not allow one to define a unique burst frequency, because it depends strongly on the threshold level. However, by using the same threshold level at different values of the Reynolds number, they deduced that the burst frequency in the outer region scales with outer variables. In a subsequent article, Alfredsson and Johansson (1984) found that the correct time scale for bursting in the near wall region is the arithmetic mean of the inner and outer scales, i.e., it is of mixed type, even very close to the wall. They interpreted this result from the mixed character of bursting, which results from the interaction of the outer layer and the inner layer.

Blackwelder and Haritonidis (1983) measured the burst frequency in a turbulent boundary layer for Reynolds numbers ranging from 1000 to 10000. They found a strong effect of the sensor size on the measured frequency and attributed previous discrepancies in the scaling law to the use of sensors which were too large. When their sensor had a length smaller than $l^+ = 20$, their data showed that the bursting frequency always scaled with inner variables. Willmarth and Sharma (1984) and Luchik and Tiederman (1987) later confirmed these results. Thus the more recent investigations, with smaller and better probes, seem to confirm the inner scaling hypothesis.

A different approach, used in recent years, is to study a laminar flow in which some of the features of a turbulent boundary layer are reproduced. In these experiments, no background noise due to the outer flow is introduced, so that flow visualization and burst detection are easier to carry out. Thus some researchers have tried to generate laminar boundary layers which mimic artificially the large scale structure of turbulent boundary layers. Accarlar and Smith (1987)

generated hairpin vortices in a laminar boundary layer by placing a hemispheric protuberance on the wall. They used dye injection and a hydrogen-bubble wire to visualize the flow pattern downstream of the hemisphere. Many of the visual patterns observed in this experiment closely match those observed in turbulent boundary layers. Hot-wire measurements also indicate a close resemblance between the streamwise velocity profiles and those in a turbulent boundary layer. These observations support Head and Bandyopadhyay's hypothesis (1981) that the outer region of a turbulent boundary layer is filled with random arrays of hairpin vortices.

Swearingen and Blackwelder (1987) studied the growth, breakdown and transition to turbulence of counter-rotating vortices generated via the Görtler instability along a concave wall. They determined that the low-speed regions between the vortex pairs create strongly inflexional profiles of the streamwise velocity. The oscillations which develop on these profiles were found to correlate better with the spanwise, not normal, velocity gradient. These results can be interpreted in relation to theoretical studies by Orszag and Patera (1984), Jang et al. (1984) and Landahl (1986), who have showed that the primary instability mode of the normal velocity profile is damped. However, when this primary instability mode is excited by a finite disturbance, it can give rise to a secondary instability developing in the spanwise direction. Nonlinear analyses of this second mode of instability yield equilibrium solutions which look very much like the counter-rotating vortex pairs observed in turbulent boundary layers, and in Swearingen and Blackwelder's experiment.

Numerical simulation represents an appealing alternative by which to study turbulence. Due to computer limitations, however, only low Reynolds number simulations are possible. Moin and Kim (1982) performed large eddy simulations

to compute the flow field in a turbulent channel flow at a Reynolds number of 13800. The database generated by their calculations was used to perform a number of analyses of the flow. Simulating the hydrogen-bubble flow visualization of Kline et al. (1967), they were able to reproduce almost exactly the same visual patterns. Kim (1983), using a spatial version of the VITA technique developed by Blackwelder and Kaplan (1976), determined that the ejection process is associated with a localized adverse pressure gradient, with simultaneous lift-up of the streamwise vortices. Moin (1984) confirmed the results of Head and Bandyopadhyay (1981), and showed that the vorticity vector in the outer region is preferentially inclined at an angle of 45° to the wall. He also found that these vortices contribute significantly to the long-time average Reynolds stress. Because the spatial resolution of the calculation may not have been fine enough to resolve all the scales in the wall region, these results should be interpreted with care. In spite of its cost, the numerical simulation strategy is an effective approach, and much of its potential remains to be explored.

1.3 Toward a Rigorous Definition of Turbulent Structures

The main difficulty associated with the study of large structures in turbulent shear flows lies in the ambiguity associated with their definition. An additional difficulty comes from the unsteady and three-dimensional character of turbulent flows, which makes interpretation of qualitative and quantitative data hazardous. Indeed, according to the conditional averaging method used, different flow patterns emerge.

To avoid these problems, Lumley (1967) proposed the proper orthogonal decomposition method, which naturally defines the most energetic structures in

a non-homogeneous turbulent flow. The method looks at the turbulent flow field as a statistical realization of a random vector field. The dominant structure of the flow is defined as one which maximizes in a mean-square sense its correlation with the random field (this is also referred to as the Karhunen-Loeve expansion in statistics). The problem can be reformulated as an eigenvalue problem and solved for the dominant structure. The method was first applied to find the dominant eddies in a turbulent wake (Payne, 1966) using the experimental data of Grant (1959). Application of the method to the wall region of a turbulent boundary layer was accomplished by Bakewell (1966), Moin (1984) and Herzog (1986).

Bakewell (1966) performed his measurements in a fully developed pipe flow using glycerine as the working fluid. The kinematic viscosity of glycerine is about 200 times that of water, thus making the wall region large enough for using hot-film probes down to a y^+ smaller than 1. The Reynolds number of the flow was 8700. He carried out extensive measurements of two-point correlations of the streamwise velocity using a pair of hot-film anemometers. The missing components of the correlation tensor were computed using a mixing-length hypothesis. He used these data to extract the large eddies following the proper orthogonal decomposition technique. Bakewell found that the dominant structure consists of a pair of counter-rotating vortices with a strong outflow of low-speed fluid between the two vortices. This structure had a long streamwise extent (up to $\Delta x^+ = 1000$) and a spanwise extent of typically $\Delta z^+ = 100$. Such a picture of the flow matches closely the description of the near-wall region by Kline et al. (1967).

Moin (1984) applied a two-dimensional version of Lumley's technique to a large-eddy simulation database. He found a dominant characteristic eddy very

similar to Bakewell's experimental result. This eddy contains a significant portion of the total turbulent kinetic energy and makes an important contribution to turbulence production.

Herzog (1986) extended Bakewell's work by measuring the streamwise and circumferential components of velocity using two pairs of split-film anemometers. Using the symmetry properties of the correlation tensor and the incompressibility condition, he was able to compute all the components of the correlation tensor. The typical eddy found by Herzog is a pair of counter-rotating rolls with their centerlines about 60 wall units apart, rising almost linearly at an angle of approximately 5° with the wall. However, some problems related to the use of hot films in glycerine were encountered in this investigation. Corrosion on the split film surface caused a temporal drift of their response. Another difficulty concerned the presence of air bubbles which stuck on the sensors.

Lumley's method has the advantage over other techniques that it does not require any subjective interpretation. However, it has two important drawbacks:

- It requires a vast amount of data.

- The dynamics of the flow is lost in the averaging process because, in practice, the spatial correlations are computed through time average. Therefore the picture obtained by this method should not be interpreted as a typical instantaneous view of the flow. The method merely supplies a set of functions on which the second-order statistics, and in particular the mean turbulent kinetic energy of the flow, are best captured (Brown, 1960).

The question of whether the method is well adapted to capture the dynamics of the flow is still open. Sirovich (1987) claims that the Karhunen-Loeve

expansion provides a practical, "in a sense optimal," description of the attractor of the motion in the phase space. There is some evidence to support this claim. Sirovich and Rodriguez (1987) examined the Cinzburg-Landau equation in the chaotic regime. They compared the results of a numerical solution based on a spectral method, with the results of a Galerkin approximation using only the first three modes of the Karhunen-Loeve expansion. Indeed, the power spectrum and the Poincaré section obtained from the Galerkin approximation fall neatly on top of those from the numerical solution. In another numerical experiment, Aubry et al. (1988) considered a finite-dimensional description of the wall region of a turbulent flow using the set of eigenfunctions obtained experimentally by Herzog (1986). The dynamics of their model appears to be in many respects similar to the visual observations of previous researchers. In particular, a "bursting event" is observed beyond a critical value of the Reynolds number.

Goldshtik (1982) proposes a different approach to identify structures in turbulent flows. First he points out that Lumley's method becomes less interesting in the case of homogeneous fields: in this case the spectrum is continuous and the Karhunen-Loeve expansion leads to the classical Fourier expansion; however, large turbulent structures can be observed even in the case of homogeneous fields (e.g., Harris et al., 1977). Further, the Karhunen-Loeve expansion does not supply any information concerning the dynamics of the flow; on the contrary, it dilutes this information during the averaging procedure. Goldshtik's theory is based on the assumption of small overlap of the turbulent structures. The specific character of the function that serves as a structure can be determined by finding the solution of a classical boundary value problem. This approach seems very promising, experimentally and theoretically. It has been applied to the study of the Lorenz equations with some success (Goldshtik,

1982). Further work seems necessary before it can be applied to the study of fully developed turbulence.

1.5 Objectives of This Study

Thus, in spite of the enormous effort devoted to the understanding of the flow in the wall region, the structure of turbulence is still poorly understood. The relationship between the differents events that have been observed—streaks, bursts, sweeps...—is not clear. Most of all, it seems that these observations, rather than help theoreticians, have made their task all the more complicated. It may be that the complexity of the flow has diverted the attention of experimentalists from some of the questions of essential importance, like momentum transport. This quantity has been clearly linked to the bursting event (Kline et al., 1967), but the spatial structure of the turbulent eddies carrying the momentum has not been investigated. The goal of this work was to investigate the structure of these eddies in the wall region of a turbulent boundary layer, with a particular emphasis on their relationship to the Reynolds stress.

Velocity measurements were carried out in the glycerine tunnel of the Applied Research Laboratory at The Pennsylvania State University. Two-point velocity correlations were measured using a two-component laser Doppler velocimeter (LDV) coupled with a one-component fiber-optics LDV. The spatial correlation between the streamwise and the radial velocity was measured in the radial plane of the pipe, between the wall and $y^+ = 64$. Complete maps of the correlation were established and the form of the dominant eddies in this region of the flow was deduced from the measurements.

Using information from the measurements, a model of the flow in the near-wall region was constructed. Predictions of turbulence quantities were made and compared with experimental results. Agreement is very good.

Details of the experimental apparatus and preliminary measurements are described in chapter 2. The experimental results are presented and discussed in chapter 3. The model of the wall region is developed in chapter 4. Chapter 5 includes the conclusions of the study and recommendations for future work.

Chapter 2

PROCEDURE OF THE INVESTIGATION

2.1 Introduction

In this chapter, we will present the experimental facility and the measuring techniques used in the course of the investigation. The experimental facility is the same as described by Bakewell (1966) and Herzog (1986) in their doctoral theses. Whereas these two investigations were performed with hot-wires (Bakewell, 1967) or split-films (Herzog, 1986), the present work used laser Doppler velocimetry for velocity measurements. In addition to being non-intrusive—a definite advantage when one is dealing with glycerine—the LDV does not suffer from such problems as probe interference, corrosion, and a difficult calibration process. Some problems exist, of course, and they will be explained in the course of this chapter. The measurements not directly relevant to the structure of turbulence will also be presented. It should be mentioned that the results labeled "model" in the figures will be explained in chapter 4.

2.2 Experimental Facility

The experimental facility is a closed circuit tunnel which uses glycerine as the working fluid. A summary of the physical properties of glycerine is given in table 1. Due to the large value of the kinematic viscosity of glycerine, the viscous sublayer is thicker than in water or air, thus making measurement in the near-wall region more practical than in conventional facilities.

TABLE 1

Physical Properties of Glycerine at 33.5 °C.

Water content		4.5 %
Kinematic Viscosity	ν	$202.5\,10^{-6}\,\mathrm{m}^2/\mathrm{s}$
Fluid Density	ρ	$1232\,\mathrm{kg}/\mathrm{m}^3$
Specific Heat Capacity	c_P	$2430\,\mathrm{Nm}/(\mathrm{kg}\,^\circ\mathrm{C})$
Coefficient of thermal expansion	β	0.000615
Refractive Index	n	1.4667
Surface Tension	σ	$6.208\,10^{-2}\ \mathrm{N}/\mathrm{m}$
Thermal Conductivity	k	$0.292\,\mathrm{N}/(\mathrm{sec}\,^\circ\mathrm{C})$
Thermal Diffusivity	α	$9.75\,10^{-8}\,\mathrm{m}^2/\mathrm{sec}$
Prandtl Number	Pr	2076

The facility (figure 1) contains 8200 liters of commercially available glycerine. The pump is a 75 kW constant speed (900 rpm) centrifugal pump located in the bottom leg of the facility, downstream of the test section.

The settling chamber is equipped with screens to prevent separation and reduce turbulence at the entrance, and a honeycomb to suppress large-scale vorticity. It is followed by a 16 to 1 contraction to the test-pipe. The test-pipe is 7.6 m long and 0.285 m in diameter, with the actual test-section located 25 diameters downstream of the contraction. The inside surface of the pipe is honed to a 16 μinch rms finish. The location of the boundary layer transition is fixed at the entrance of the test-pipe by a trip-ring with a tooth height equal to 10 mm; this gives a trip Reynolds number approximately equal to 313.

Since the pump speed can not be varied, the only practical way to adjust the Reynolds number is by changing the viscosity. The viscosity of glycerine was measured by the Cannon Instrument Company (Boalsburg, PA), which provided the following equations for the calculation of the viscosity of glycerine ν (in m^2/s) as a function of the temperature T (in°C):

$$ln(lnZ) = 24.98023 - 4.07149969\, ln(T + 273)$$

$$Y = Z - 0.7$$

$$\nu = (Y - exp(-0.7487 - 3.295Y + 0.6119Y^2 - 0.3193Y^3))10^{-4}$$

Figure 2 is a plot of glycerine viscosity vs temperature. As can be seen, glycerine viscosity is a strong function of temperature. This property suggests a temperature control of the Reynolds number, which is actually achieved with the help of a counter-flow heat exchanger. Glycerine is removed from the tunnel through holes in the tunnel wall, located in the vertical leg downstream of the

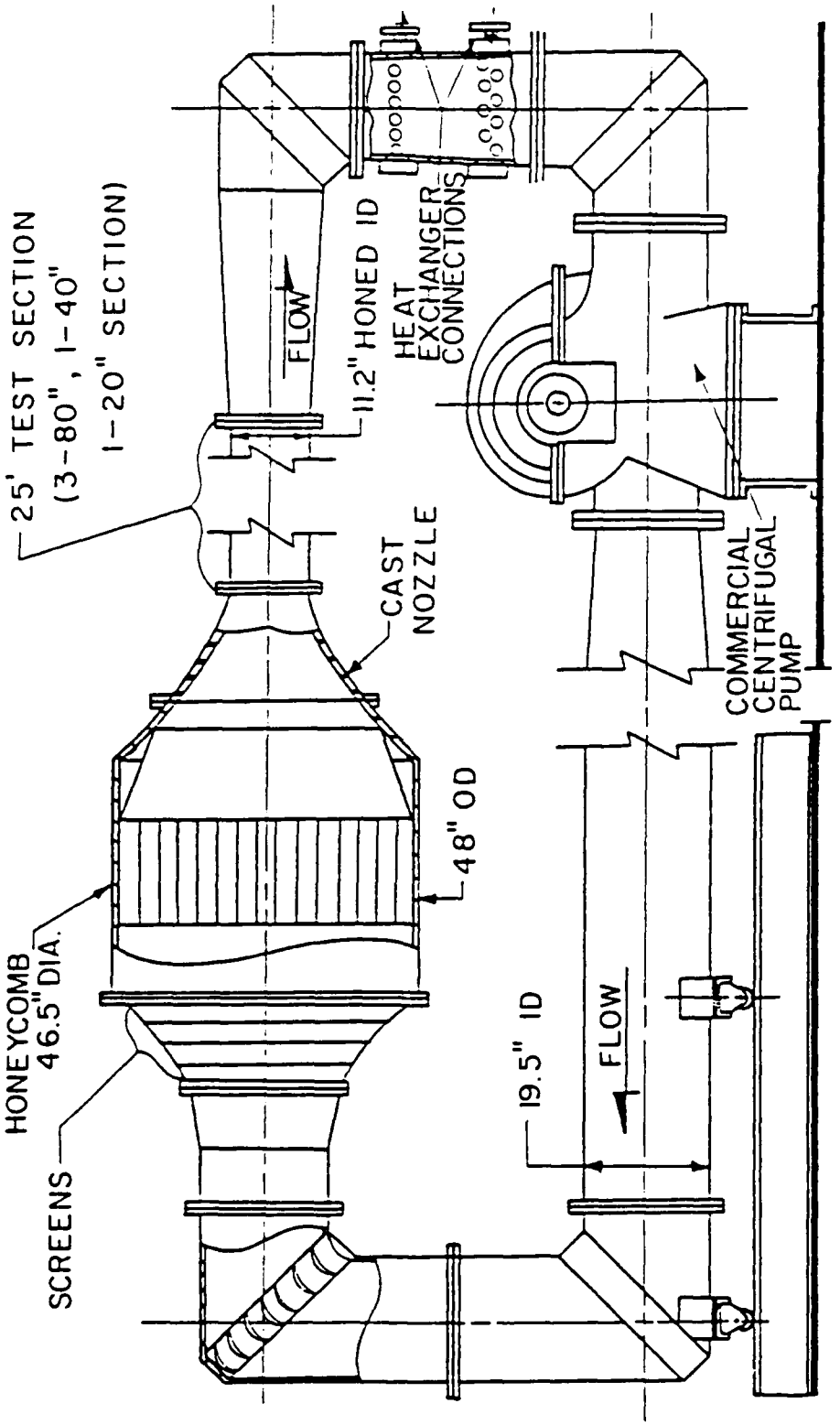

FIGURE 1
Schematic View of Test Facility

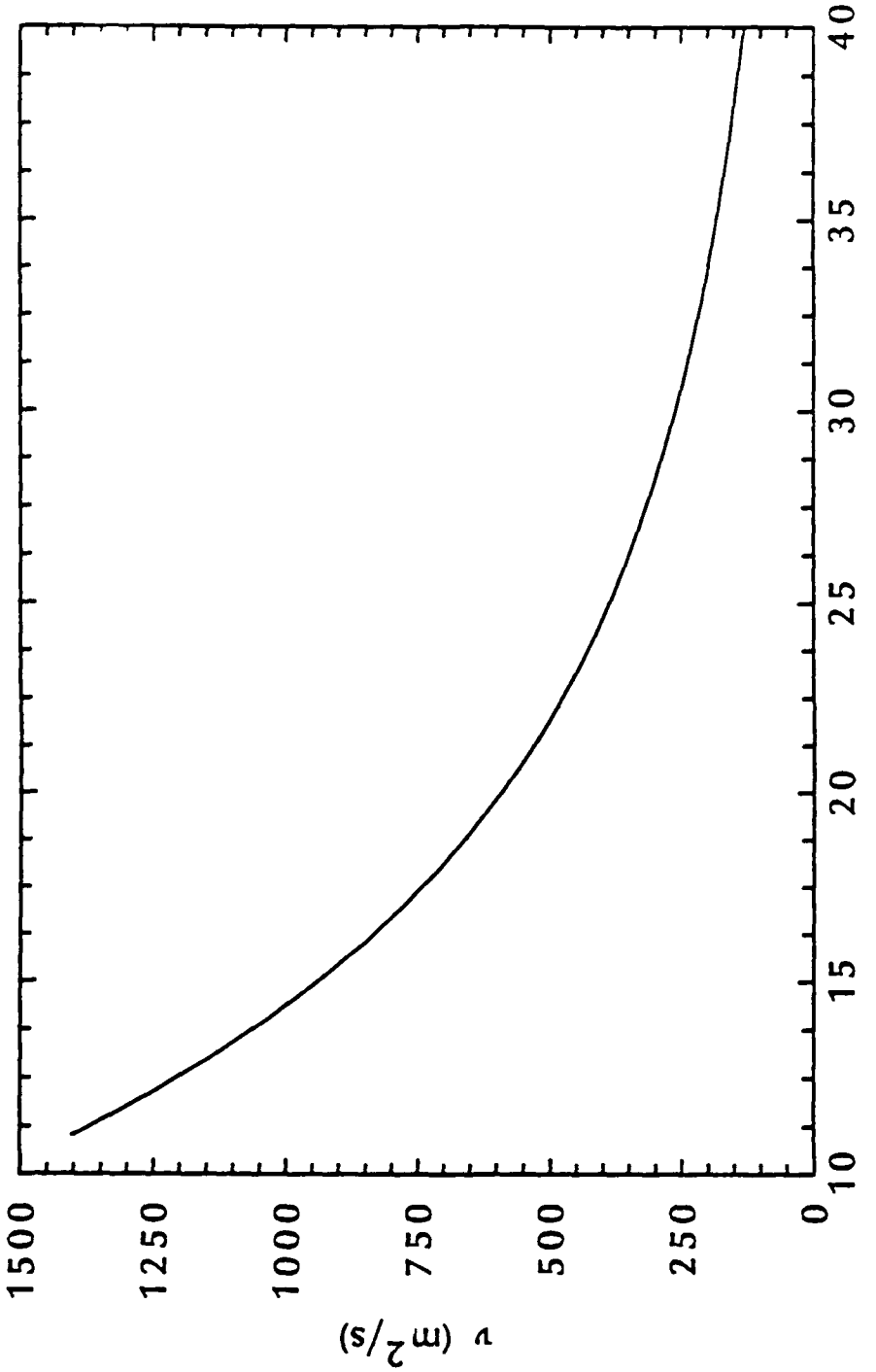

FIGURE 2
Variation of Glycerine Kinematic Viscosity
with Temperature

test section (figure 1). Glycerine temperature is monitored with a thermistor immediately downstream of the test-section. The temperature is adjusted by varying the flow rate of cooling water through the heat exchanger. Reinjection of the cooled glycerine into the tunnel occurs through two rows of tubes immediately downstream of the intake. Further mixing by the pump insures a uniform temperature of the glycerine.

To replicate the viscosity of glycerine in Herzog's experiment, i.e., $\nu = 202.5\,10^{-6}$ m^2/s, the temperature of the tests was chosen equal to 33.5°C. This choice insured that all other test parameters were equal to those of previous investigations. Since the operating temperature of the facility is about 13°C above ambient temperature, a thermal gradient could develop in the radial direction, thus causing significant changes of viscosity across the test-pipe. The Prandtl number of glycerine is larger than 2000 (table 1), which keeps heat exchange between glycerine and the pipe wall very small. Bakewell (1967) measured the temperature gradient at the wall and found that it could be made negligible by insulating the facility with thick foil-faced fiberglass.

The power input from the pump is fixed by the motor. Thus the wall shear-stress at a given location, and for a given flow regime, depends little on temperature; temperature changes affect mainly the flow-rate.

2.3 Wall Shear-stress Measurement

The pressure drop in the test-pipe is measured through an array of 22 Foxboro pressure transducers regularly distributed between the contraction and the test-section. The signal from the transducers was passed through a multiplexer and sent to the VAX 11/782 of the Garfield Thomas Water Tunnel via an IEEE bus.

Calibration of the transducers was accomplished with an Ametek calibration instrument.

Figure 3 represents the pressure drop in the test-pipe at the operating temperature of 33.5°C. The pressure drop becomes linear only a few diameters downstream of the contraction, indicating that the large-scale turbulent flow is fully developed in the test-section. In the near-wall region, where the energy spectrum is narrow, we can expect all scales to have reached an equilibrium (Comte-Bellot, 1963).

Application of the conservation of momentum in the fully developed portion of the flow allows calculation of the wall shear-stress:

$$\tau_w = \frac{R}{2}\frac{dP}{dx}$$

Figure 4 represents the wall-shear stress in the fully developed part of the test-section as a function of temperature. The transition of a laminar to a turbulent regime is observed between 29°C and 31°C. As expected, in a given flow regime, no significant variation of τ_w occurs as temperature is modified. The friction velocity u_τ is defined as:

$$u_\tau = \sqrt{\frac{\tau_w}{\rho}};$$

at 33.5°C, its value is 0.40±0.08 m/s. The viscous length scale defined using this value of u_τ and the viscosity of glycerine is:

$$l_\tau = \frac{\nu}{u_\tau} = 0.51 \text{ mm}$$

and the viscous frequency scale:

$$f_\tau = \frac{u_\tau^2}{\nu} = 790 \text{ Hz}$$

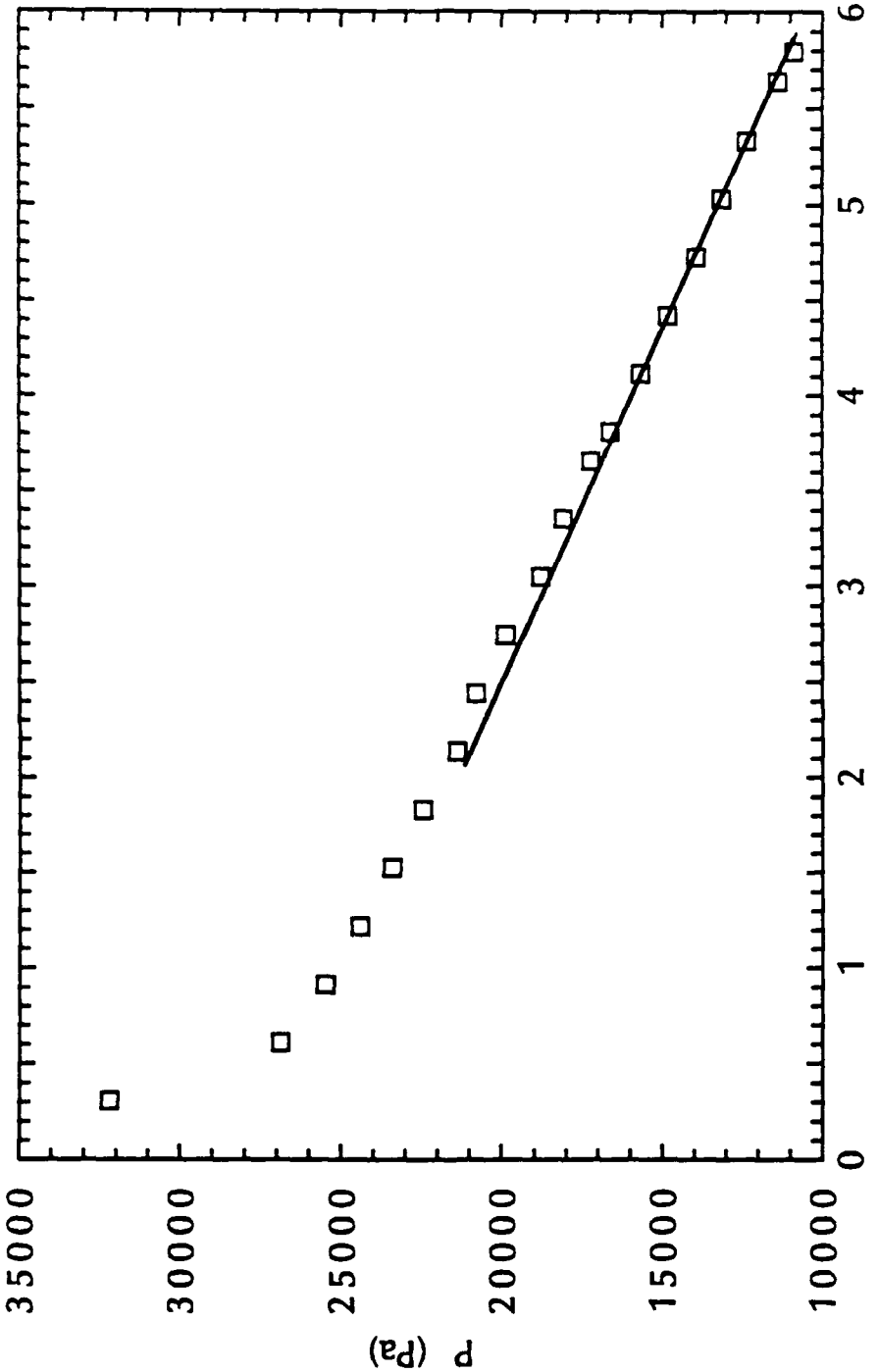

FIGURE 3
Pressure Distribution along Pipe Axis

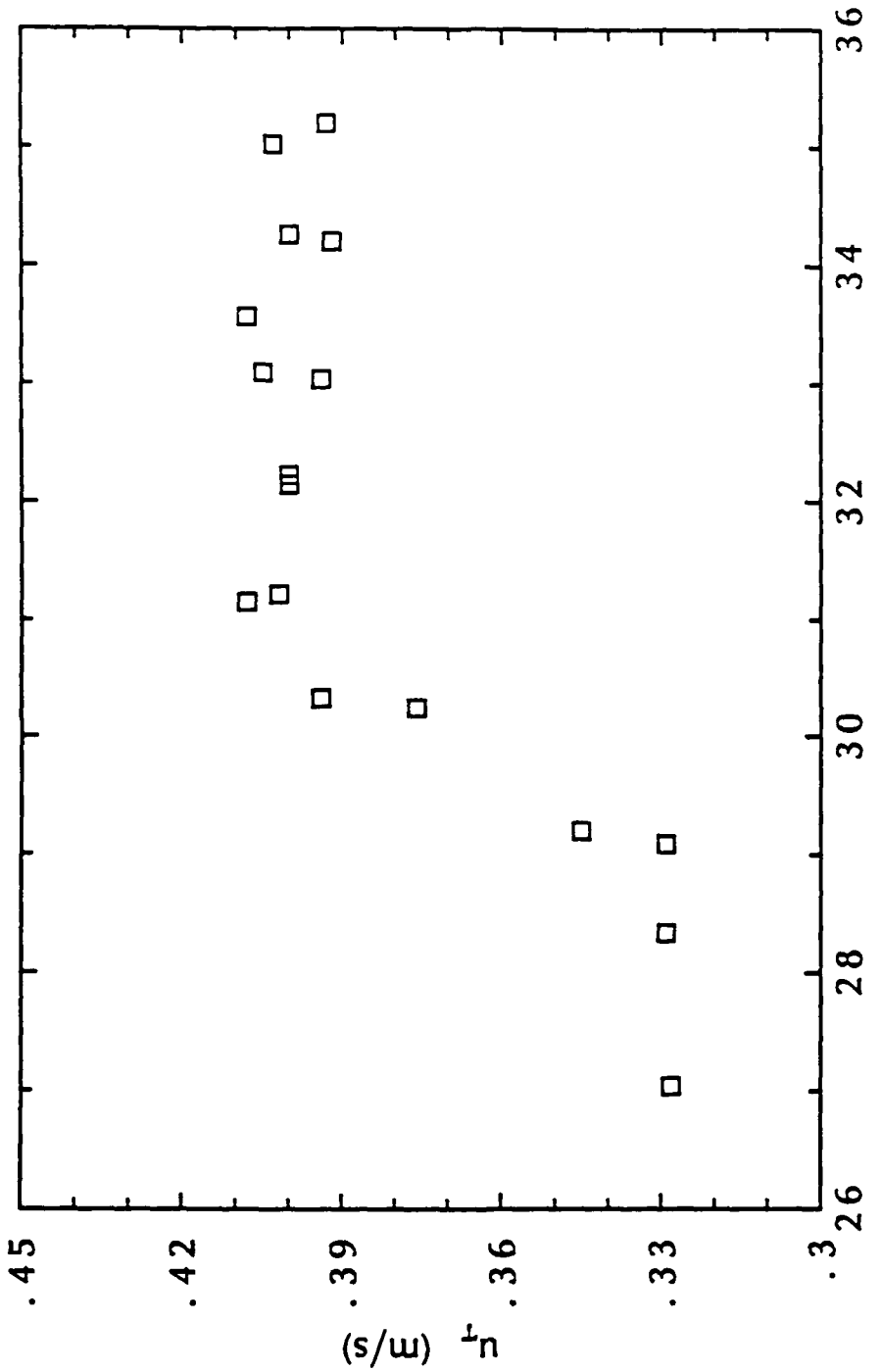

FIGURE 4
Variation of Friction Velocity with Temperature

2.4 Bulk Velocity Measurement

The bulk velocity is obtained by measuring the static pressure drop $P_1 - P_0$ across the nozzle. To accomplish this, an additional pressure transducer was installed in the settling chamber, immediately before the contraction. The flow in the contraction experiences a strong acceleration, thus making the boundary layer very thin. We can therefore neglect viscous effects, and apply Bernoulli's equation between this location and the first pressure tap at the entrance of the test-pipe. With conservation of mass, the bulk velocity is obtained as:

$$U_{av} = \sqrt{\frac{2\,(P_0 - P_1)}{\rho(1 - A_1^2/A_0^2)}}$$

where A_0 and A_1 are the cross-sectional areas in the settling chamber and the test-pipe respectively. Figure 5 represents the bulk velocity as a function of temperature. As opposed to the wall shear-stress results of Figure 4, the bulk velocity varies monotonically with temperature. The bulk velocity at 33.5°C was found to be $U_{av} = 6.78 \pm 0.1$ m/s. An upper bound for the size of the largest eddies is given by the diameter of the pipe. Therefore the frequency scale of the largest eddies of the flow can be estimated using the bulk velocity and the diameter of the pipe:

$$f_L = \frac{U_{av}}{D} = 24 \text{ Hz}$$

An estimate of the Kolmogorov frequency in the center of the pipe is given by Bakewell (1966):

$$f_k = \left(\frac{4\,u_\tau^2\,U_{av}}{D\,\nu}\right)^{1/2} = 272 \text{ Hz}$$

This frequency is about one third of the viscous frequency in the wall region. Since this result is based on an order-of-magnitude analysis, it might not be significant. However it indicates that the viscous time scale at the wall is probably smaller than the Kolmogorov scale in the pipe core. Experimental investigation

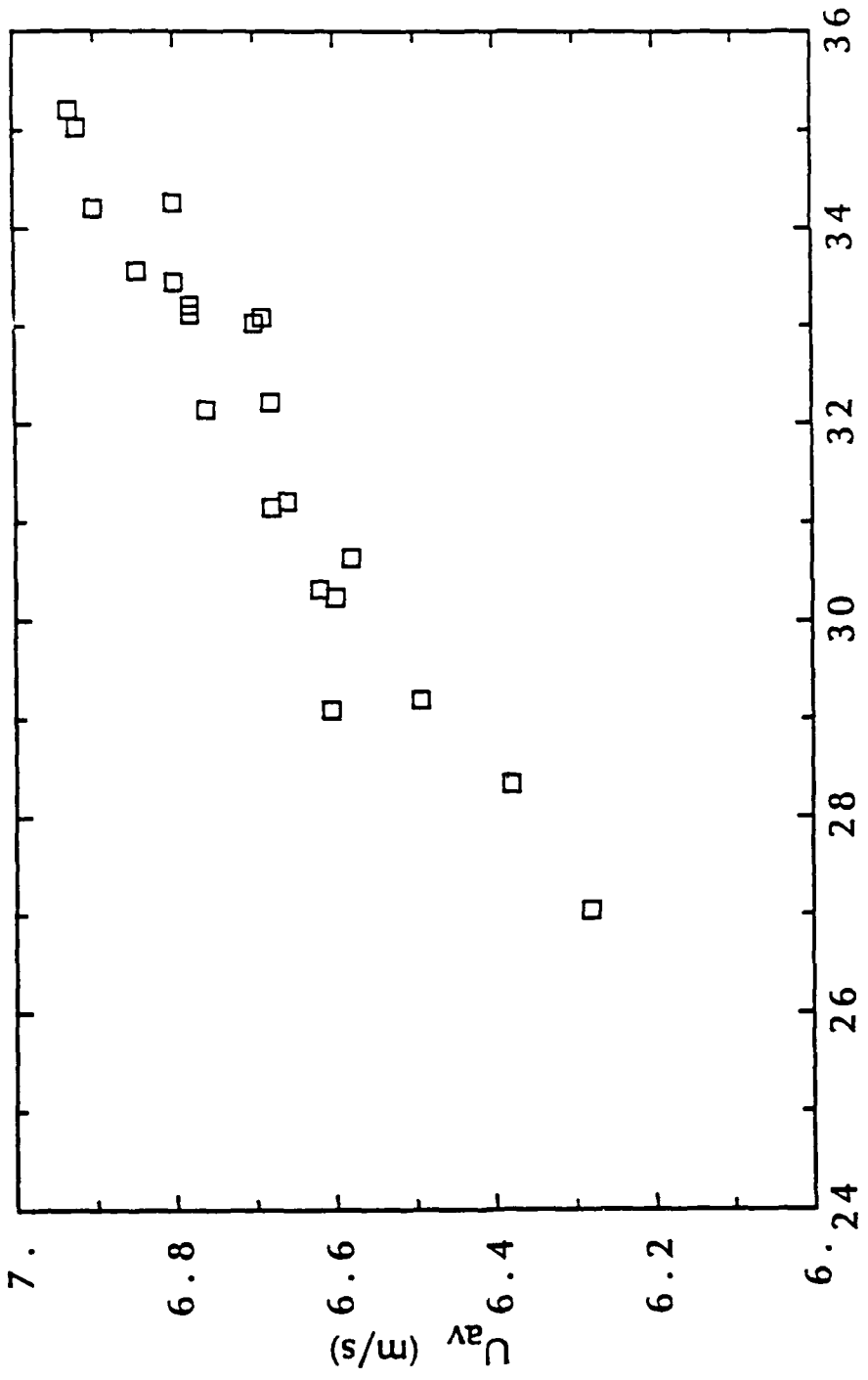

FIGURE 5
Variations of Bulk Velocity with Temperature

of the wall region thus requires not only better physical resolution, but also better frequency resolution.

Knowledge of the bulk velocity provides another check that the flow is fully developed. The Blasius formula linking the Darcy friction factor Λ to the Reynolds number Re_d in a fully developed pipe flow (White, 1974) gives:

$$\Lambda = 0.3164\, Re_d^{-1/4}$$

where:

$$\Lambda = \frac{8\,\tau_w}{\rho\, U_{av}^2}$$

Solving for the friction velocity u_τ gives the following expression:

$$u_\tau = 0.1989\, U_{av}\, Re_d^{-1/8} \tag{2.1}$$

At 33.5°C, this gives $u_\tau = 0.43$ m/s, in good agreement with the reference value calculated from the pressure drop. The small difference might result from the disturbance introduced by the trip ring, which is located near the first pressure transducer. Streamline curvature effects, due to the large size of the trip ring compared to the diameter of the pipe, probably significantly affect the static pressure measurement there.

The operating conditions of the experimental facility are presented in table 2. The friction velocity was computed from the pressure gradient measurements.

2.5 Velocity Measurement Instrumentation

A two-component laser Doppler velocimeter (LDV) and a one-component fiber-optics LDV were used for the velocity measurements. In order to provide optical access into the pipe, a specially designed acrylic test-section was built

TABLE 2

Operating Conditions of Experimental Facility

Operating Temperature	T	$33.5\,°C$
Pipe Diameter	D	$0.285\,\mathrm{m}$
Mean Velocity	U_{av}	$6.34\,\mathrm{m/sec}$
Reynolds Number	R_e	8923
Friction Velocity	u_τ	$0.40 \pm 0.08\,\mathrm{m/sec}$
Viscous Length	l	$0.51\,\mathrm{mm}$

(figure 6) to replace the previous stainless steel test-section. The inside surface of the test-section was machined to an rms surface finish of 20 μinch, i.e., less than 0.001 viscous wall unit. The index of refraction of acrylic ($n = 1.49$) matches closely that of glycerine ($n = 1.479$) so that the deflection of the laser beams at a glycerine-acrylic interface was very small, particularly since the beams were almost normal to the surface. To avoid beam deflection caused by pipe curvature, a flat window was added to one side of the pipe and the space between the window and the pipe was filled with glycerine. The side-walls holding the window on the test-section were also made of plexiglas so that optical access through the top and the bottom parts of the pipe were possible. Calculation of the beam angles inside the pipe was made by applying Snell's law. The index of refraction was approximated by $n = 1.49$. This approximation is of the same order of magnitude as the inaccuracy in the index of refraction of acrylic, which may be caused by inhomogeneities and wavyness of the test-section surface. This represents an 1.2% error in the estimation of the distance of the probe from the wall.

Simultaneous measurement of the three components of velocity was one of the goals of this study, and we initially hoped that the three-component LDV system of the Garfield Thomas Water Tunnel would give us this capability. This LDV system is a two-colour, five-beam backward-scatter system, and is equipped with three counter processors. It uses the blue line and green line of an Argon-ion laser. A detailed description of the system is given in Appendix A.

Measurement of the radial component of velocity, the "on-axis" component, turned out to be impractical. An analysis of the effect of beam misalignment on the on-axis component, given in appendix B, shows that this component is very sensitive to misalignment, making alignment of the beams extremely difficult to obtain.

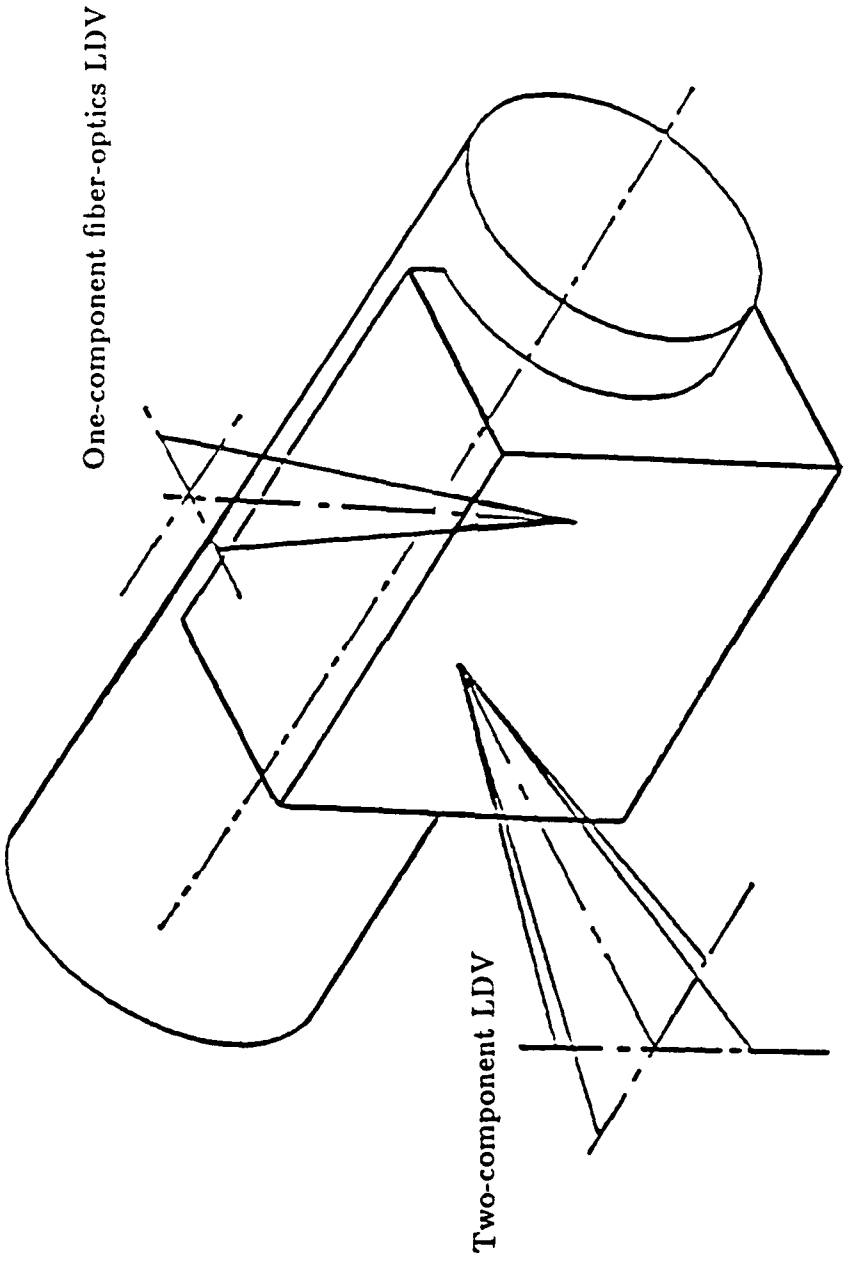

FIGURE 6
Arrangement of LDV System
for Two-Point Measurements

A second and more serious difficulty comes from the large amount of noise present in the on-axis component of velocity. A simplified analysis of this problem is also given in appendix B. The analysis predicts that the noise present in the on-axis component v is proportional to the noise present in other components, u or w. The factor of proportionality k has the form:

$$k = \frac{v}{w} \frac{1}{2sin(\phi/2)}$$

In our case, v and w are of the same order of magnitude and ϕ is small, therefore k varies like $1/\phi$, which represents a severe limitation on the accuracy of the system. To assess experimentally the influence of this factor on the measurement of the radial component, velocity measurements were performed in the glycerine tunnel at low temperature when the flow in the test-pipe is laminar. Whereas the standard deviation of the streamwise and circumferential components of velocity were typically between 0.5 and 0.6%, the radial component consistently gave a value greater than 5%. This result is in agreement with the result of the theoretical analysis, which predicts a tenfold increase in the amount of noise present in the on-axis component compared to other components. Therefore measurement of quantities such as turbulence intensity, Reynolds stress and higher-order statistical moments involving the radial velocity component were excluded. Attempts to measure the radial component of velocity in the turbulent regime gave unrealistic values for the Reynolds stress, thus confirming the results of the analysis.

As a consequence, we decided to use the standard two-component LDV system. With this system, we can measure only the streamwise and circumferential components of velocity. The optical arrangement is almost unchanged, except for the removal of the center green beam.

The standard two-component LDV is a backscatter system. It was observed that when the coincidence window (see appendix A) was set at the average size of a burst, the data rate was of the order of 100. Even though single-point measurement does not require a high data rate, the ability to resolve the largest frequencies in the flow was considered important. Moreover, it was anticipated that such a data rate would be too small for the measurement of two-point velocity correlations.

The main problem of backscatter systems is the presence of a high level of noise, with a signal to noise ratio typically over 50 times less than in forward-scatter systems. A burst detection scheme based on amplitude sets a limit on the maximum data rate attainable, because the gain must be kept low enough so that the background noise is rejected by the processor. In the case of a backscatter system with a low signal to noise ratio, this constraint is particularly harmful. An economical solution to increase the data rate is to use a forward scatter arrangement. Another advantage of forward scatter LDV systems is that they are not as sensitive to the presence of a wall, a crucial advantage in this study. Therefore a window was added on the other side of the pipe to allow optical access to a forward-scatter receiving optics module. An xyz translation stage was built and installed on a platform behind this new window. The photomultipliers were attached to the translation stage, and an additional receiving lens completed the receiving module. The axis of the receiving optics was set at approximately 10° to the horizontal, and 10° to the vertical, which allowed a more accurate identification of the beam crossing, without sacrificing too much scattered light.

Small air bubbles in suspension in glycerine constituted the seeding. The way air gets into the tunnel is not clear, but seems to be linked with the filling of the tunnel. The tunnel has a tendency to leak glycerine back into the glycerine tanks,

and it is thus necessary to refill it a little bit almost every day. This operation is thought to be the major cause of air bubbles in the tunnel. Whenever the bubble concentration in the tunnel is too small to provide an acceptable data rate, air is purposely introduced into the tunnel from a pressurized air line. The size of the bubbles was estimated visually from holograms of glycerine taken immediately after its removal from the tunnel. The diameter of the bubbles, measured by holography, varied between 20 and 50 μm ,i.e., 0.02 to 0.1 viscous wall units. Hinze (1955) gave a theoretical estimate of the size of gas bubbles in a turbulent liquid; he found that the maximum bubble size stable against breakup by turbulent eddies is:

$$d_1 \simeq \left(\frac{\sigma}{\rho}\right)^{3/5} \epsilon^{-2/5}$$

where σ is the surface tension, and ϵ the rate of turbulent energy dissipation. In the conditions of our experiment, this formula gives a maximum bubble size of $57\mu m$, in good agreement with the experimental result. Because the density of air is negligible compared to that of glycerine, the bubbles follow the flow perfectly. It can also be shown that convection and viscous forces on the bubbles are much larger than buoyancy forces. Attempts to use commercially available seeding particles with a well known size distribution centered around 4μm did not increase the data rate. This result is attributed to the presence of the larger bubbles in the flow, scattering light more efficiently than the small particles. Since the gain in the processors is set to avoid saturation of the electronics, signal from the smaller particles remains below detection level.

The Doppler signal observed on the oscilloscope had the characteristic shape of a burst in fringe mode laser anemometry, with an apparently good signal to noise ratio. This was only apparent because the electronic modules downmixing the signal after the photomultiplier (see appendix A) also remove the pedestal.

It is thus impossible to look at properties of the original Doppler signal such as its visibility. It is often believed that fringe mode laser Doppler anemometry can not work when the scattering particles are much larger than the fringe spacing. In the present case, the particle diameter is an order of magnitude larger than the fringe spacing. Calculations by Adrian and Earley (1975), using Mie scattering theory, show that "good signal to noise ratio can be obtained with particles much larger than the fringe spacing." The absence of experimental information on the signal visibility did not allow us to verify this claim. However, some runs were made after glycerine was passed through a filter with a 5 μm mesh size built in an auxiliary circuit of the facility. Commercially available particles (4 μm particles from TSI) were used; the single point statistics from these runs did not exhibit any significant difference with the runs made without filtering the glycerine.

The data rate obtained with the new LDV configuration typically varies between 1000 and 10000, depending on the location of the probe and the gain setting. By setting the gain so that the data rate was larger than 2000, the highest frequencies present in the flow could be resolved—recall that the largest frequency in the pipe have been estimated around 800 Hz. However, to avoid the simultaneous presence of particles in the probe volume, the data rate was kept less than 3000. Near the wall, where the velocities are of order u_τ, it corresponds to the presence of a particle in the probe volume approximately 25% of the time.

The LDV system is set up on a breadboard able to translate in all three directions. The position of the breadboard was chosen so that the LDV probe inside the pipe would lie in the horizontal plane passing through the pipe centerline, with its motion in the radial direction. The two other degrees of freedom of the breadboard were locked. A linear actuator with an accuracy of 10 μm was used to monitor the radial position of the breadboard. The motion

of the breadboard was accomplished with an anti-backlash screw. An eye-piece aligned with the optical axis allowed to position the beam crossing on the pipe wall, with an accuracy estimated at the length of the probe, i.e., 0.6 mm. Due to the change of index of refraction across the interface, a displacement y of the breadboard in the radial direction corresponded to a displacement $n\,y$ of the probe inside the pipe, where $n = 1.49$ is the index of refraction of acrylic. Note that the fringe spacing d_f is not changed across the interface. If λ and ϕ are respectively the wavelength of the beams and their angle, the fringe spacing is given by:

$$d_f = \frac{\lambda}{2\,sin(\phi/2)}$$

Since $sin(\phi/2)$ and λ follow the same law across the interface, d_f remains unchanged.

2.6 Mean Velocity Profile

Figure 7 shows the mean streamwise velocity normalized by the centerline velocity, as a function of the wall distance normalized by the pipe radius. Data obtained by Herzog (1986), using a split film in the wall region and a pitot tube in the center of the pipe, are shown for comparison. The location of the wall was found by taking the intersection of the least-square fit of a straightline with the first five points with the horizontal axis. The shift at the origin was $\Delta y = 0.65$ mm, about one viscous length. In addition, the slope of the straight line gives the velocity gradient at the wall, which in turn can be converted into the friction velocity u_τ; the value $u_\tau = 0.43$ m/s was found, in good agreement with the reference value $u_\tau = 0.40$ m/s computed from the pressure gradient.

The friction velocity was also calculated from the velocity distribution in the log-region using a least-square fit to the following universal profile (Tennekes and

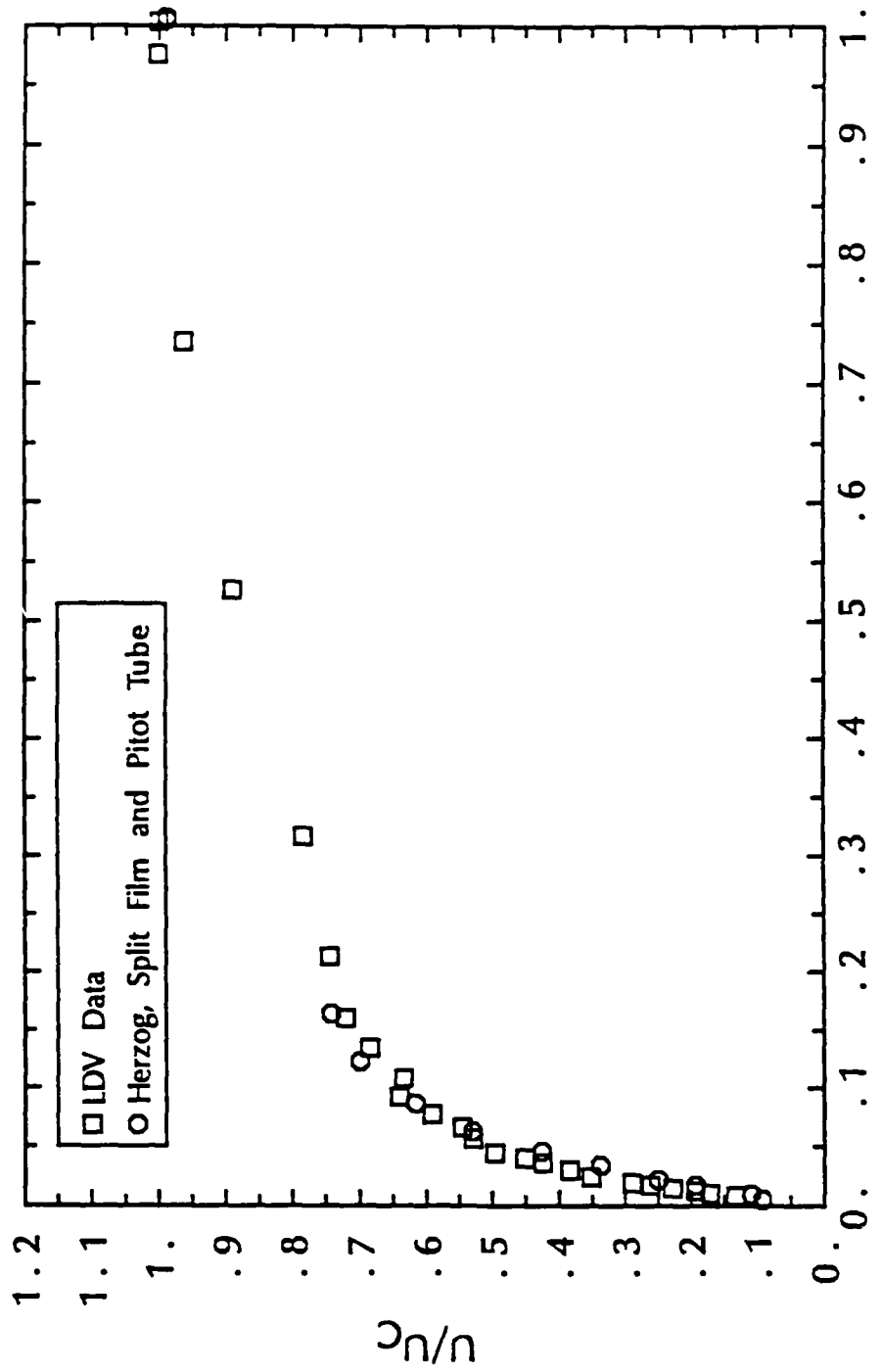

FIGURE 7
Mean Velocity Distribution across the Pipe

Lumley, 1972):

$$u^+ = y^+, \text{ when } y^+ < 5.0$$

$$u^+ = 2.5 ln y^+ + 5.5, \text{ when } y^+ > 30.0$$

The origin of ordinates was taken equal to that previously computed. The friction velocity was found equal to $u_\tau = 0.39$ m/s. Figure 8 is a plot of the velocity in the near-wall region in semi-log coordinates, non-dimensionalized with this value of the friction velocity.

The bulk velocity was calculated by integrating the velocity profile across the pipe. The value $U_{av} = 6.34$ m/s was found, in good agreement with the value the value of the mean velocity at the quarter radius (Tennekes and Lumley, 1972). This last method yields the value $U_{av} = 6.44$ m/s. The Reynolds number based on the diameter and $U_{av} = 6.34$ m/s is $Re_d = 8923$. The value of the friction velocity obtained by substituting $U_{av} = 6.34$ m/s in equation 2.1 is $u_\tau = 0.405$ m/s, in excellent agreement with the value computed from the pressure drop.

2.6 Measurement of Velocity Correlation

The measurement of the two-point velocity correlations was accomplished with the two-component LDV complemented by a one-component fiber-optics LDV. A detailed description of the setup is given in appendix A. For convenience, we denote the probe of the two-component system, which moved only in the radial direction, as the "fixed" probe while the probe of the fiber-optics system is called the "moving" probe. Two traverse mechanisms were designed for the moving probe. Both provided translation in all three directions, rotation about a line parallel to the axis of the pipe, and rotation about a direction parallel to its own optical axis. The range of motion was 450 :nm in the streamwise direction and 35 mm in the radial direction.

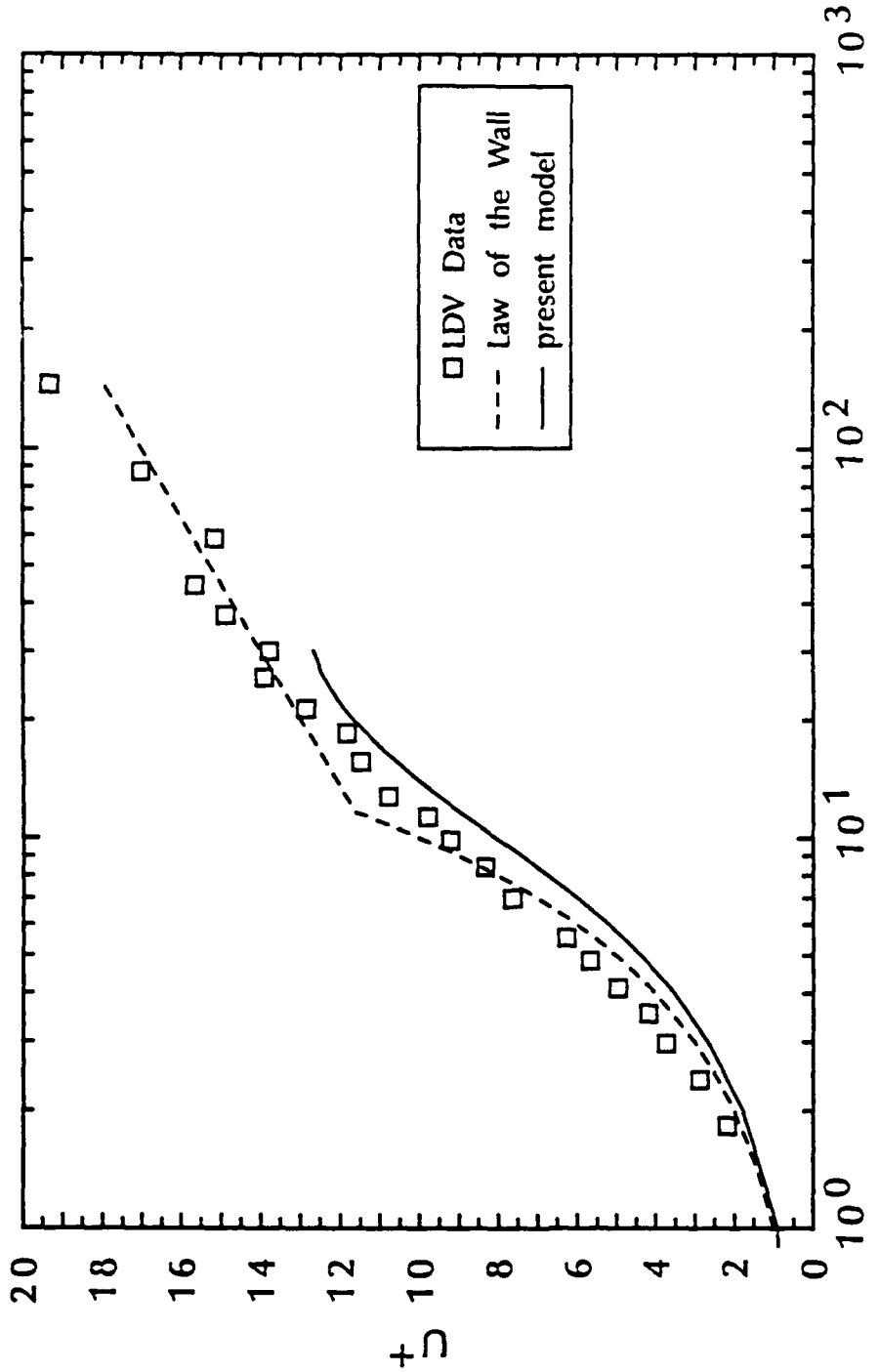

FIGURE 8
Mean Velocity Distribution near the Wall

In the initial setup, the beams of the moving probe were shot into the pipe horizontally, i.e., parallel to the axis of the two-component system. In this configuration, the vertical range was 300 mm. By rotating the probe head about its own axis, it was possible to measure either the streamwise or the circumferential velocity component. This setup created a serious problem close to the wall, where the velocity gradient is large over the length of the probe volume (l_m = 2.4mm = 5 viscous units). The velocity gradient bias can be approximately corrected when the streamwise velocity is known, but since the fiber-optics system gives access to only one component of velocity, no correction for the radial velocity can be used.

In the second configuration, the beams of the moving probe are shot into the pipe vertically through the top window. In this case, the vertical range was only 35 mm. The two components of velocity measurable in this setup are the streamwise and the radial components. The diameter of the probe volume (d_m = 0.11 mm) is small so that the velocity gradient bias in the radial direction can be neglected. In the circumferential direction, the probe length is 2.4 mm, approximately 5 viscous units. However, since the radius of the pipe is much larger than the length of the probe, the velocity change in the direction of the probe is small. Thus the velocity gradient bias in the circumferential direction is negligible. This setup was used for the remaining of this study.

The procedure for the measurement of the two-point velocity correlations was as follows:

- The fixed probe was moved to a new location in the radial direction, corresponding to one of the following distances from the wall: y^+ = 2, 3, 6, 9, 12, 18.

- For each of the fixed probe locations, the moving probe was moved to a new position with a streamwise separation Δx^+, and a radial separation Δy^+. The separation distances were increased logarithmically. The increments near the wall and near the probe were always chosen as small as possible, usually $\Delta x^+ = 2$ and $\Delta y^+ = 1$. For example, when the fixed probe was at $y^+ = 12$, the positions relative to the fixed probe were:

$$\Delta y^+ = -11, -10, -8, -4, -2, -1, 0, 1, 2, 4, 8, 16, 32, 52$$

giving absolute positions of:

$$y^+ = 1, 2, 4, 8, 10, 11, 12, 13, 14, 16, 20, 28, 44, 64$$

The maximum distance of the moving probe from the wall can not exceed $y^+ = 64$.

The streamwise separation was as large as the setup allowed, i.e., $\Delta x^+ = 830$. This is about 50% larger than in Herzog's experiment (1986), and corresponds approximately to the observed length of the wall streaks. The maximum radial separation of the two probes, 64 wall units, is also 50% larger than that of Herzog. This allowed us to identify the turbulent structures further away from the wall.

Even in a simple geometry, like a pipe flow, it is difficult to locate precisely the probe volume of an LDV. The procedure described previously for the determination of the position of the fixed probe allowed the present measurements to be performed with an accuracy estimated at one viscous length. For the correlation measurements, the moving probe was first aligned with the fixed probe. Coincidence of the two probes was checked with a telescope. Then the moving probe was moved to its new position relative to the fixed probe. At large separation, when the correlation coefficient varies slowly with distance,

inaccuracies in the alignment procedure are not critical. At zero or small separation, when the correlation coefficient varies substantially with distance, the effect is more important. However, Reynolds stress measurements presented in the next chapter do not seem to be affected by this problem and compare well with previous measurements.

The length of the fiber-optics probe ($l_m \simeq 5$ wall units) represented another potential difficulty, namely the lack of accuracy in correlation measurements. Experimental results presented in the next chapter showed that this was not a major problem. Presumably this is due to the fact that the integral length scale in the circumferential direction (about 40 wall units) is much larger than the size of the probe. Blackwelder and Haritonidis (1983) found that the maximum probe size in the wall region should not exceed 20 wall units. The size of the fiber-optics probe, measured in wall units, is smaller than this limit; in fact it is smaller than any hot wire or hot film probe used in previous investigations in air or water, because of the use of glycerine.

The data rate from the one-component fiber-optics LDV rarely exceeds 500. Therefore the limiting factor for the data rate in the two-point correlation measurements was the data rate from the fiber-optics system. Velocity bias was an obvious concern in this study. The large turbulence intensity near the wall, and the low data rate are two factors that are usually considered to increase velocity bias (Edwards, 1981). A simple model was devised to study the effect of velocity bias on the mean velocity and correlation coefficient. The model and the numerical results are presented in appendix C. Our conclusions are that while the mean velocities can be significantly affected by velocity bias (up to 50% of the RMS value), the correlation coefficient is not affected by more than 4%.

2.8 Data Analysis

A software package was written for the analysis of the LDV data. Computer memory limitations restricted the number of data points to less than 6000 per channel for every run. Immediately following the end of a run, velocity statistics were calculated and displayed for inspection. They include:

- Test, run number and position of the fixed probe volume.
- Data rate, and minimum and maximum time between data points.
- Mean velocity, standard deviation, turbulence intensity, skewness and flatness factor for each channel.
- The three cross correlation coefficients: 1-2, 2-3, and 1-3.
- Minimum and maximum velocity values on each channel.
- Low and high filter values for each channel.

Two types of filters were available. The first filter, the crudest, was used to discard the data well out of the range of a realitic velocity distribution. To accomplish this, the velocity distribution of each channel was plotted on the computer terminal and a low and a high filter value were manually entered. The new statistics were computed after discarding the points outside the filter limits.

The second step consisted of a two-dimensional filter based on the fact that the u-v (or v-w, or u-w) distribution has an elliptical shape in the u-v plane. From the second-order statistics of the u-v distribution it is easy to compute the principal axes of the distribution as well as their length. A Gaussian velocity distribution would be completely characterized by these quantities—or

equivalently, the "1-sigma" ellipse they define—and the velocity statistics could be estimated with a given confidence level.

In reality, the u-v distribution is not Gaussian, so filtering can not be performed this way. A filtering ellipse was specified by expanding the 1-sigma ellipse by a factor k. The coefficient k was chosen between 6 and 9, a conservative value compared to the values usually mentioned in the literature (between 4 and 6 for the one-dimensional filter). All points located outside this ellipse were discarded. To check the validity of the procedure, a two-dimensional contour plot of the velocity distribution was displayed on the computer terminal, with the rejected points identified by a cross (figure 9). The effectiveness of the filter was left to the appreciation of the user. This two-dimensional filter is particularly efficient when noisy data, located away from the rest of the distribution in the u-v plane, appears acceptable to a one-dimensional filter.

A similar three-dimensional filter, based on the complete 3×3 Reynolds stress tensor, is feasible. However, our experience shows that visual inspection of the filtered data is an essential step in the procedure, and visualizing the velocity distribution in three dimensions is not an easy task. Therefore no effort was spent in this direction.

The rejection rate depends on the location of the probes. Very near the wall, up to 3 or 4% of the data can be rejected; away from the wall, this rate is always lower than 1%. Each measurement most often involves taking 4000 data points at a given location, which means that usually more than 3950 points are used for the calculation of the statistics. The effect of the one-dimensional filter is most felt on the estimate of the standard deviation, skewness and kurtosis factors, while the two-dimensional filter affects especially the cross-correlations.

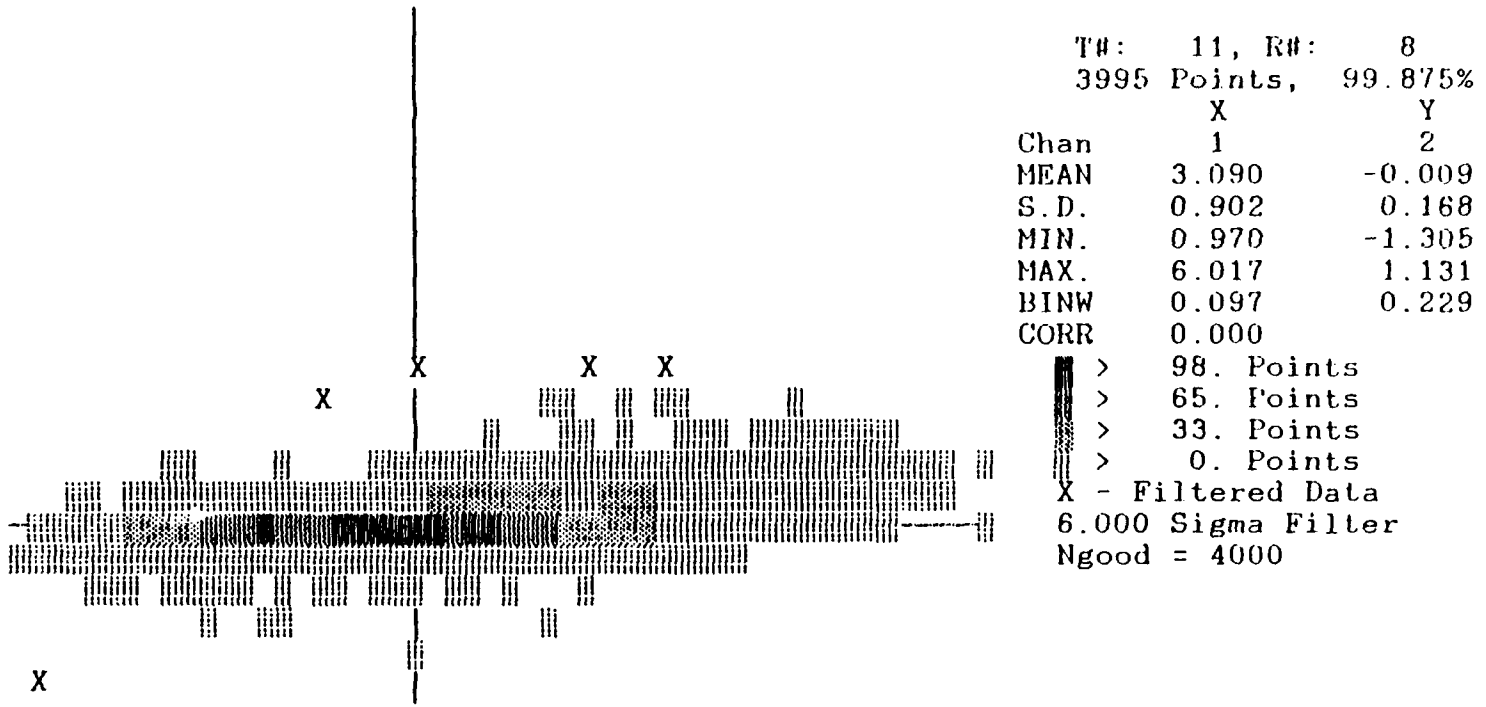

FIGURE 9
Computer Display of $u - v$ Velocity Distribution
horizontal axis = u-velocity
vertical axis = v-velocity

Chapter 3

EXPERIMENTAL RESULTS

3.1 Introduction

In the previous chapter, we presented the facility, the experimental technique and some basic measurements—pressure drop, flow-rate and mean velocity distribution. This chapter will emphasize experimental results relative to the structure of turbulence in the near-wall region. Higher-order moments of velocity and two-point correlations will be presented. Since this study focuses on the behavior of turbulence in the wall region, the non-dimensionalization of the data has been done systematically in terms of the inner variables ν and u_τ (obtained from the pressure drop measurements).

First, single-point measurements are presented and compared with previous data. The Reynolds stress results are emphasized, because they provide a good test of the problems encountered during correlation measurements. Two-point correlation measurements are detailed in a following section. The interpretation of these results is then presented.

3.2 Single-point Measurements

3.2.1 Velocity Statistics

Standard deviation of the streamwise, circumferential and radial components of velocity are presented on figures 10, 11 and 12, respectively. These data were

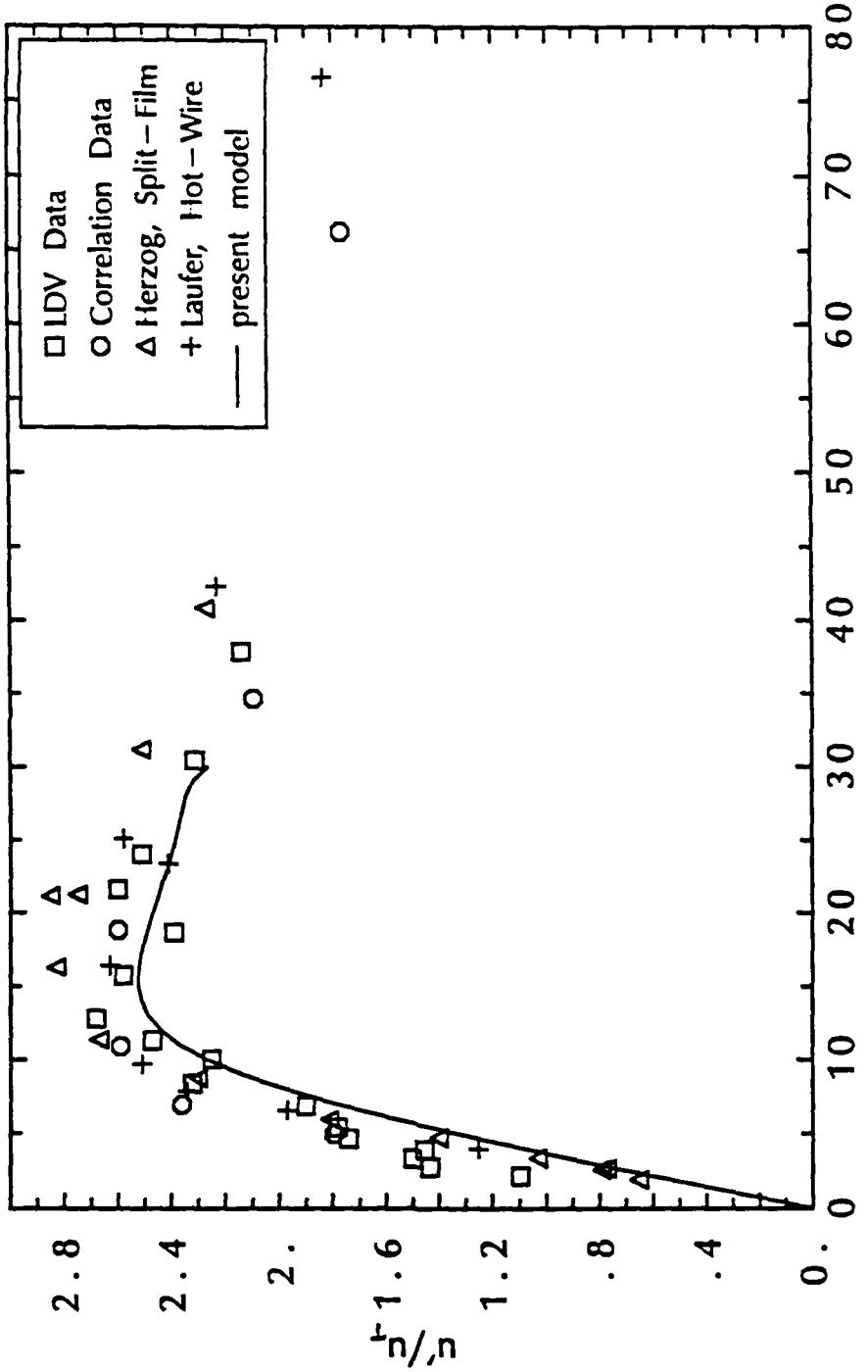

FIGURE 10
Near-Wall Distribution of
Standard Deviation of Streamwise Velocity

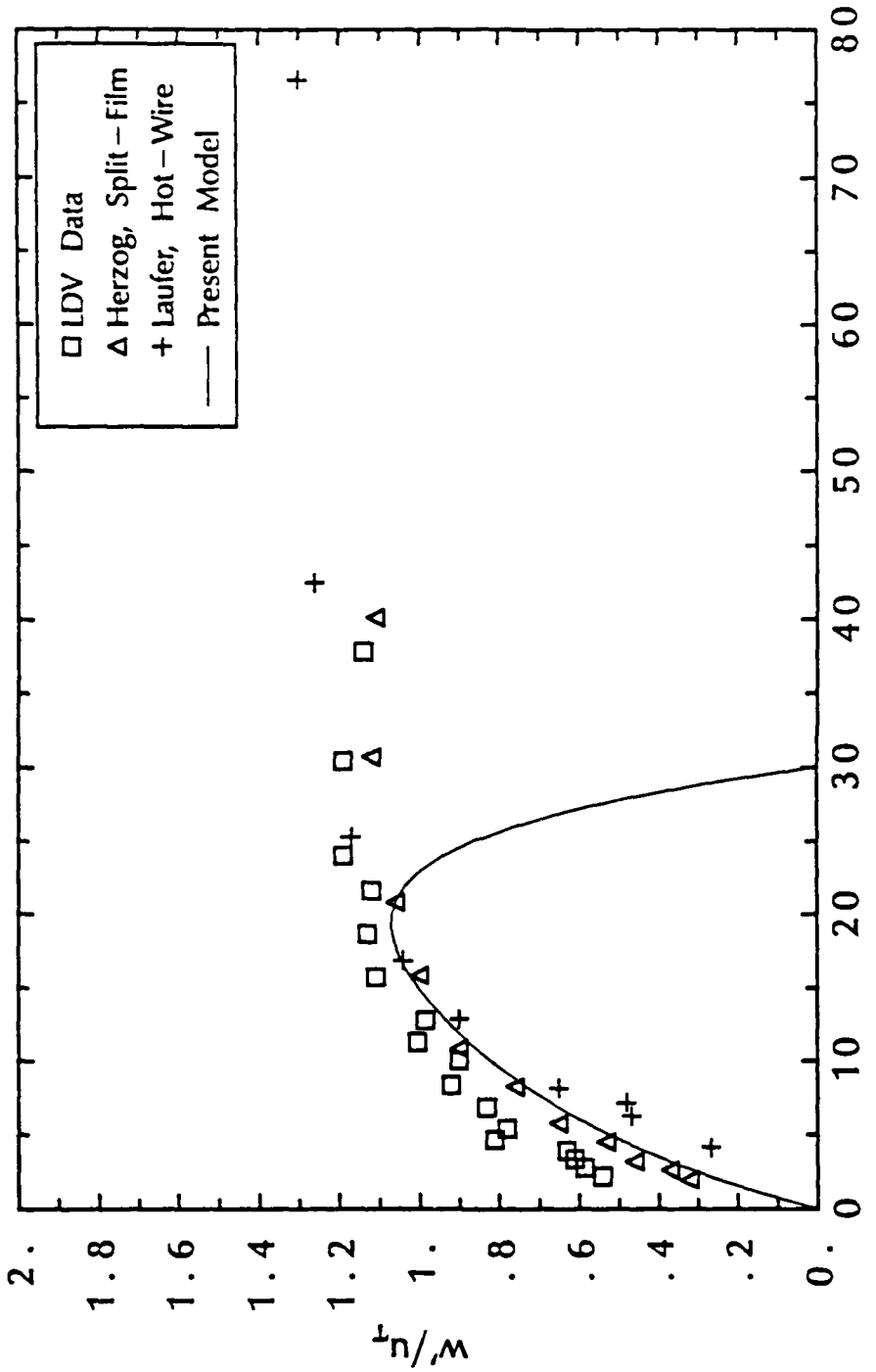

FIGURE 11
Near-Wall Distribution of
Standard Deviation of Circumferential Velocity

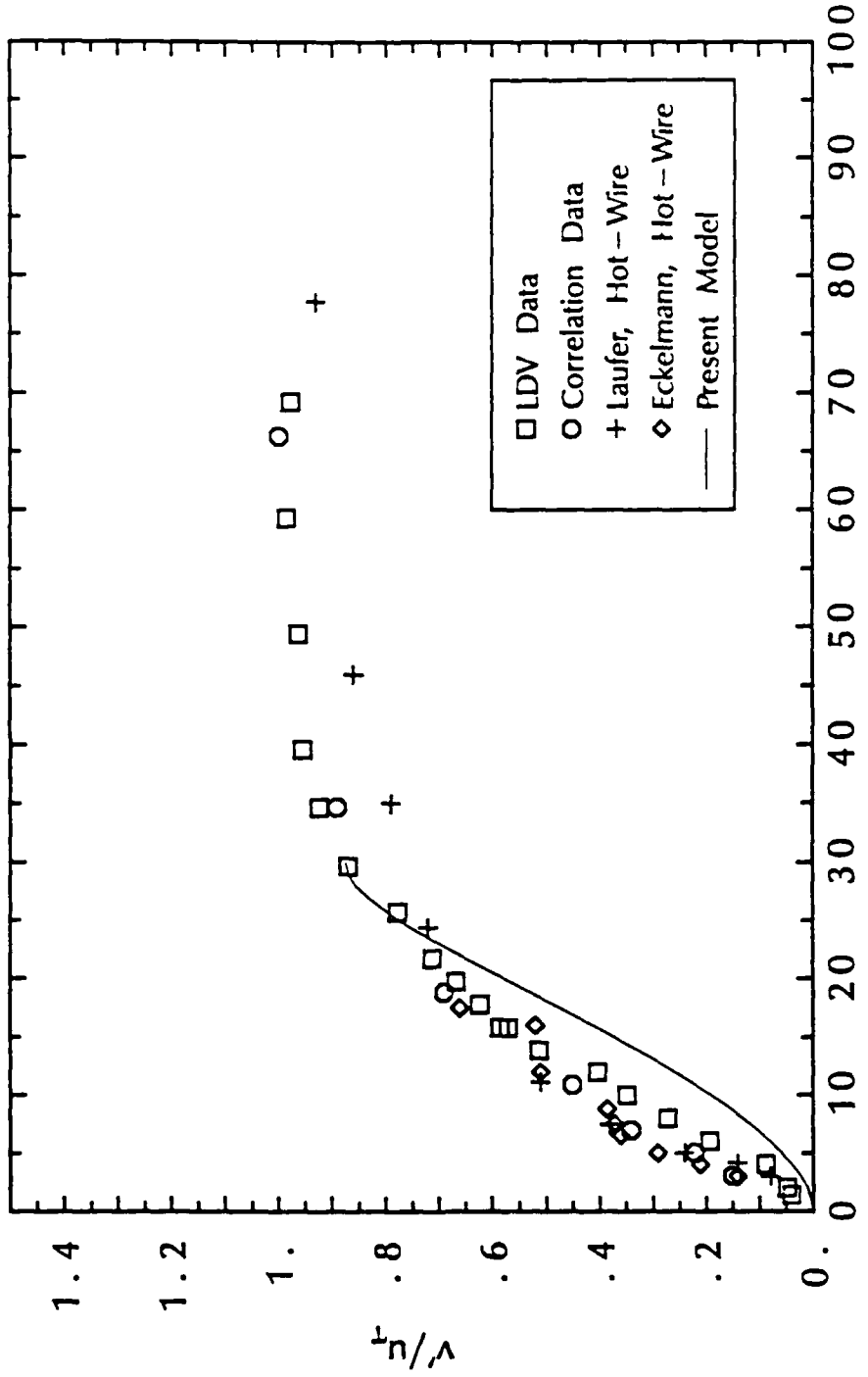

FIGURE 12
Near-Wall Distribution of
Standard Deviation of Radial Velocity

obtained either from single-point measurements ("LDV data"), or from the two-point measurements described in the following section ("Correlation data"). The two sets of data are in good agreement with each other.

Herzog (1986) measured the streamwise and circumferential RMS velocities in the glycerine tunnel at the same Reynolds number. He used split films (length of the films$\simeq$0.5 wall unit) with an inverse calibration procedure which is described in his thesis. Laufer measured the three components of velocity in a pipe at Reynolds numbers of 50,000 and 500,000. The fluid was air and hot wires (length of the wires$\simeq$5 wall units) were used for the measurements. In the logarithmic region, the present results are in good agreement with Laufer's data, while Herzog's data seem slightly too high. In the viscous sublayer, the RMS streamwise and circumferential velocity are slightly higher than Laufer's and Herzog's data. The small difference could be caused by velocity gradient bias due to the size of the two-component LDV probe: its length is about one wall unit, representing a mean velocity variation of approximately $u_\tau = 0.4$ m/s across the probe; this is the order of magnitude of the difference between the present results and Herzog's data. Very near the wall, Laufer's hot wire data are low, either because his hot wire was too large or because it might have been contaminated by the proximity of the wall, producing lower values of the circumferential RMS velocity. The present study finds the peak of the streamwise RMS velocity near $y^+ = 17$, in agreement with the results of Laufer (1954) and Herzog (1986).

The radial RMS velocity distribution (Figure 12) is compared with Laufer's and Eckelmann's data (1972). Eckelmann performed his measurements in an oil channel at a Reynolds number of 8200. Agreement with his results is good. Beyond $y^+ = 20$, the present data reach the asymptotic value $v/u_\tau = 1$ faster

than Laufer's. Near the wall, the present data are slightly smaller than in previous investigations although the distribution is linear, in agreement with theoretical estimates.

The distribution of the skewness factor in the wall region is shown on figure 13. Because of the axial symmetry of the flow, the skewness of the circumferential component of velocity must be zero. Indeed, the measured value is small, typically less than 0.2 in absolute value. The skewness of the streamwise component is positive close to the wall and negative away from the wall. This behavior can be easily interpreted: close to the wall, the velocity distribution is centered on a small value, bounded immediately below by zero and bounded above by a comparatively very large value. In contrast, away from the wall, the velocity distribution is centered on a large value, bounded above by the maximum velocity, and bounded below by a comparatively very small value. On the pipe centerline, the skewness must be zero for symmetry reasons. The distribution of the skewness of the radial velocity is very different: after starting at zero close to the wall, it reaches a negative peak between $y^+ = 10$ and 20, and returns to zero past this region. The peak corresponds to the buffer zone, where most of the turbulent production takes place, and is probably due to the intermittent character of the motion. The negative sign indicates that the distribution is skewed towards negative values of the radial velocity. Thus excursions far from zero are stronger towards the wall than away from it. In the same region, the streamwise velocity distribution is also skewed towards negative values, indicating that excursions far from the mean are stronger for negative fluctuations than for positive fluctuations. This result is somewhat surprising, because the Reynolds stress involves excursions away from the mean by streamwise and radial velocity fluctuations of opposite signs. These behaviors

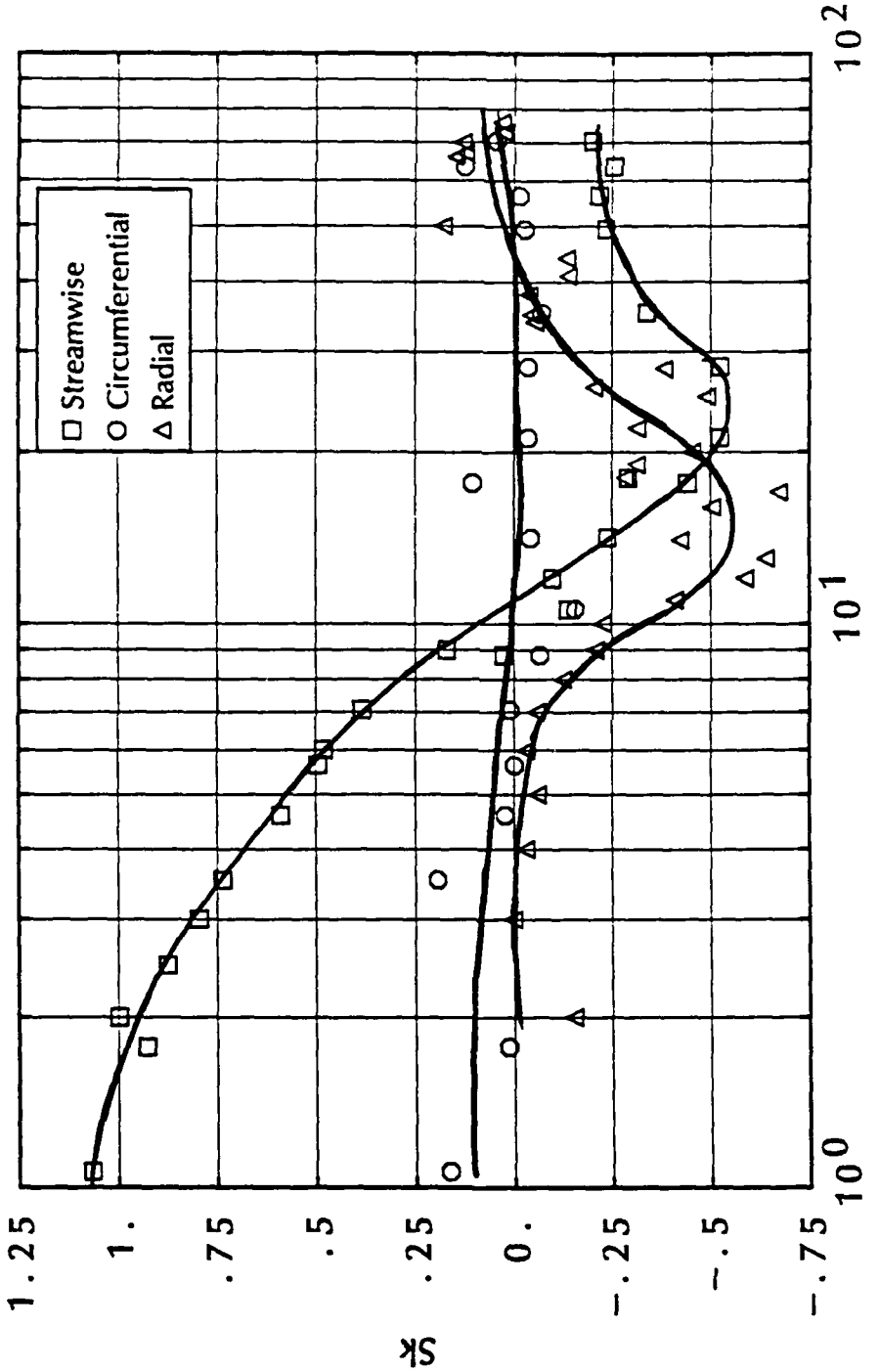

FIGURE 13
Near-Wall Distribution of
Velocity Skewness

are in no way incompatible, though, and can be interpreted in the following simple fashion: the two-dimensional $u - v$ distribution, in addition to presenting a strong negative correlation in the direction of the major axis (i.e. the line $u = -v$), is skewed in the direction of the minor axis (i.e. the line $u = v$), towards the third quadrant.

The distribution of the flatness factor shown on figure 14 confirms the previous remarks in many ways. The streamwise and circumferential velocity components have large values close to the wall and decrease to the Gaussian value of 3 in the logarithmic layer. The large value of the flatness factor near the wall can be attributed to the intermittent character of the velocity field in the wall region. The flatness of the radial velocity exhibits a strong peak between $y^+ = 8$ and 15, indicating a strongly non-Gaussian behavior in this region. But again, as for the skewness, it seems to possess a Gaussian distribution in the viscous sublayer, unlike the streamwise and circumferential velocities. These results indicate that the combination of the wall and predominant viscous effects exert a strong damping on this component below $y^+ = 8$. Thus excursions of the radial velocity far from its mean value are unlikely very close to the wall, unlike what is observed for the streamwise velocity. Intermittent behavior of u and v are usually linked in the near-wall region, but the present results show that below $y^+ = 8$, u is intermittent while v is not: That is the intermittent behavior of v does not reach as far into the viscous sublayer as that of u. The asymptotic behavior of the Reynolds stress close to the wall—which will be shown to vary like y^3, not y^2, in the next section—should probably be attributed to this feature of the radial velocity close to the wall.

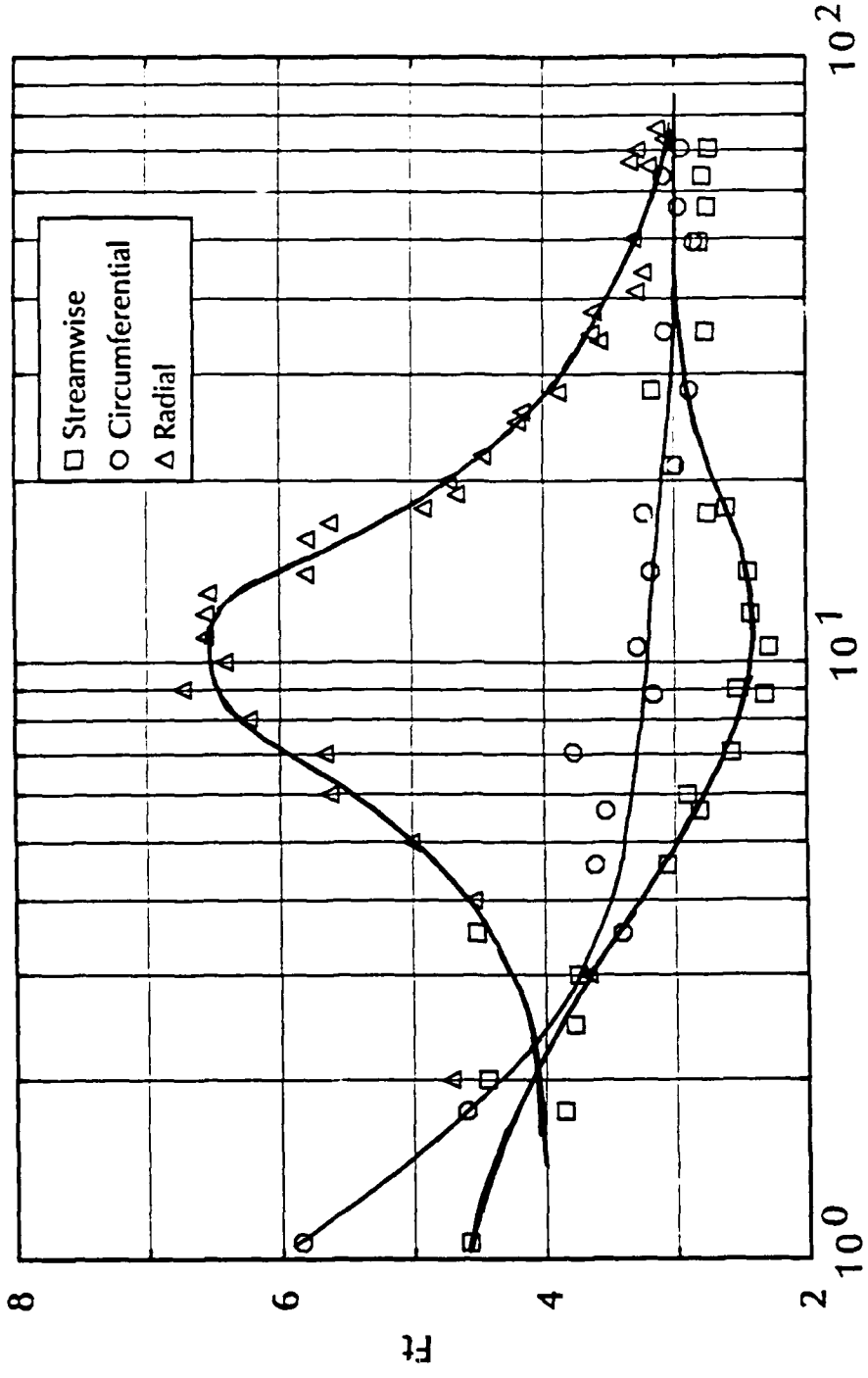

FIGURE 14
Near-Wall Distribution of
Velocity Flatness

3.2.2 Single-point Correlation results

Two methods were used to determine the ability of the system to measure velocity correlations.

In a first step, the two probes were placed at the same point and the fiber-optics LDV was oriented so as to measure the streamwise velocity. The correlation coefficient between the streamwise velocities measured from the two systems thus fell between 93% and 99%, a satisfactory result considering that it is a second-order statistic.

As a second method of checking the accuracy of correlation measurements we kept the two probes at the same location but rotated the fiber-optics probe so that it could measure the radial velocity. We were thus able to measure the Reynolds stress distribution, and to compare it with that computed from the mean velocity distribution across the pipe (Laufer, 1954). Combining the continuity equation with the streamwise and radial momentum equations written in cylindrical coordinates, one gets:

$$-\frac{\overline{uv}}{u_\tau^2} = (1 - \frac{y^+}{R^+}) - \frac{dU^+}{dy^+} \tag{3.1}$$

The mean velocity gradient can be estimated using the mean velocity distribution shown on figure 8. Using the value of u_τ given by the pressure gradient, the non-dimensional value of the velocity gradient $\frac{dU^+}{dy^+}$ can be computed. Substitution in equation 3.1 thus provides the Reynolds stress.

To compute the Reynolds stress distribution very near the wall, the mean velocity was assumed to follow the asymptotic form:

$$U^+ = y^+ + \alpha y^{+2} + \beta y^{+3} + \gamma y^{+4} + \delta y^{+5} + O(y^{+6})$$

where α, β, γ and δ are constants to be determined. Substitution into equation 3.1 yields:

$$-\frac{\overline{uv}}{u_\tau^2} = -(\frac{1}{R^+} + 2\alpha)y^+ - 3\beta y^{+2} - 4\gamma y^{+3} - 5\delta y^{+5}$$

It can be shown that the coefficients of y^+ and y^{+2} in this equation must cancel. Chapman and Kuhn (1986) expand the instantaneous fluctuating velocities in a Taylor series near the wall:

$$u = a_1(x,z,t)y + ...$$

$$w = b_1(x,z,t)y + ...$$

By substitution in the continuity equation, one gets:

$$\frac{\partial v}{\partial y} = -\left(\frac{\partial a_1}{\partial x} + \frac{\partial b_1}{\partial z}\right) y + ...$$

Integration and multiplication by u yield:

$$-\overline{uv} = \left(\frac{1}{2}\overline{\frac{\partial a_1^2}{\partial x}} + \overline{a_1 \frac{\partial b_1}{\partial z}}\right) \frac{y^3}{2} + ...$$

Since the flow is fully developed in the streamwise direction, the first term inside the parenthesis is zero. Therefore:

$$-\overline{uv} = \overline{a_1 \frac{\partial b_1}{\partial z}} \frac{y^3}{2} + ... \qquad (3.2)$$

The leading term of the Taylor expansion for the Reynolds stress near the wall is thus proportional to y^3 and we must have:

$$\alpha = -\frac{1}{2R^+}$$

$$\beta = 0$$

γ and δ can be found by computing a least square fit to the experimental mean velocity profile of figure 8 for y^+ varying between 0 and 10. γ was found equal to

$-3.052\,10^{-4}$, and δ to $1.67\,10^{-5}$. The final result for the Reynolds stress behavior near the wall is:

$$-\frac{\overline{uv}}{u_\tau^2} = 1.22\,10^{-3}y^{+3} - 8.35\,10^{-5}y^{+4}$$

The Reynolds stress distribution beyond $y^+ = 5$ was computed using a cubic spline of the mean velocity profile, and taking its derivative. Comparison of the computed distribution with the measured distribution of Reynolds stress is shown in figure 15. The two curves are in good agreement. Eckelmann's data are also shown on this figure. Agreement with his data is very good. Repeatability tests yielded a scatter of about 10% in the value of the Reynolds stress.

The good agreement between theoretical and experimental results obtained in our measurement of single-point auto- and cross-correlations proved the effectiveness of the correlation measuring technique using two LDVs.

3.2.3 On Calculating the Reynolds Stress from the Mean Velocity Distribution

Some care must be taken in calculating the Reynolds stress distribution from the mean velocity distribution. In the following, we show how the misuse of Spalding's formula, or a small error in the estimate of the friction velocity can lead to incorrect results close to the wall.

Using Spalding's semi-empirical formula (1961) relating y^+ and U^+ in a turbulent boundary layer, together with the momentum equation 3.1, gives an erroneous result. Spalding's formula is:

$$y^+ = U^+ + e^{-\kappa B}\left(e^{\kappa U^+} - 1 - \kappa U^+ - \frac{(\kappa U^+)^2}{2} - \frac{(\kappa U^+)^3}{6}\right)$$

where κ is the von Karman constant and B is the additive constant appearing in the law of the wall. A Taylor series expansion of this expression around $y^+ = 0$

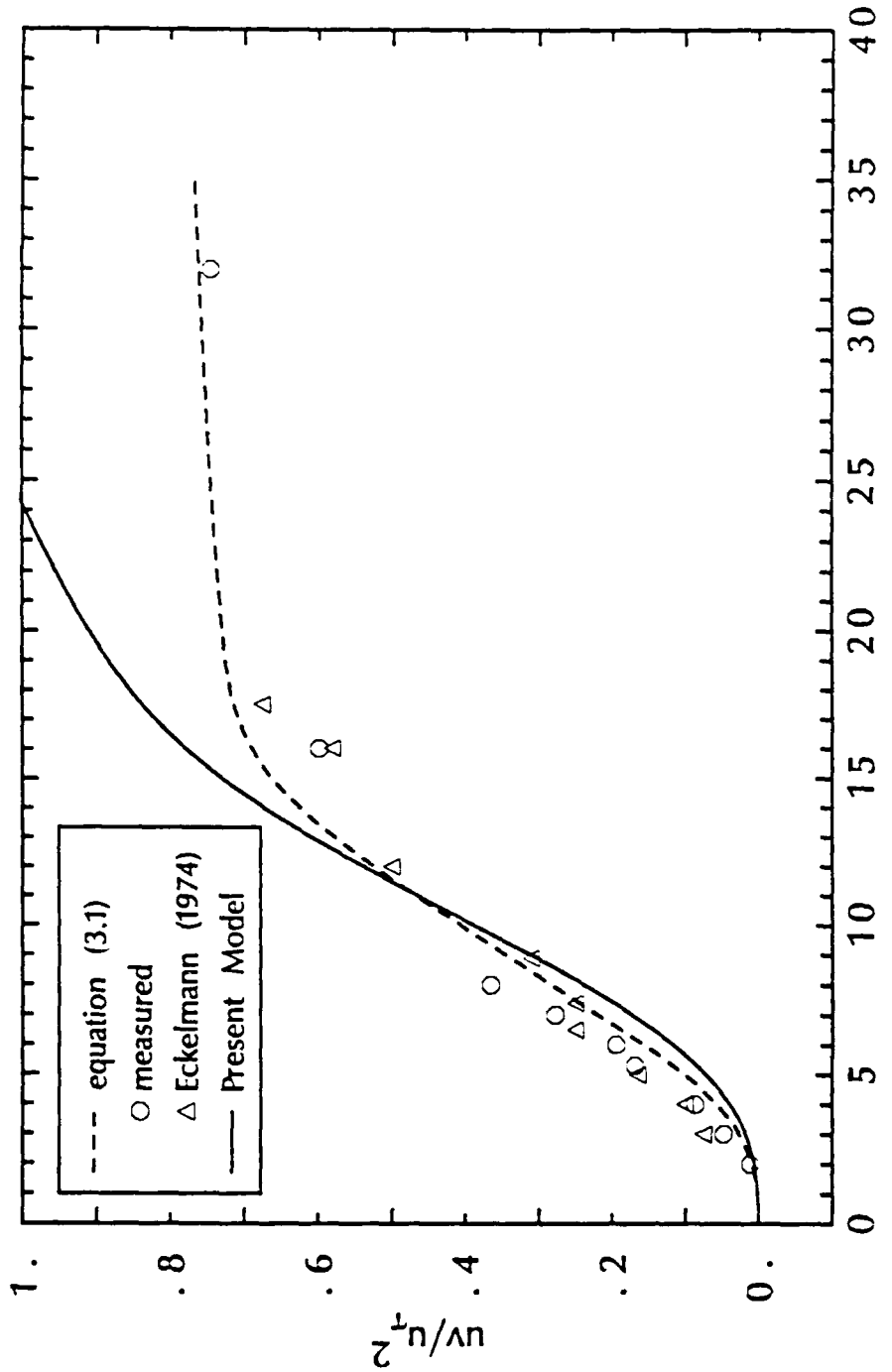

FIGURE 15
Near-Wall Distribution of
Reynolds Stress

provides an expression for the velocity as a function of the distance from the wall:

$$U^+ = y^+ - \frac{e^{-\kappa B}}{24} y^{+4} + O(y^{+5})$$

Now taking the derivative of this expression, we get:

$$\frac{dU^+}{dy^+} = 1 - \frac{e^{-\kappa B}}{6} y^{+3} + O(y^{+4}) \tag{3.2}$$

Substituting in equation 3.1, we find for the Reynolds stress near the wall:

$$-\frac{\overline{uv}}{u_\tau^2} = -\frac{y^+}{R^+} + \frac{e^{-\kappa B}}{6} y^{+3} + O(y^{+4})$$

According to this result, the Reynolds stress should change sign near the wall. This erroneous conclusion is due to the inapropriate use of Spalding's formula in a flow with a pressure gradient. A first-order term y^+ should be added to the formula to take into account the pressure gradient.

Durst et al. (1985) performed Reynolds stress measurements in a pipe and found negative Reynolds stress near the wall. This result is incorrect, as well as the theoretical explanation for it: the Taylor series for the mean velocity they used in equation 3.1 included only one term, whereas it should include terms up to fourth order, because terms up to third order cancel out. It is shown in the following that their experimental result can be explained by an inaccurate determination of the friction velocity. For example, if it is assumed that the measured friction velocity differs from the actual friction velocity by a relative error ϵ, the non-dimensionalized distance and velocities thus obtained are:

$$U^+ = \frac{1}{(1+\epsilon)} \frac{U}{u_\tau}$$

and

$$y^+ = (1+\epsilon) \frac{y u_\tau}{\nu}$$

The mean velocity gradient computed from figure 8 is then:

$$\left(\frac{dU^+}{dy^+}\right)_{comp} = \frac{1}{(1+\epsilon)^2}\frac{dU^+}{dy^+}$$

Substitution into equation 3.1 yields:

$$\left(-\frac{\overline{uv}}{u_\tau^2}\right)_{comp} = 1 - \frac{y^+}{R^+} - \frac{1}{(1+\epsilon)^2}\frac{dU^+}{dy^+}$$

After expansion with respect to ϵ, this equation becomes:

$$\left(-\frac{\overline{uv}}{u_\tau^2}\right)_{comp} = [1 - \frac{y^+}{R^+} - \frac{dU^+}{dy^+}] + \epsilon[2\frac{dU^+}{dy^+}] + O(\epsilon^2)$$

The absolute error on the Reynolds stress is thus proportional to the mean velocity gradient. Since this quantity reaches its highest value at the wall, this is where the effect of inaccuracies in the estimation of u_τ is the most sensitive, and an estimate of the friction velocity smaller than the actual value can produce erroneous negative values of the Reynolds stress near the wall. Extreme care should be taken in the measurement of the friction velocity when formula 3.1 used for the estimation of the Reynolds stress distribution near the wall.

3.3 Two-point Correlation Measurements

Two-point correlations have been measured across the wall region, for six locations of the fixed probe: y^+=2, 3, 6 , 9, 12 and 18. In every case, the angle θ characterizing the circumferential separation was zero, i.e. the moving probe stayed in the horizontal plane passing through the centerline. The moving probe was oriented to measure the radial component of velocity. Since the correlation between circumferential and radial velocity is zero in this plane, only

the streamwise component of velocity was measured with the fixed probe. The correlation coefficient which was measured is thus:

$$R_{12}(y^+;\Delta x^+,\Delta y^+,0) = \frac{\overline{u(0,y^+,0)\,v(\Delta x^+,y^+ + \Delta y^+,0)}}{\sqrt{\overline{u^2}}\sqrt{\overline{v^2}}}$$

To our knowledge, this quantity has never been measured in the viscous sublayer and buffer layer. Herzog (1986) could not measure it directly and computed its Fourier transform from the Fourier transform of the components R_{13} and R_{23} using the continuity equation. His computations were not available to us.

At zero separation, R_{12} is equal to the non-dimensional Reynolds stress, i.e., the term which represents turbulent momentum transfer from the mean flow in the Reynolds averaged equations. Therefore R_{12} provides a measure of the size of the eddies by which this transfer occurs. In the following of the discussion, we will refer to these eddies as the Reynolds stress eddies.

The correlation coefficient R_{12} is a statistical quantity which gives an average picture of the Reynolds stress eddies. Pathological situations might exist where the average picture given by the correlation coefficient is not representative of the individual elements that have been used to compute it. As pointed out by Willmarth (1978), the correlation may thus hide rather than reveal the physics of the flow. This could be the case in the wall region, where many seemingly different events have been observed and classified. However, there are also reasons to believe that the correlation coefficient should give a fair picture of the Reynolds stress eddies in the wall region. The universal appearance and scaling of the turbulent eddies in a turbulent boundary layer suggests that the flow, on the average, is not as complicated as flow visualization, or even a hot-wire signal would suggest. The visual observations of Head and Bandyopadhyay (1981) in the outer part of a turbulent boundary layer, for example, show that the

structure of the boundary layer is on the average made of horseshoe or lambda vortices, thus much simpler than originally thought. In addition, not all eddies contribute equally to R_{12}; in fact it has been shown that most of the Reynolds stress production comes from bursts and that the contribution of other types of eddies is much smaller (Kline et al., 1967). These observations thus make it likely that the correlation coefficient R_{12} is a fair representation of the Reynolds stress eddies.

Interest in the correlation measurements is two-fold. On the one hand, one of the most important problems in turbulence is the spatial characterization of turbulent eddies. This can be seen in the fact that turbulence models have to be tuned to every flow situation they are supposed to "predict," because turbulence reacts differently to different types of boundary conditions. On the other hand, most researchers agree that practical models will have to rely on statistical averaging for some time to come. Thus from the point of view of theoreticians, the measurement of the correlation coefficient is useful because it tells how, on the average, turbulence spatially adjusts to the presence of the wall.

Some experimentalists argue that the only way to understand the mechanisms of turbulence is to look at individual eddies. It is true that looking at individual eddies helps to characterize turbulence. Unfortunately, it seems to be a subjective approach which asks almost as many questions as it answers. In fact, the statistical and the deterministic approaches complement each other, their common goal being to find an "average deterministic turbulent process." Our understanding of turbulence is neither purely deterministic, nor purely random.

The statistical approach we have followed in this study does not let us identify directly the structures contributing to the correlation coefficient. However,

observation of the contour plots provides a number of clues which, combined with visual observation of other authors, suggest a possible interpretation which will be explained after the following presentation of the data.

The calculation of R_{12} involves the measurement of three quantities: u, v, and their correlation $\overline{uv}$. The relative accuracy of the u and v measurements is estimated at 10%. In addition to depending directly on u and v, the two-point correlation also depends on the spatial accuracy of the probe separation, and on the temporal coincidence of every data point, as determined by the coincidence window. Due to these additional sources of error, the relative accuracy of the two-point correlation $\overline{uv}$ was estimated at 20%. Consequently, the relative accuracy of the R_{12} measurements was estimated at 40%. This estimate is very conservative, and includes inaccuracies due to systematic errors. For each position of the fixed probe, i.e., for each contour map, precautions were taken to ensure repeatability of the correlation coefficient measurements. The isocorrelation lines—the information of real interest to us—are thus more accurate than the numerical value associated with each line.

The results are presented in figures 16, 17, 18, 19, 20 and 21 for positions of the fixed probe equal to y^+ =2, 3, 6, 9, 12, and 18, respectively. The absolute value of the correlation coefficient is plotted in the form of contour plots. The horizontal axis represents the streamwise separation and the vertical axis the distance from the wall. The y-axis is greatly magnified compared to the x-axis. Note that the position of the fixed probe is indicated on the plots by a small arrow on the y-axis, and the successive positions of the moving probe is indicated by round symbols.

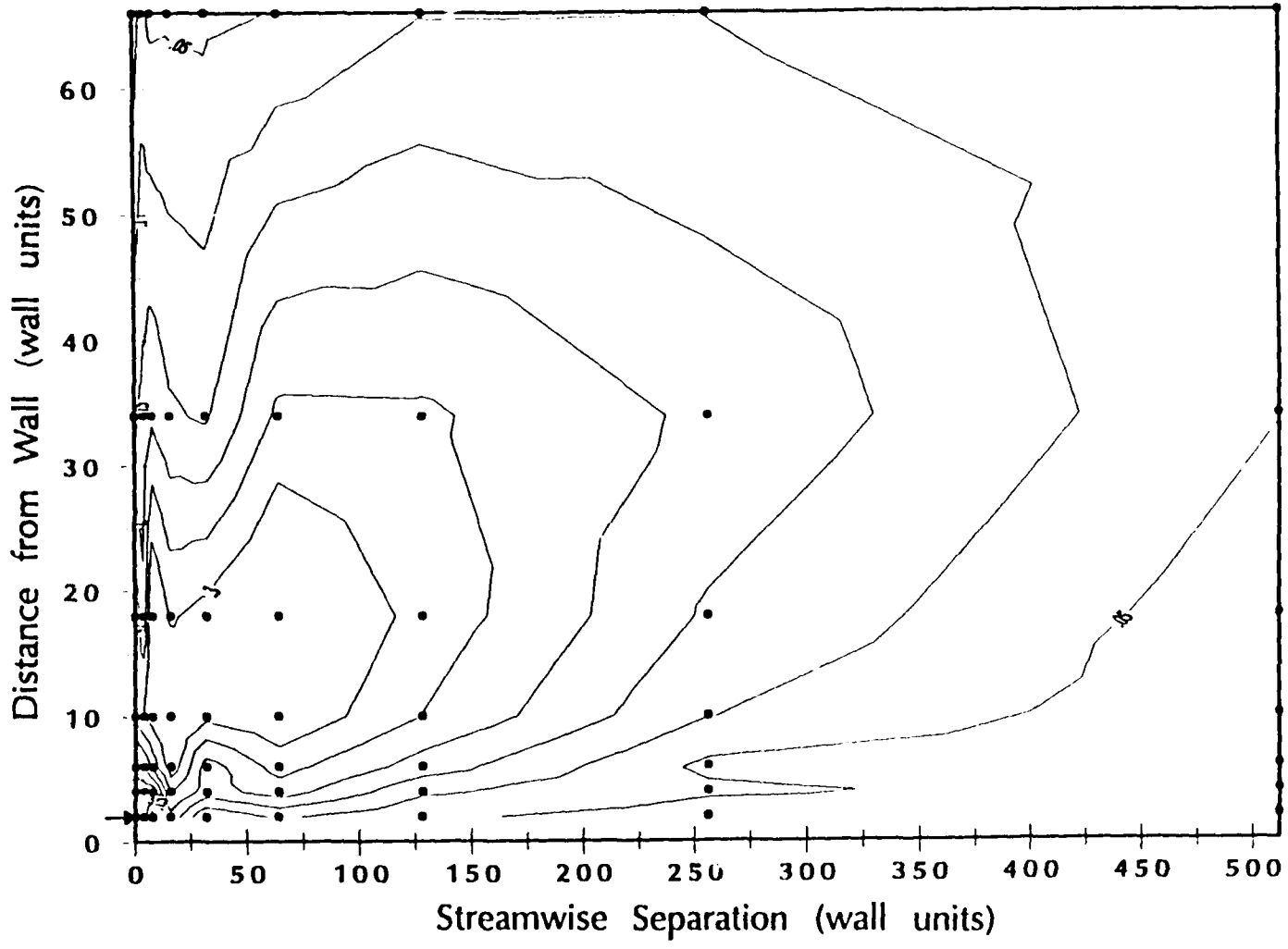

FIGURE 16
Contour Plot of $-R_{12}$ with Fixed Probe at $y^+ = 2$
Arrow Indicates Position of Fixed Probe
Dots Indicate Positions of Moving Probe

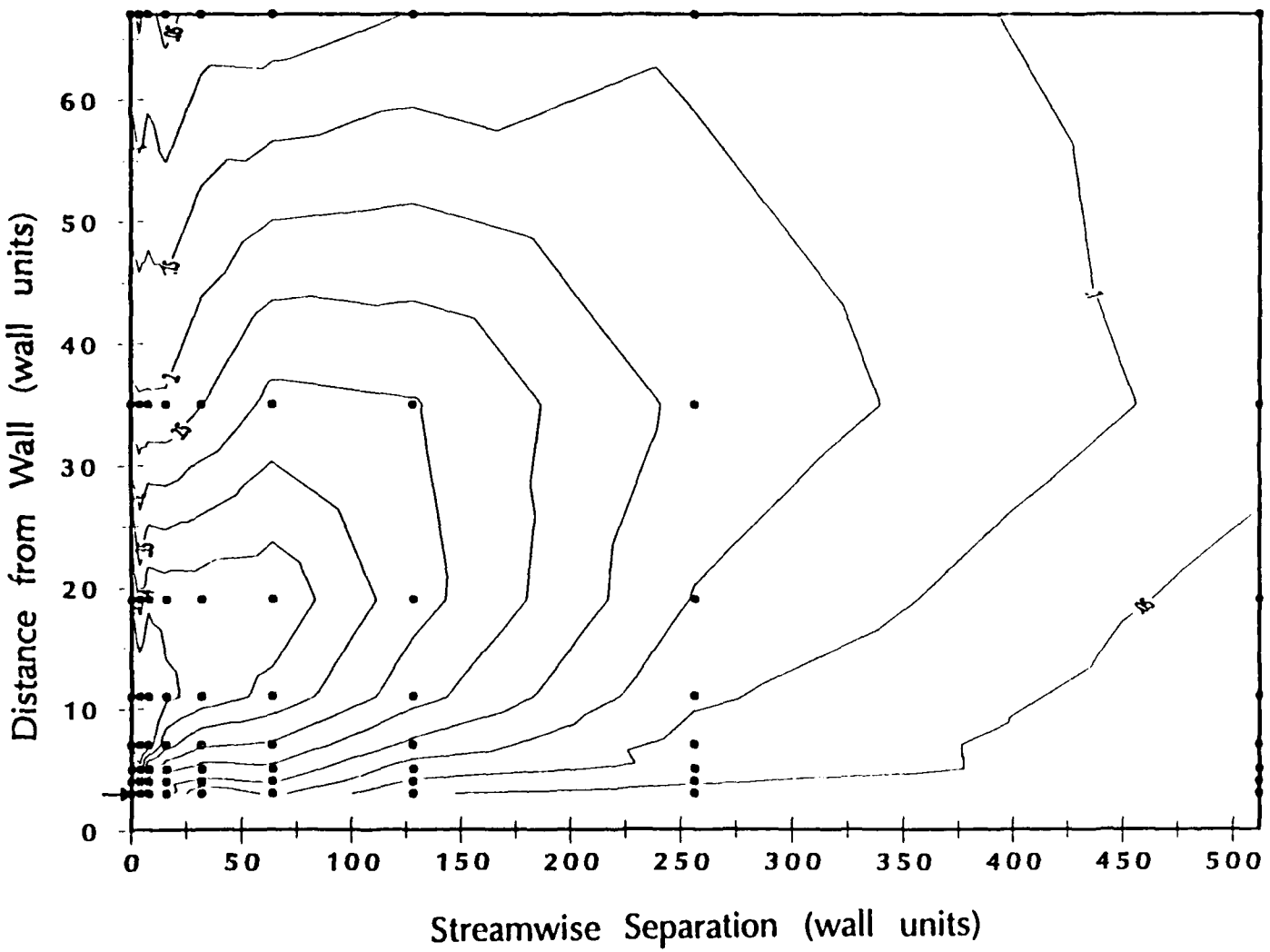

FIGURE 17
Contour Plot of $-R_{12}$ with Fixed Probe at $y^+ = 3$
Arrow Indicates Position of Fixed Probe
Dots Indicate Positions of Moving Probe

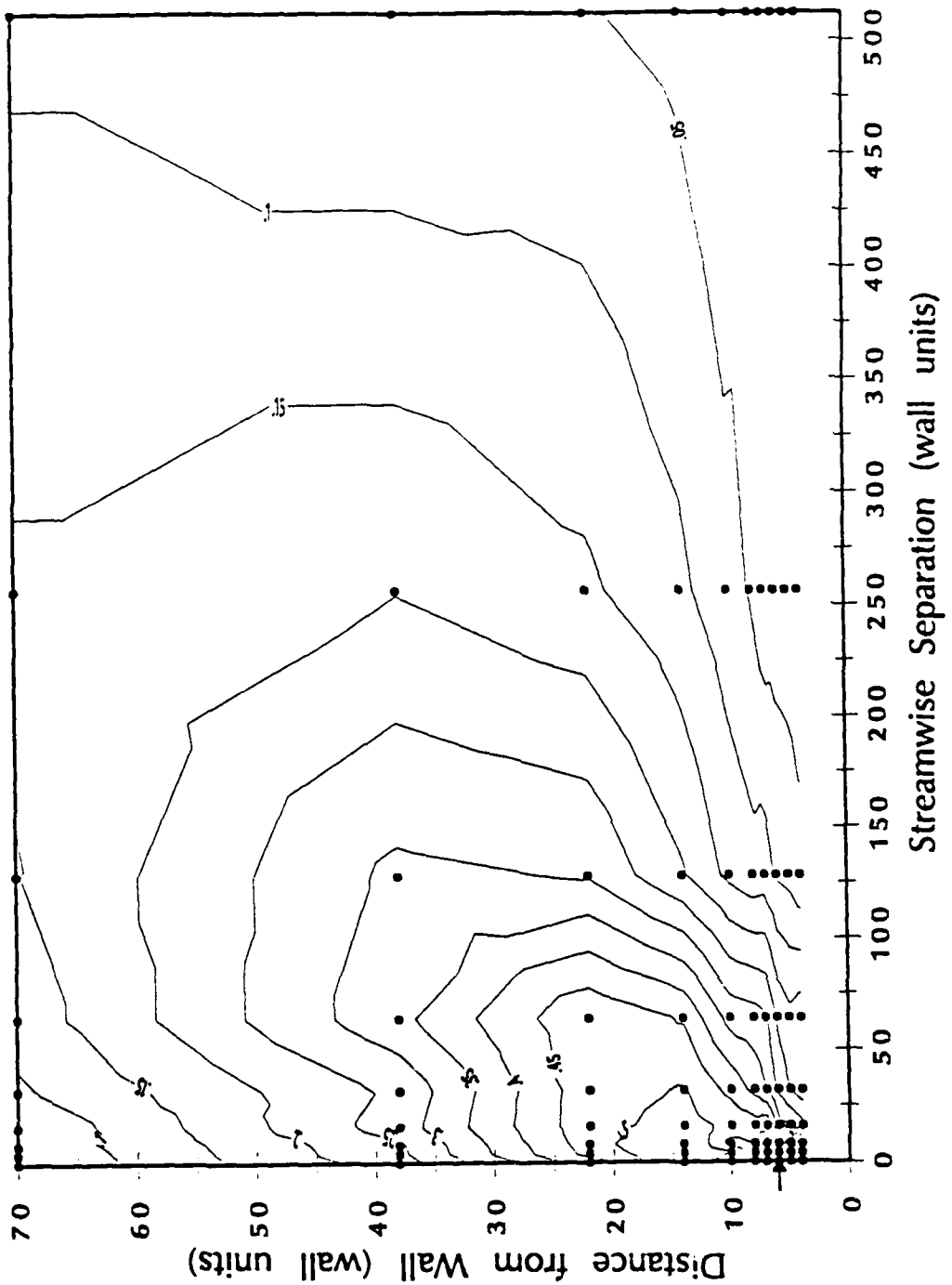

FIGURE 18
Contour Plot of $-R_{12}$ with Fixed Probe at $y^+ = 6$
Arrow Indicates Position of Fixed Probe
Dots Indicate Positions of Moving Probe

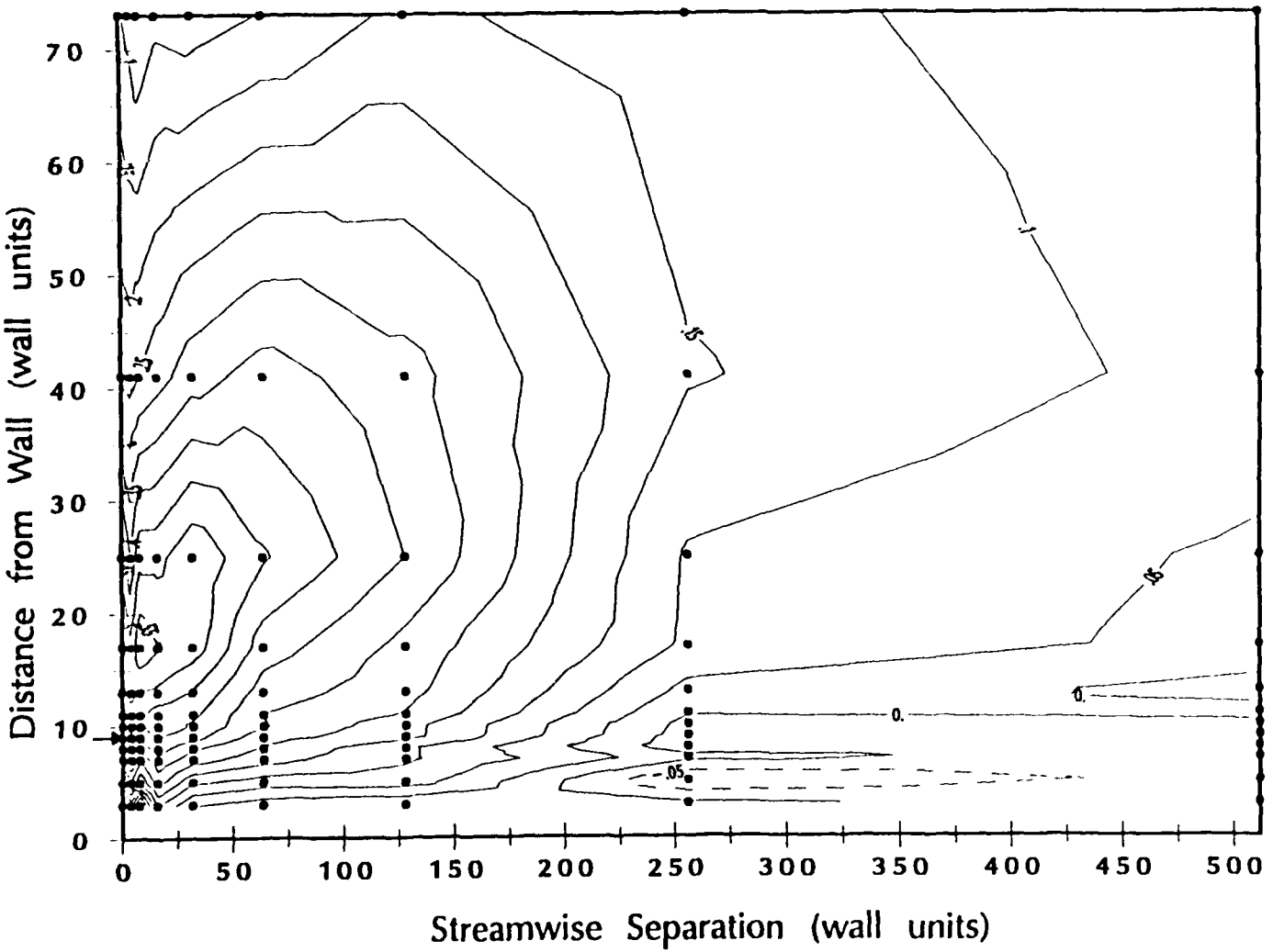

FIGURE 19
Contour Plot of $-R_{12}$ with Fixed Probe at $y^+ = 9$
Arrow Indicates Position of Fixed Probe
Dots Indicate Positions of Moving Probe

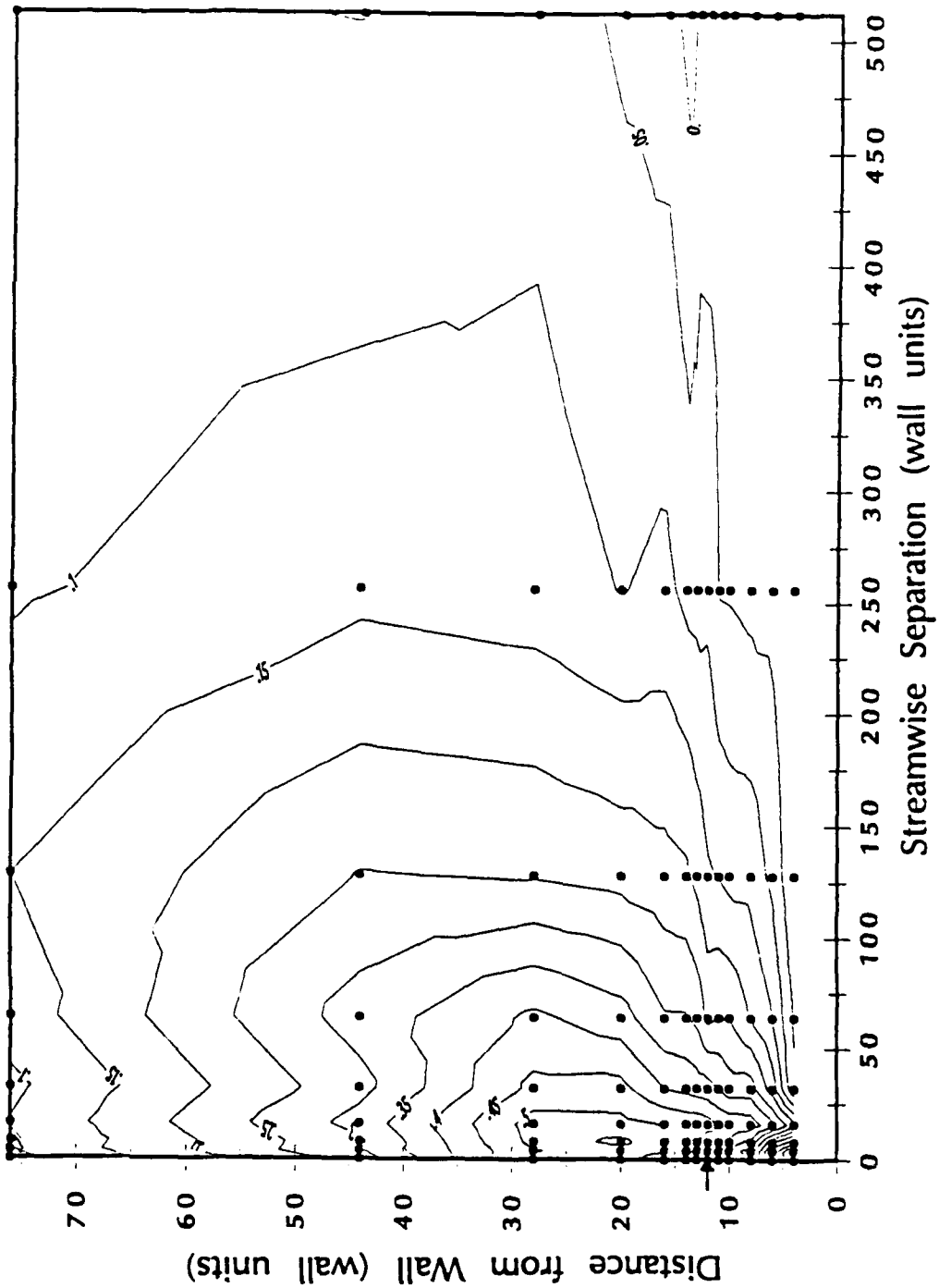

FIGURE 20
Contour Plot of $-R_{12}$ with Fixed Probe at $y^+ = 12$
Arrow Indicates Position of Fixed Probe
Dots Indicate Positions of Moving Probe

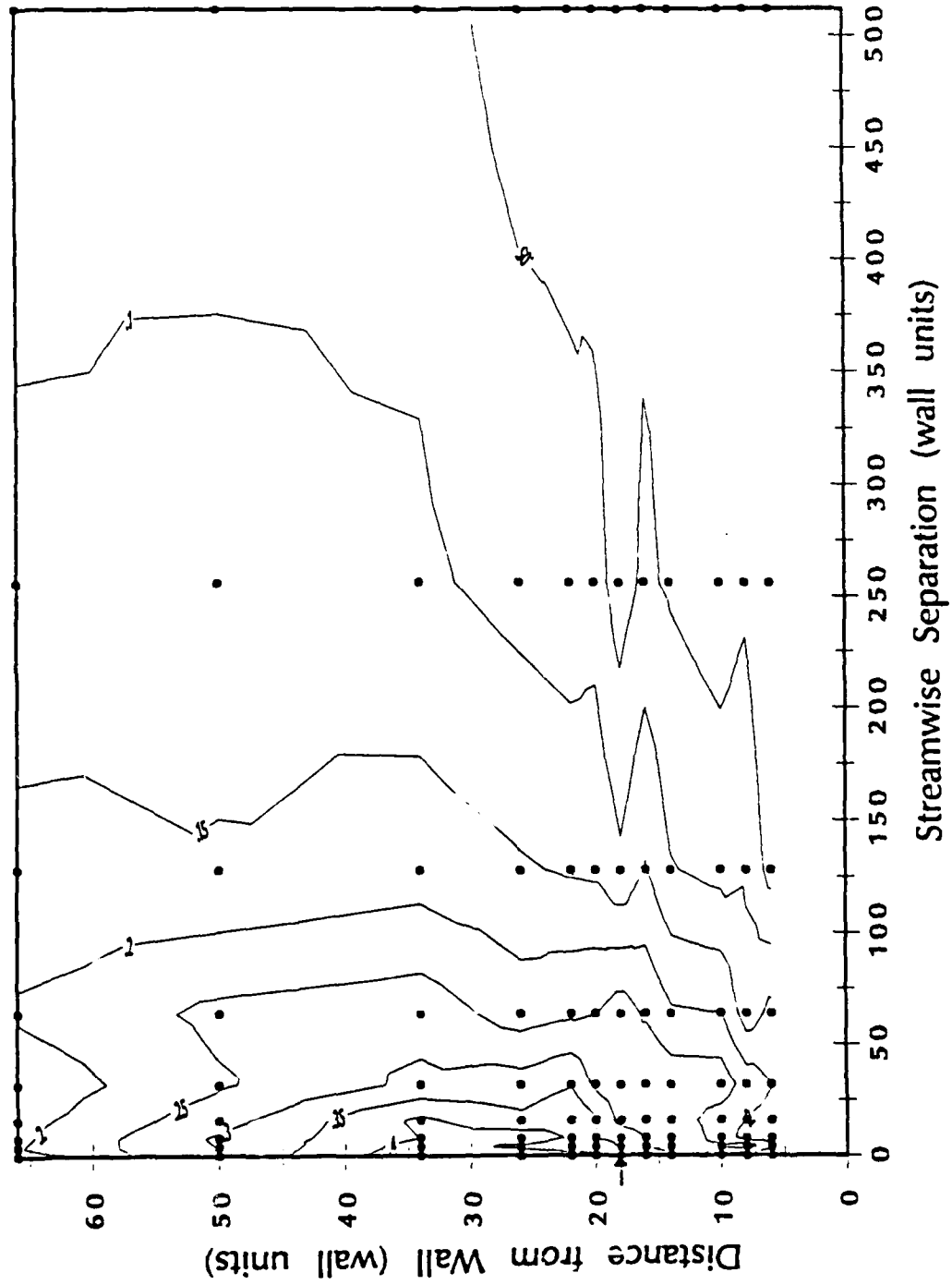

FIGURE 21
Contour Plot of $-R_{12}$ with Fixed Probe at $y^+ = 18$
Arrow Indicates Position of Fixed Probe
Dots Indicate Positions of Moving Probe

In all cases, separations larger than 500 wall units produced correlation coefficients smaller than 5%. This value is below experimental uncertainty. Since little information was added by extending the contour plots to a larger separation, the maximum separation shown on the plots is 500 wall units. The correlation coefficient was not measured for negative values of the streamwise separation. Extrapolation of the results to the left of the y-axis, seems to indicate that the correlation coefficient vanishes quickly in the region of negative streamwise separation. However, it would be useful to study this further.

The first observation concerns the scaling of the Reynolds stress eddies. As pointed out by Bradshaw (1978), the length scales of the shear-stress producing motion should be proportional to the distance from the wall. It can be observed from the contour plots, that the Reynolds stress eddies remain attached to the wall, thus satisfying the classical local scaling argument which is fundamental in the derivation of the law of the wall.

The streamwise extent of the Reynolds stress eddies seems to be smaller than that of the counter-rotating vortices described by Bakewell (1966) and Herzog (1986). These authors found that the wall vortices extend over a length of at least 1000 wall units in the streamwise direction. The size of the Reynolds stress eddies, as would be defined for example by an integral length scale, is smaller. Since the maximum correlation does not arise for zero separation, it is difficult to define a physically meaningful integral length scale; we will thus base our reasoning on the extent of the contour lines. As the fixed probe is moved away from the wall, the 25% correlation contour lines extend to smaller and smaller distances, from $\Delta y^+ = 300$ at $y^+ = 2$ to $\Delta y^+ = 150$ at $y^+ = 18$. By comparison, in the vertical direction, the size of the Reynolds stress eddies varies little, and remains of the order of 50 wall units. The consequence of these results is that

the aspect ratio of the Reynolds stress eddies changes considerably across the wall layer, from a very elongated streamwise structure in the viscous sublayer to an elliptical structure with an aspect ratio close to 3 at the bottom of the logarithmic layer.

A surprising result concerns the position of the maximum of R_{12}. In all cases, the maximum is attained at a non-zero separation distance. Previous correlation measurements, further away from the wall, did not exhibit this feature (e.g. Sabot, 1976), possibly due to the lack of resolution of the probes. Moreover, as the position of the fixed probe is changed, the length and inclination of the vector separating the location of the fixed probe from the point of maximum correlation are significantly affected. Figure 22 shows the variation of the inclination angle of this separation vector, estimated visually from the contour maps—thus possibly subject to a significant error. The angle varies almost linearly with the distance of the fixed probe from the wall. The eddies in the viscous sublayer are almost parallel to the wall, while those at the bottom of the logarithmic layer are inclined at an angle close to 56° with the wall. Physical limitations did not allow us to extend these measurements further away from the wall, but it is likely that the value of the inclination angle at $y^+ = 18$ is close to the asymptotic value reached in the outer layer. This angle is slightly larger than the value of 45° inclination angle of the hairpin vortices observed by Head and Bandyopadhyay (1981). We will come back later to this result.

Figure 23 represents the distance between the fixed probe and the point of maximum correlation as a function of the distance of the fixed probe from the wall. This distance decreases as the fixed probe is moved away from the wall, and reaches an asymptotic value equal to about 15 wall units. Note that the radial separation remains of the same order of magnitude while the

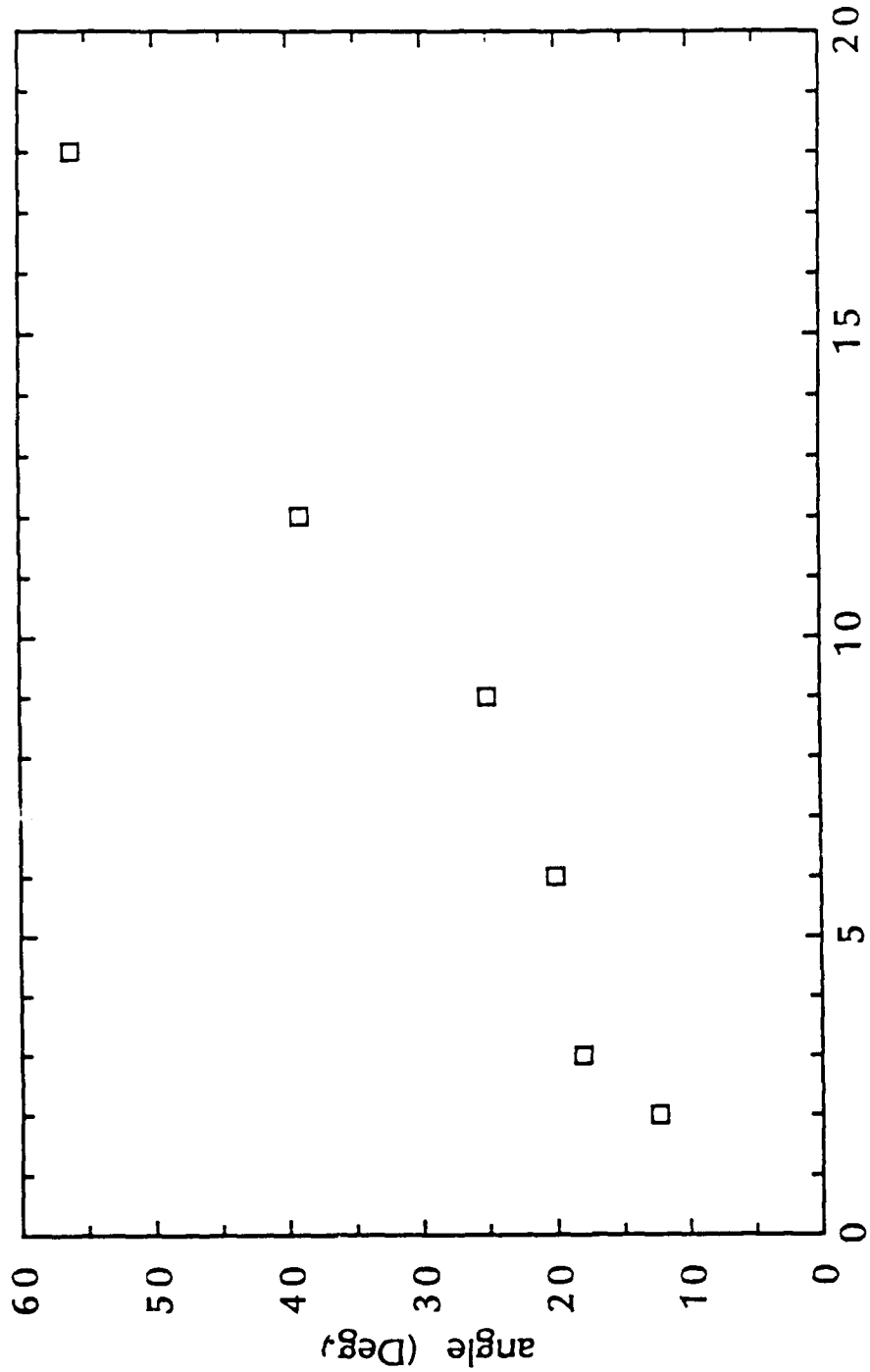

FIGURE 22
Variations of Angle of Separation Vector
between Fixed Probe and Point of Maximum Correlation
with Distance of Fixed Probe from the Wall

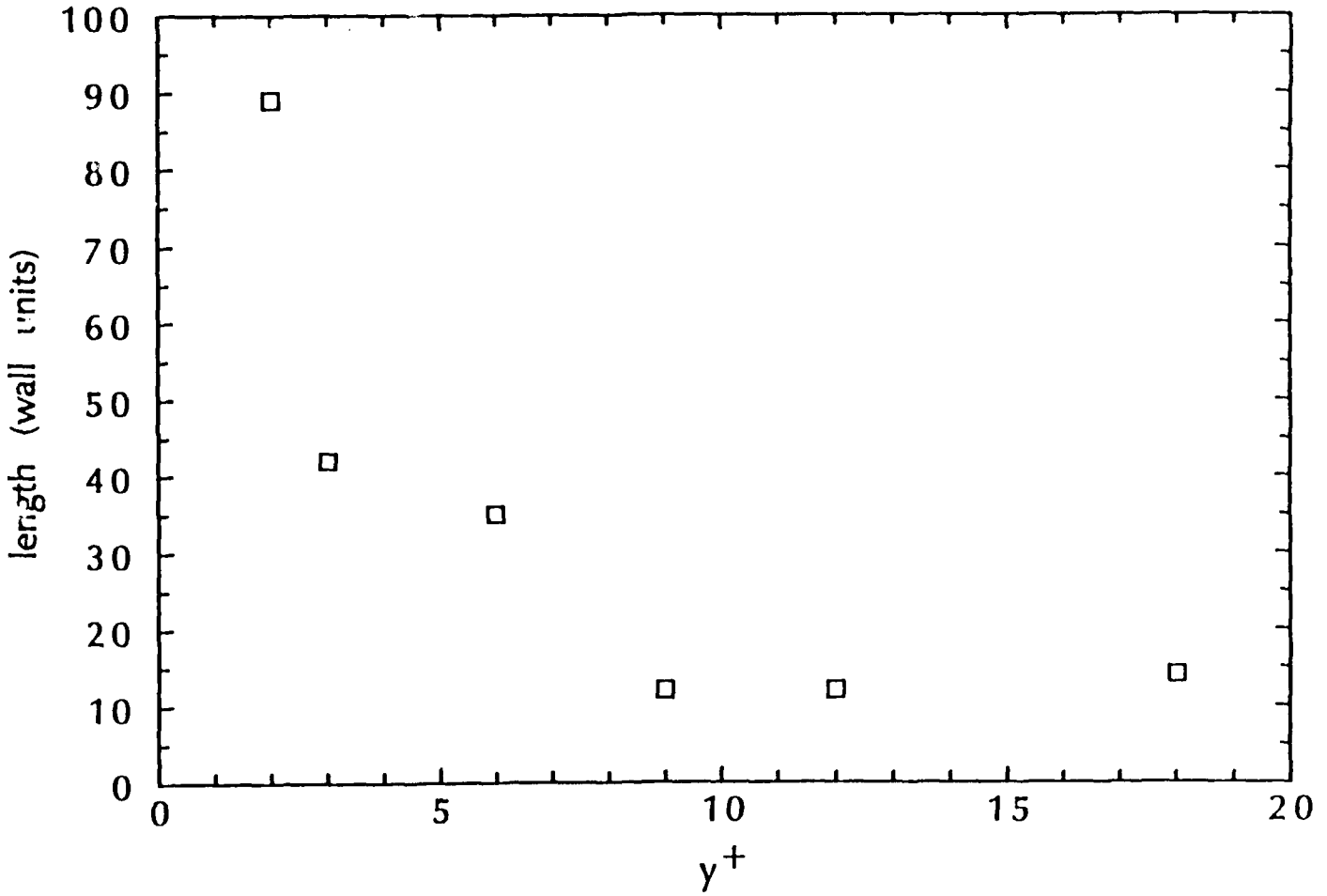

FIGURE 23
Variation of Length of Separation Vector
between Fixed Probe and Point of Maximum Correlation
with Distance of Fixed Probe from the Wall

streamwise separation becomes an order of magnitude smaller for fixed probe location between the wall and $y^+ = 9$. This might be due to the increase of the inclination angle of the Reynolds stress eddies.

The value of the correlation, although subject to a large uncertainty, is also of interest. Figure 24 represents the variation of the maximum of R_{12} with the position of the fixed probe. The distribution of R_{12} starts between 25 and 30% at the wall, increases to 55 to 60% between $y^+ = 9$ and 12, and decreases to between 35 and 40% at $y^+ = 18$. The location of the maximum, between $y^+ = 9$ and 12, also corresponds to the location of the sharpest peak: the correlation quickly decreased in this region. These results indicate that the greatest coherence is achieved for positions of the fixed probe between $y^+ = 9$ and 12.

One remark should be made concerning the contour plots of the correlation coefficient. In almost all figures, there is a horizontal spike throughout the domain at $y^+ \simeq 5$, and a vertical spike at $x^+ \simeq 25$. Nadine Aubry (private communication) noticed the same phenomenon in Herzog's results (1986). The occurrence of these spikes in the two sets of data, with totally different measuring techniques seems to exclude the possibility of an experimental error. They probably result from a peculiarity of the experimental facility.

3.4 Interpretation of the Results

First, let us emphasize that the correlation R_{12} is independent of the sign and magnitude of each individual velocity component, even though it depends on the sign and magnitude of each component relative to each other. Thus the contour lines in figures 16 to 21 simply indicate the extent of the eddies, not their strength.

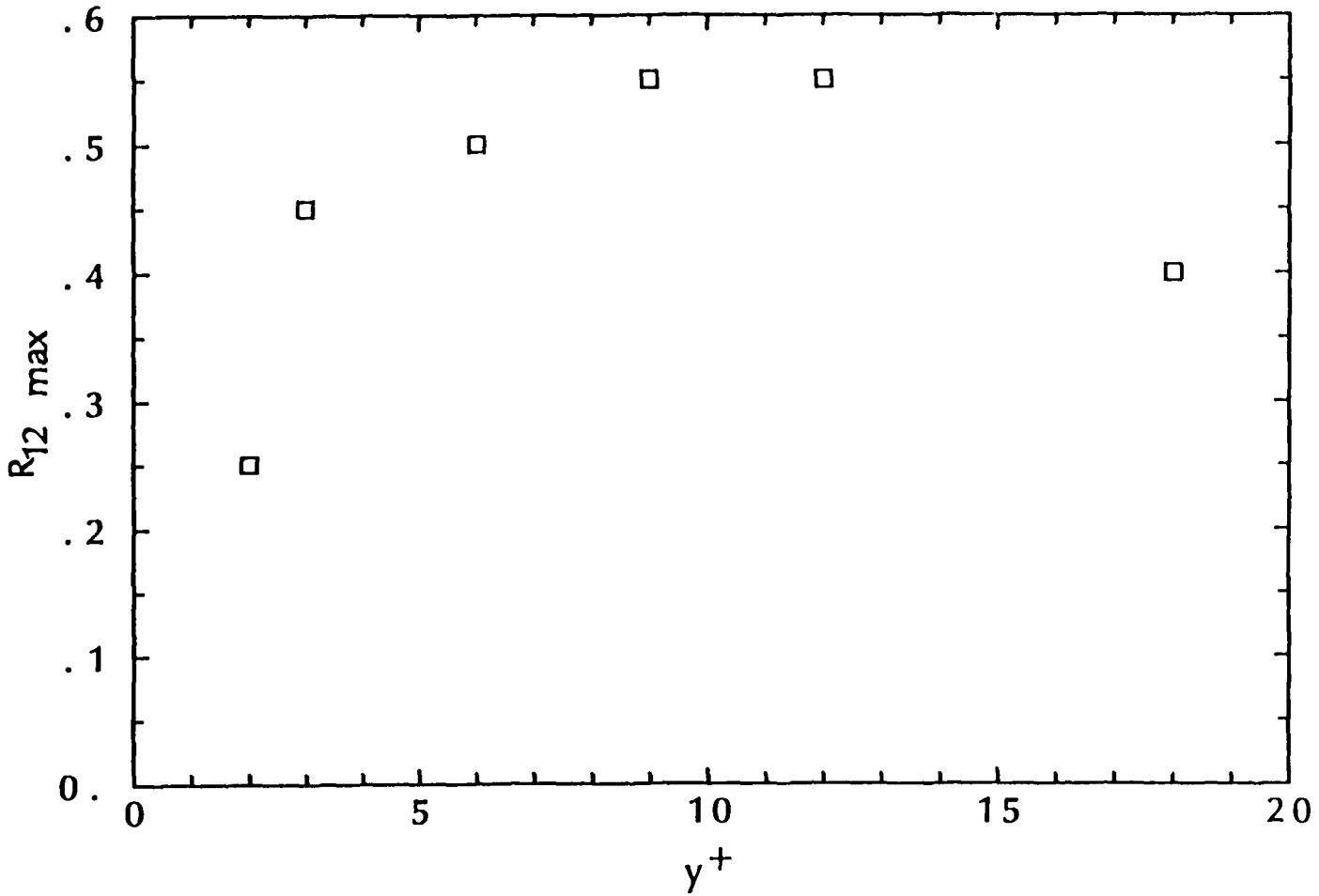

FIGURE 24
Variation of Reynolds-stress Eddies Strength
with Distance of Fixed Probe from the Wall

The continuity of figures 16 to 21 suggests that the correlation plots all represent the same structure. As we have seen, the Reynolds stress eddies are characterized by their inclination angle, which increases with their distance from the wall. The axisymmetry of the pipe implies that the average eddy is symmetric with respect to the plane of measurement. In a two-dimensional flow, the maximum value of the correlation coefficient can only occur when the two probes are at the same location. Thus the non-zero separation between the fixed probe and the point of maximum correlation observed in the present measurements can only be interpreted by a three-dimensional structure. The point of maximum correlation is the point where the radial velocity is most consistently correlated with the streamwise velocity at the fixed probe location; for example, when the streamwise velocity fluctuation at the fixed probe location is large and negative, the radial velocity at the point of maximum correlation is on the average large and positive. In contrast, the correlation coefficient for zero separation is smaller, i.e., the radial velocity follows the trend of the point of maximum correlation, but with a smaller magnitude; for example, on the average, low streamwise velocity fluid does not move away from the wall as fast as fluid located slightly downstream of it and further away from the wall. The average Reynolds stress eddy thus induces at this point a large streamwise velocity fluctuation with little effect on the radial velocity, while inducing a large radial velocity and little streamwise velocity fluctuation at a point located downstream and further away from the wall. From figure 23, we see that beyond a certain distance from the wall, the separation between these two points is approximately constant, i.e., the two points seem attached to each other. Very close to the wall, the structure is very elongated; further away from the wall, it is inclined to the wall.

An attractive interpretation of these observations involves a horseshoe or lambda vortex, with its tip located at the point of maximum correlation (figure 25). The negative streamwise velocity fluctuation is created by the uplift of low velocity fluid from between the legs of the vortex. At the same time, the interaction between the tip of the vortex and the wall moves the vortex tip away from the wall. The combination of these two simultaneous motions creates a negative correlation coefficient with the form shown on figures 16 to 21.

Let us examine this interpretation in detail. Figure 26 shows how the horseshoe vortex would contribute to the correlation coefficient. It is a sideview of a vortex, with its legs trailing in the viscous sublayer. The sense of rotation of the vortex is the same as that of the spanwise vorticity created by the wall. The action of the vortex tip is two-fold: locally, it induces a motion of rotation around itself, toward the wall downstream of it and away from the wall upstream of it; in addition, its interaction with the wall makes it move away from the wall. The action of the vortex legs is to lift low streamwise velocity fluid from between them, while at the same time pushing high velocity fluid towards the wall on the sides of the horseshoe vortex. The streamwise distance over which the vortex legs are active is much larger than that of the vortex tip.

Let us assume that the two probes are such that the fixed probe is between the legs of the vortex, at the point where the streamwise velocity defect is largest, while the moving probe is at the vortex tip. We now show that this arrangement of the probe produces a large contribution to the correlation coefficient. As the vortex tip approaches the moving probe, the fixed probe begins to sense the low streamwise velocity induced by the vortex legs. The radial velocity induced by the vortex tip starts negative, and as the vortex tip is swept by the moving probe, becomes positive and returns to zero. Since the streamwise velocity at the

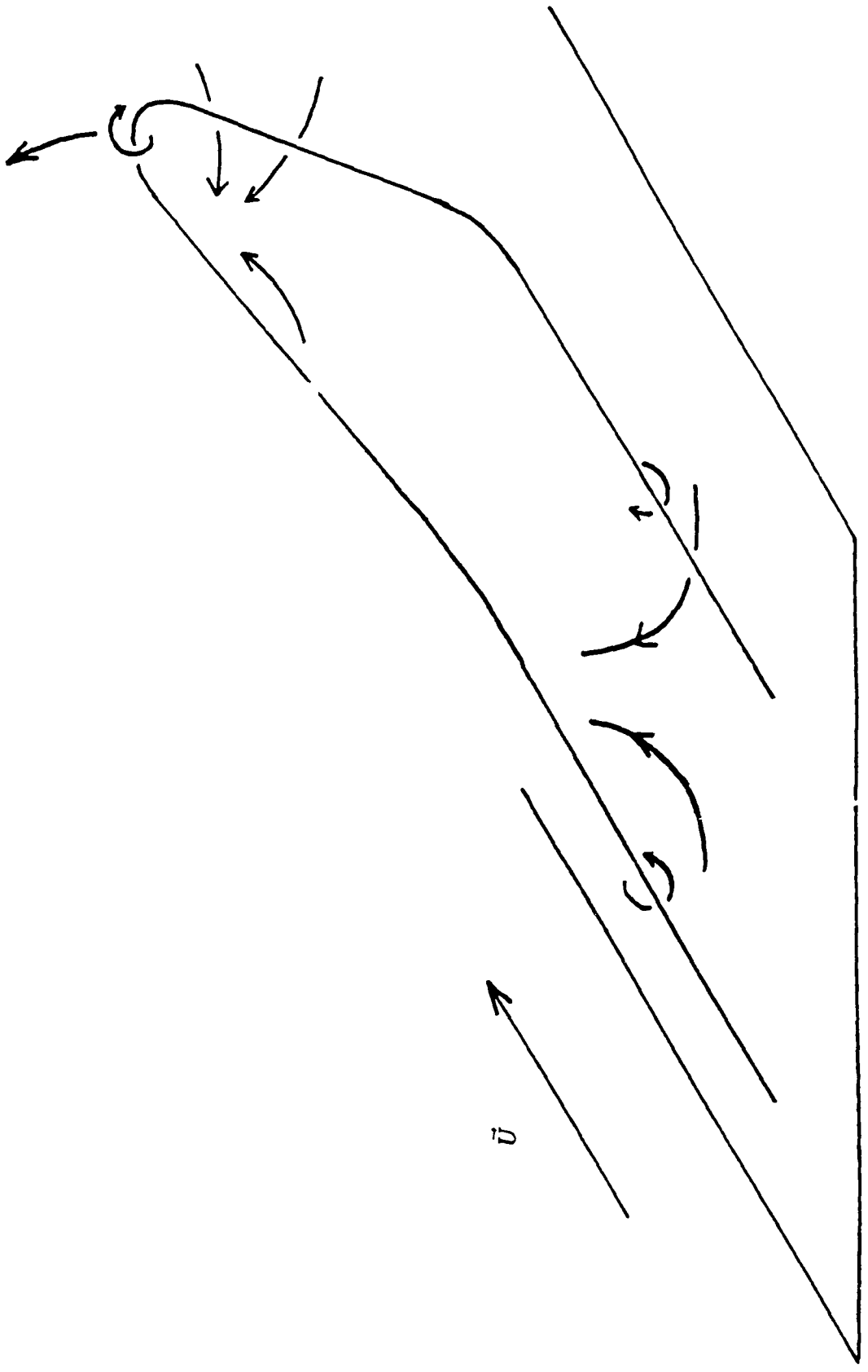

FIGURE 25
Horseshoe Vortex Pattern
and Induced Velocity Field

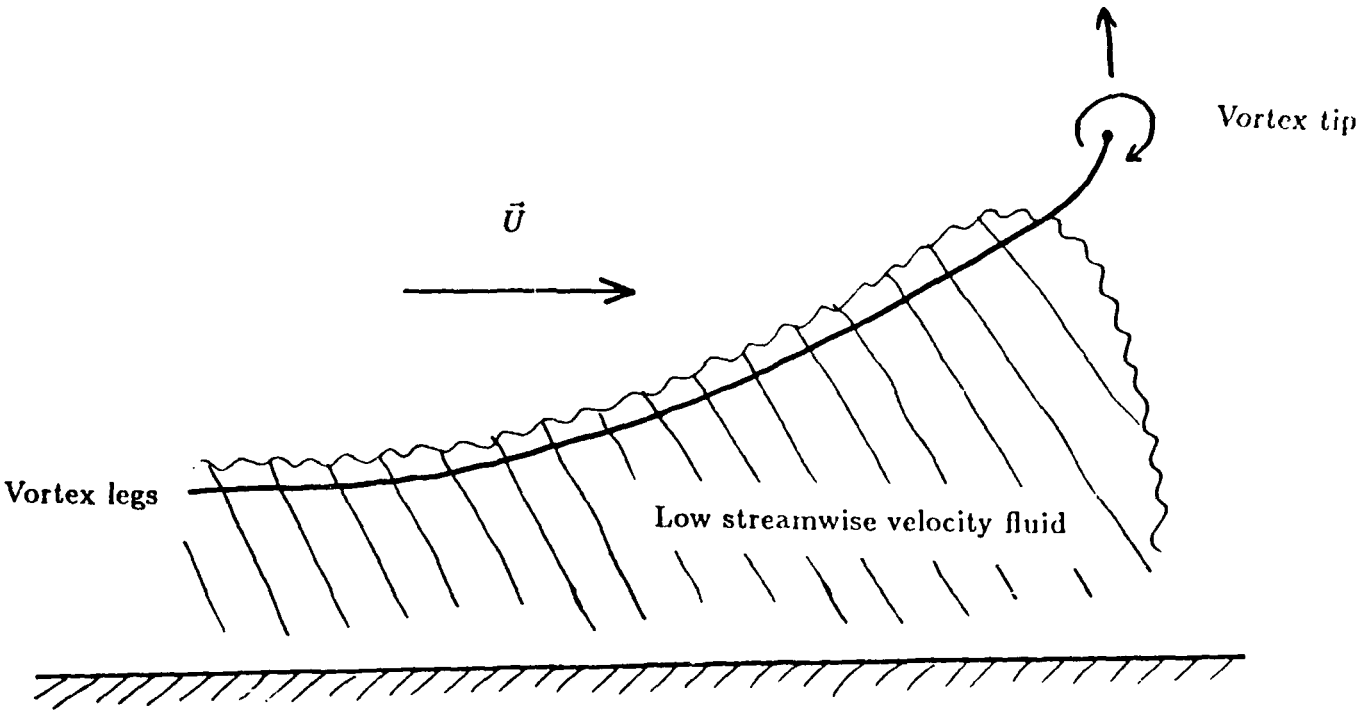

FIGURE 26
Sideview of the Horseshoe Vortex
in the Near-wall Region

fixed probe has not changed sign, the contribution to the correlation coefficient is zero. At the same time, the vortex tip experiences a radial motion away from the wall, i.e., a positive radial velocity, induced by its interaction with the wall; this motion contributes to the correlation coefficient with the correct negative sign. Thus the convection of the horseshoe vortex past the two-probe pattern creates a negative correlation globally. Other arrangement of the two probes with respect to each other will contribute less to the correlation coefficient because the radial velocity there will be smaller. Thus the maximum correlation is produced when the fixed probe is between the legs of the vortex and the moving probe at its tip.

If the probes are between two horseshoe vortices, then the fixed probe sees a positive streamwise velocity fluctuation induced by the vortices legs, while the moving probe sees a negative radial velocity imposed by the uplift of the neighboring vortex tips, and conservation of mass. Globally, the contribution to the correlation coefficient is again negative, though probably smaller than that from inside the horseshoe vortex, because not as coherent. Note that one-point studies (Lu and Wilmarth, 1973) determined that the stronger uv event is in the second quadrant, i.e. u negative and v positive. This situation corresponds to having the two probes between the legs of the vortex, and is in agreement with our interpretation.

Our results indicate that the regions of large streamwise velocity fluctuation and large radial velocity are distinct. For example, regions of low streamwise velocity are not active in the radial direction. This remark is consistent with observations of low velocity streaks by Kline et al. (1967). Note that the structures moving hydrogen bubbles into streaks are not necessarily as long as the streaks. Indeed our results seem to indicate that the structures which transport momentum from the wall are not long streamwise vortices, but spanwise vortices.

Streamwise vortices as found by Bakewell (1067) and Herzog (1986) are present— they are the legs of the horseshoe vortices— but they are much weaker than the tip vortices.

The motion of the horseshoe vortices away from the wall explains why the inclination angle shown on figure 22 increases as the distance of the fixed probe from the wall increases. The fact that the inclination angle reaches values larger than 45° is somewhat surprising, because Head and Bandyopadhyay (1981) unambiguously showed that the preferred inclination angle of the horseshoe vortices is 45°. However, their picture of the horseshoe vortices clearly shows that the vortex tip is bent in the upstream direction. This would correspond in our measurement to an angle larger than 45°.

The connection between our interpretation and the bursting phenomenon is difficult to clarify, but several points are worth mentioning. As pointed out by Kline et al. (1967), if bursts result from an inflexional instability, this instability must occur in the buffer layer, not in the viscous sublayer. This is confirmed by our measurements, because the correlation coefficient remains small in the viscous sublayer. The largest correlation coefficient (figure 24) occurs when the tip of the vortex is around $y^+ = 20$; this is where bursting has been observed in visual and hot-wire investigations. Because the random motion observed during bursting does not contribute to the correlation coefficient, the burst does not appear in the contour plots as a separate entity. Conditional averaging techniques would be necessary to further investigate the spatial structure of the bursts and their connection to the present data.

The interpretation of the correlation results is in good agreement with flow visualization results of Kline et al. (1967) in the wall region, and Head and

Bandyopadhyay (1981) in the outer layer. The former authors suggested that the streamwise vortices could be the legs of the horseshoe vortices they had observed in the outer layer. The present results support this idea, but emphasize the importance of the vortex tip in the buffer layer.

Chapter 4

A MODEL OF THE FLOW IN THE VISCOUS SUBLAYER

4.1 Introduction

The goal of this chapter is to present a simple model of the flow in the viscous sublayer. Most existing models (Einstein and Li, 1956; Hanratty, 1956; Sternberg, 1962) do not incorporate the existence of the low speed streaks. The study by Hatziavramidis and Hanratty (1978) used visual observations of the flow in the viscous sublayer to simplify the equations and choose physically plausible boundary conditions. They obtained a set of equations which was solved numerically. Their results were in good qualitative agreement with experimental results. Detailed simulations of the flow in the wall region were recently performed by Chapman and Kuhn (1986) and Azab and McLaughlin (1987).

Our goal in devising the model presented in this chapter was to study the behavior of the correlation coefficient close to the wall. The major difficulty is trying to connect a totally deterministic model with statistical experimental results. The approach we have followed is simple-minded, but the results it provides are surprisingly good. We have been able to predict with satisfactory accuracy the distribution of the mean velocity and turbulent intensity up to $y^+ = 25$ with very little empirical input. The only constants required are the spanwise period of the counter-rotating vortices, the height of their centers, and the RMS-value of the radial velocity at this height.

This model tries to reproduce the qualitative picture of the flow in the near-wall region as can be drawn, for example, from the flow visualization of Kline et al. (1967). The present experimental results have been used in determining the boundary condition. The model assumes a weak coupling between the flow in the streamwise direction and the flow in the cross-plane direction.The flow in the cross-plane direction is assumed to be purely two dimensional, and is represented by a pair of counter-rotating streamwise vortices. This assumption is based on the findings of Bakewell (1966) and Herzog (1986). They determined that the first eigenmode of Lumley's proper orthogonal decomposition consists of a pair of counter-rotating vortices with a length much greater than their cross-stream dimensions. The vortices are assumed to be steady, which means that we neglect their interaction with each other and with the wall. The calculation uses a low Reynolds number approximation. The form of the boundary condition provides an exact analytical solution to this problem. The velocities thus computed in the cross-plane are substituted into a simplified form of the streamwise momentum equation. The resulting linear partial differential equation is solved numerically for the streamwise velocity. The velocity statistics are computed by assuming that the counter-rotating vortices fill the wall region and occur at random locations in the spanwise direction.

4.2 Calculation of the Flow in the Cross-plane

We assume that the counter-rotating vortices fit into a rectangular box of width W and height H. Inertial forces in this box are assumed much smaller than viscous forces and are thus neglected. This approximation may be questionable, because the local Reynolds number varies like y^{+2} in the viscous sublayer. However, our goal is only to obtain a velocity field that satisfies the boundary

conditions and the continuity equation. By doing so, we neglect the dynamics, but the kinematic constraints are satisfied. Even though the cross-plane flow in the buffer layer is probably poorly modeled, this approach provides satisfactory results in the viscous sublayer.

Let the streamfunction $\Psi(z,y)$ be defined by:

$$w = -\Psi_y \text{ and } v = \Psi_z$$

We look for a solution of the following Stokes problem:

$$\Delta^2 \Psi = 0 \tag{4.1}$$

between $z = 0$ and W, and $y = 0$ and H, with the following boundary conditions:

- no-slip condition at the wall: $\Psi = \Psi_y = 0$ at $y = 0$
- symmetry condition on the sides of the domain: $\Psi = \Psi_{zz} = 0$ at $z = 0$ and $z = W$
- no spanwise velocity: $\Psi_y = 0$, and a sinusoidal normal velocity:

$$\Psi_z = -V_e \cos\left(\frac{\pi z}{W}\right)$$

at $y = H$, where V_e is the maximum amplitude of the normal velocity on top of the domain.

Equation 4.1 is linear, and can be solved by expanding the solution in the following form:

$$\Psi(z,y) = -V_e \sum_{m=0}^{\infty} f_m(y) \sin\left(\frac{m\pi z}{W}\right)$$

The boundary condition at $y = H$ restricts the sum to the term $m = 1$ only, so that:

$$\Psi(z,y) = -V_e f(y) \sin\left(\frac{\pi z}{W}\right)$$

Substitution of this expression into equation 4.1 gives the following equation for f:

$$\left(\frac{\pi}{H}\right)^4 f - 2\left(\frac{\pi}{H}\right)^2 f'' + f^{(iv)} = 0$$

We look for a solution to this equation of the form:

$$f = \sum_{i=1}^{4} f_i e^{\lambda_i y}$$

where λ_i is one of the roots of the equation:

$$\left(\lambda_i^2 - \left(\frac{\pi}{H}\right)^2\right)^2 = 0$$

There are two double-roots:

$$\lambda_i = \pm\frac{\pi}{H}$$

The constants f_i are determined by applying the boundary conditions. To simplify the algebra, the function f is expressed in terms of the hyperbolic sine and cosine functions:

$$f(y) = AW\,sinh\left(\pi\frac{y}{H}\right) + BW\,cosh\left(\pi\frac{y}{H}\right) + C\,y\,sinh\left(\pi\frac{y}{H}\right) + D\,y\,cosh\left(\pi\frac{y}{H}\right)$$

Application of the boundary conditions at $y = 0$ yields $B = 0$ and:

$$D = -\pi A\left(\frac{W}{H}\right)$$

and at $y = H$:

$$C = A\frac{\pi^2\,sinh\pi}{sinh\pi + \pi cosh\pi}\left(\frac{W}{H}\right)$$

and:

$$A = \frac{1}{\pi}\frac{sinh\pi + \pi\,cosh\pi}{sinh^2\pi - \pi^2} \simeq 0.1236$$

Finally $\Psi(z,y)$ can be expressed as:

$$\Psi(z,y) = A\left[\left(\pi\frac{y}{H}\right)cosh\left(\pi\frac{y}{H}\right) - \left(E\left(\frac{y}{H}\right)+1\right)sinh\left(\pi\frac{y}{H}\right)\right] W\, V_e\, sin\left(\pi\frac{z}{W}\right) \tag{4.2}$$

where:

$$E = \frac{\pi^2\, sinh\pi}{sinh\pi + \pi cosh\pi} \simeq 2.3763$$

Figure 27 shows the streamlines corresponding to this solution. W was chosen equal to 80 wall units and H to 30 wall units, as found experimentally by Bakewell (1966). The streamline pattern is similar to that of Bakewell.

Let us assume that the counter-rotating vortices occur at random positions in the spanwise direction (Kline et al., 1967), and that they fill the wall region so that each vortex pair stands immediately next to another. Then the statistics of v and w obtained by long term averaging, and those obtained by averaging in the spanwise direction are equivalent. Bakewell (1967) and Herzog (1986) found that approximately 80% of the turbulent kinetic energy is contained in the the first eigenmode of the proper orthogonal decomposition. Since we neglect higher-order modes in this model, the statistics computed with the present model should provide somewhat low values of the second-order moments of v and w.

The velocities v and w are readily computed from equation 4.2 and the definition of the streamfunction:

$$w(z,y) = A\frac{W}{H}\left[\left(E - \pi^2\frac{y}{H}\right) nh\left(\pi\frac{y}{H}\right) + E\pi\frac{y}{H}cosh\left(\pi\frac{y}{H}\right)\right] V_e\, sin\left(\pi\frac{z}{W}\right) \tag{4.3}$$

$$v(z,y) = A\pi\left[\pi\frac{y}{H}cosh\left(\pi\frac{y}{H}\right) - \left(E\frac{y}{H}+1\right)sinh\left(\pi\frac{y}{H}\right)\right] V_e\, cos\left(\pi\frac{z}{W}\right) \tag{4.4}$$

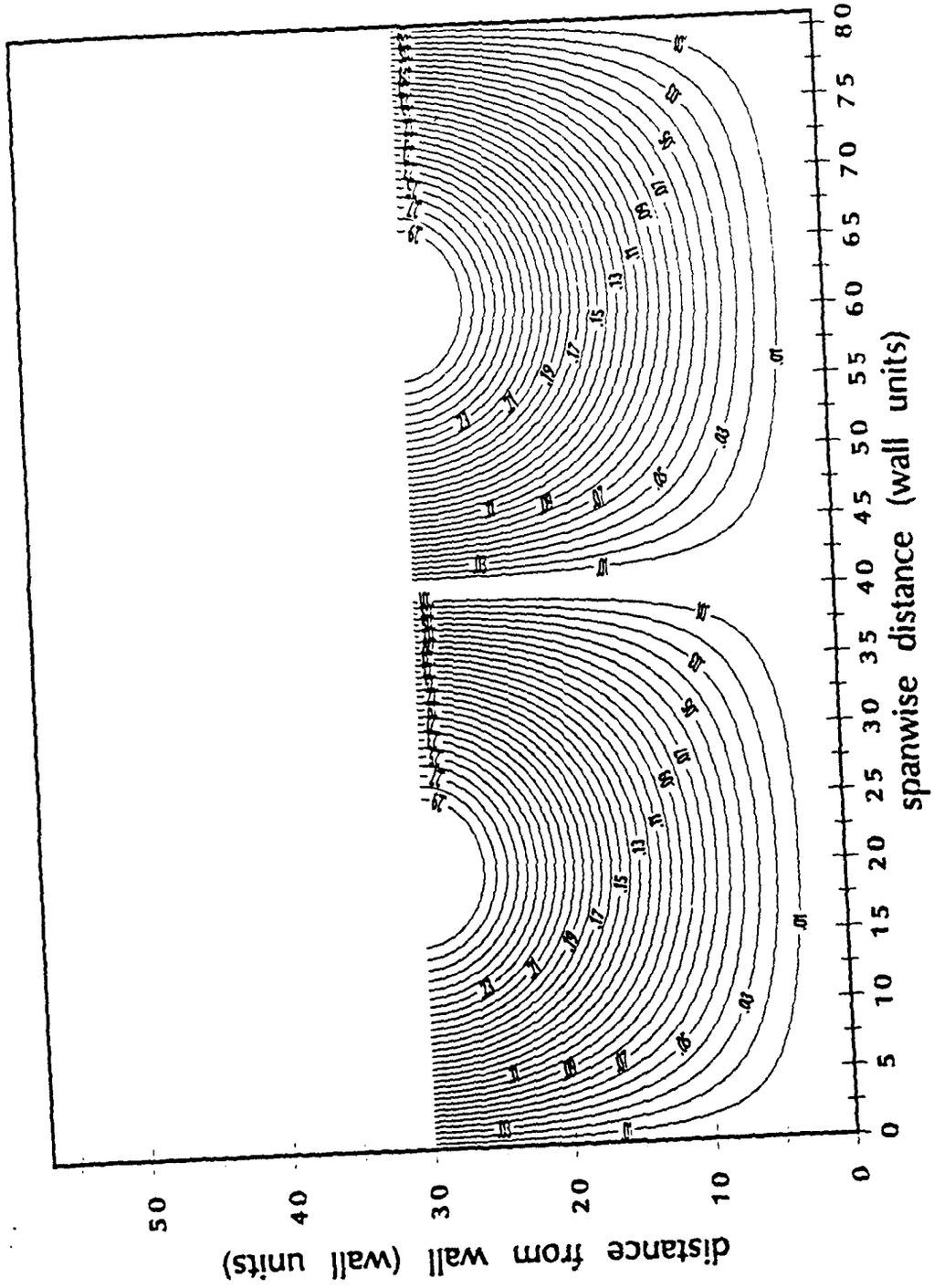

FIGURE 27
Streamlines of the Flow
in the Cross-Plane $z - y$

The quantities of primary interest are the standard deviations of v and w, as a function of y. Squaring the expressions for $v(z,y)$ and $w(z,y)$, and averaging over a wavelength W in the spanwise direction yields:

$$\frac{w'(y)}{v'(H)} = A\left(\frac{W}{H}\right)\left[\left(E - \pi^2\frac{y}{H}\right)sinh\left(\pi\frac{y}{H}\right) + E\pi\frac{y}{H}cosh\left(\pi\frac{y}{H}\right)\right]$$

$$\frac{v'(y)}{v'(H)} = A\pi\left[\left(E\frac{y}{H}+1\right)sinh\left(\pi\frac{y}{H}\right) - \pi\frac{y}{H}cosh\left(\pi\frac{y}{H}\right)\right]$$

where the prime superscript stands for the RMS value of the velocity component.

For $H = 30$, the experimental value of $v'(H)/u_\tau$ is close to 0.875 (figure 12). This allows us to plot the expressions for $w'(y)$ and $v'(y)$ on figure 11 and 12 for comparison with experimental results. Considering the crudeness of the model, the comparison is very good.

The agreement of the calculated value of the spanwise velocity with experimental data is excellent up to $y^+ = 25$. Beyond this distance, the boundary conditions on top of the domain causes it to cancel at $y^+ = H$. This boundary condition was chosen ad hoc, to give us the desired counter-rotating vortices. Obviously, it is not physical. In fact, an attempt to use a different boundary condition, apparently more physical (zero derivative for the spanwise velocity), significantly deteriorated the results. Several reasons can be put forward:

- The Stokes approximation does not hold this far from the wall. Any attempt to correctly model this part of the flow must incorporate convective effects.

- The top boundary condition is the only coupling between the flow in the near wall region and that in the outer flow. The latter is much more complicated that can be represented analytically. The large scale motion of the outer part of the boundary layer acts in a complicated way on the counter-rotating

vortices. This model assumes that this motion, however, does not have a direct effect on the motion in the near-wall region.

In the outer region, the influence of the wall weakens considerably, thus largely reducing the anisotropy present in the near wall region. The fluctuating velocity components caused by the large scale motion are therefore statistically very similar in this region. These observations could provide a basis for a matching between the near-wall region and the outer region.

We now study the behavior of v' and w' as y goes to zero. Developing the hyperbolic sine and cosine in Taylor series around zero, we find:

$$\frac{w'(y)}{v'(H)} = 2AE\pi \left(\frac{W}{H}\right) \left[\left(\frac{y}{H}\right) + \frac{\pi^2}{2}\left(1 - \frac{1}{E}\right)\left(\frac{y}{H}\right) + O\left(\frac{y}{H}\right)^3\right]$$

$$\frac{v'(y)}{v'(H)} = AE\pi^2 \left[\left(\frac{y}{H}\right)^2 - \frac{\pi^2}{2}\left(\frac{y}{H}\right)^3 + O\left(\frac{y}{H}\right)^4\right]$$

Therefore this model provides results in agreement with reasoning based on physical arguments: the spanwise velocity component varies linearly with the distance from the wall, whereas the normal velocity component varies as its square. We now non-dimensionalize these expressions with the friction velocity to get:

$$w^+ \simeq 2AE\pi \left(\frac{v'(H)}{u_\tau}\right)\left(\frac{W}{H}\right)\left(\frac{\eta}{H}\right) y^+$$

$$v^+ \simeq AE\pi^2 \left(\frac{v'(H)}{u_\tau}\right)\left(\frac{\eta}{H}\right)^2 y^{+2}$$

where η represents one wall unit.

For H equal to 30 wall units, we find the following expressions:

$$w^+ \simeq 1.435\,10^{-1}\, y^+$$

$$v^+ \simeq 2.82\,10^{-3}\, y^{+2}$$

These expressions provide numerical formulas for the asymptotic behavior of the spanwise and normal RMS velocities.

4.3 Streamwise Velocity Pattern

The momentum equation in the streamwise direction can be written:

$$\frac{\partial u}{\partial t} + u\frac{\partial u}{\partial x} + v\frac{\partial u}{\partial y} + w\frac{\partial u}{\partial z} = -\frac{1}{\rho}\frac{\partial p}{\partial x} + \nu\left(\frac{\partial^2 u}{\partial x^2} + \frac{\partial^2 u}{\partial y^2} + \frac{\partial^2 u}{\partial x^2}\right) \qquad (4.5)$$

To non-dimensionalize this equation, we use the mean velocity U_e at the top edge of the domain, the height H of the domain, and the kinematic viscosity ν. Equation 4.5 may then be rewritten in non-dimensional form:

$$\frac{\partial u}{\partial t} + u\frac{\partial u}{\partial x} + v\frac{\partial u}{\partial y} + w\frac{\partial u}{\partial z} = -\frac{\partial p}{\partial x} + \frac{1}{R_e}\left(\frac{\partial^2 u}{\partial x^2} + \frac{\partial^2 u}{\partial y^2} + \frac{\partial^2 u}{\partial x^2}\right)$$

where the quantities u,v and w now represent the non-dimensionalized velocity components.

Experimental results (e.g Kline et al., 1967) show that the streamwise extent of the structures in the viscous sublayer is much larger than their dimensions in the cross-plane. Therefore we assume that:

$$\frac{\partial}{\partial x} << \frac{\partial}{\partial y} \text{ and } \frac{\partial}{\partial z}$$

We also know that the three components of velocity u, v and w are of the same order of magnitude at the top boundary. We thus neglect the convection of streamwise momentum in the streamwise direction:

$$u\frac{\partial u}{\partial x} << v\frac{\partial u}{\partial y} \text{ and } w\frac{\partial u}{\partial z}$$

The persistence of the streaks observed experimentally also allows us to assume that the temporal changes caused by the convection of streamwise velocity by

the crosswise velocity components v and w are much slower than those resulting from the instability leading to bursting. Therefore we use the stationary values of v and w calculated in the previous section (equations 4.3 and 4.4). With these approximations, equation 4.5 becomes:

$$\frac{\partial u(y,z,t)}{\partial t} = -v(y,z)\frac{\partial u(y,z,t)}{\partial y} - w(y,z)\frac{\partial u(y,z,t)}{\partial z}$$

$$+\frac{1}{R_e}\left(\frac{\partial^2 u(y,z,t)}{\partial y^2} + \frac{\partial^2 u(y,z,t)}{\partial z^2}\right)$$

The term $\partial u/\partial t$ is kept for numerical reasons only. This equation is linear. Its right-hand side possesses an integrating factor which allows us to simplify it further:

$$R_e\frac{\partial u}{\partial t} = e^{\left(R_e \int v\,dy\right)}\frac{\partial}{\partial y}\left[e^{\left(-R_e \int v\,dy\right)}\frac{\partial u}{\partial y}\right] + e^{\left(R_e \int w\,dz\right)}\frac{\partial}{\partial z}\left[e^{\left(-R_e \int w\,dz\right)}\frac{\partial u}{\partial z}\right]$$

The value of the integrals:

$$I = \int v\,dy \quad \text{and} \quad J = \int w\,dz$$

can be calculated exactly from equations 4.3 and 4.4:

$$I = A\left[\left(-2 - E\frac{y}{H}\right)cosh\left(\pi\frac{y}{H}\right) + \left(\pi\frac{y}{H} + \frac{E}{\pi}\right)sinh\left(\pi\frac{y}{H}\right)\right]H\,V_e\,cos\left(\pi\frac{z}{W}\right)$$

$$J = -\frac{A}{\pi}\left[\left(E - \pi^2\frac{y}{H}\right)sinh\left(\pi\frac{y}{H}\right) + \pi E\frac{y}{H}cosh\left(\pi\frac{y}{H}\right)\right]\frac{W}{H}W\,V_e\,cos\left(\pi\frac{z}{W}\right)$$

Let:

$$\alpha = e^{-R_e I} \text{ and } \beta = e^{-R_e J}$$

The streamwise momentum equation simply becomes:

$$u_t = \frac{1}{R_e}\left[\frac{1}{\alpha}\frac{\partial(\alpha\,u_y)}{\partial y} + \frac{1}{\beta}\frac{\partial(\beta\,u_z)}{\partial z}\right] \tag{4.6}$$

which is a variable coefficient form of the two-dimensional heat equation.

Equation 4.6 is solved numerically using an explicit scheme first order accurate in time. The spatial derivatives are estimated using central differencing. The form of α and β allows additional simplifications, after discretization:

$$\frac{1}{\alpha}\frac{\partial(\alpha u_y)}{\partial y} = \frac{\alpha_{i,j+1/2}}{\alpha_{i,j}}\left(\frac{u_{i,j+1}-u_{i,j}}{\Delta y^2}\right) - \frac{\alpha_{i,j-1/2}}{\alpha_{i,j}}\left(\frac{u_{i,j}-u_{i,j-1}}{\Delta y^2}\right)$$

From the definition of α, we have:

$$\frac{\alpha_{i,j+1/2}}{\alpha_{i,j}} = e^{-R_e\int_y^{y+\Delta y/2} v\,dy}$$

In the present calculation, this quantity can be computed exactly. In general, this integral could be approximated by the value of the velocity at $(y-\Delta y/4)$. Similar expressions can be derived for the remaining coefficients of equation 4.6. For simplicity, we define:

$$\alpha_1 = \frac{e^{-R_e\int_y^{y+\Delta y/2} v\,dy}}{R_e\,\Delta y^2} \text{ and } \alpha_2 = \frac{e^{-R_e\int_y^{y-\Delta y/2} v\,dy}}{R_e\,\Delta y^2}$$

$$\beta_1 = \frac{e^{-R_e\int_z^{z+\Delta z/2} w\,dz}}{R_e\,\Delta z^2} \text{ and } \beta_2 = \frac{e^{-R_e\int_z^{z-\Delta z/2} w\,dz}}{R_e\,\Delta z^2}$$

Equation 4.6 can then be rewritten:

$$u_t = \alpha_1 u_{i,j+1} + \alpha_2 u_{i,j-1} + \beta_1 u_{i+1,j} + \beta_2 u_{i-1,j}$$

$$-(\alpha_1+\alpha_2+\beta_1+\beta_2)\,u_{i,j} \qquad (4.7)$$

The boundary conditions are as follows:

- at $y = 0$, $u = 0$.

- at $z = 0$ and $z = W$, symmetry condition.

- at $y = H$:

$$\frac{\partial u}{\partial y} = \frac{H\,u_\tau^2}{V_e\,\nu}\,\frac{e^{\kappa\left(B-u\frac{u_\tau}{V_e}\right)}}{\kappa}$$

This relation is be easily derived from the logarithmic law.

The initial velocity profile is given by Spalding's law of the wall:

$$y^+ = U^+ + e^{-\kappa B}\left(e^{\kappa U^+} - 1 - \kappa U^+ - \frac{(\kappa U^+)^2}{2} - \frac{(\kappa U^+)^3}{6}\right)$$

Attempts to use other initial conditions did not affect the solution.

Equation 4.7 with the above boundary conditions possesses a steady solution. In reality, of course, the three-dimensional velocity profile is strongly inflexional, both in the normal and in the spanwise direction. This inflexional profile gives rise to an instability (Swearingen and Blackwelder, 1986), which is often believed to initiate the bursting sequence. However, the instability takes place at a distance of about 20 wall units from the wall. Since the assumptions used in the derivation of the model limit its validity to the viscous sublayer, i.e., well below the instability region, it seems natural, as a first approximation, to consider only the steady-state solution of equation 4.7.

Equation 4.7 was solved on the VAX computer of the Garfield Thomas Water Tunnel. The L^2-norm of the residue was less than 10^{-10}. The solution is plotted on figure 28. The iso-velocity lines are seen to be lifted away from the wall between the two vortices, whereas high velocity fluid is pushed toward the wall on their outer sides.

As in the previous section, applying spanwise averaging allows us to compute the statistics of the streamwise velocity as a function of the distance from the wall. The mean velocity distribution thus found is shown on figure 8. The agreement with both experimental and empirical results is very good. Figure 10 shows the distribution of turbulence intensity. The slope at the wall is accurately predicted, and the peak slightly above $y^+ = 15$ is also provided by the model.

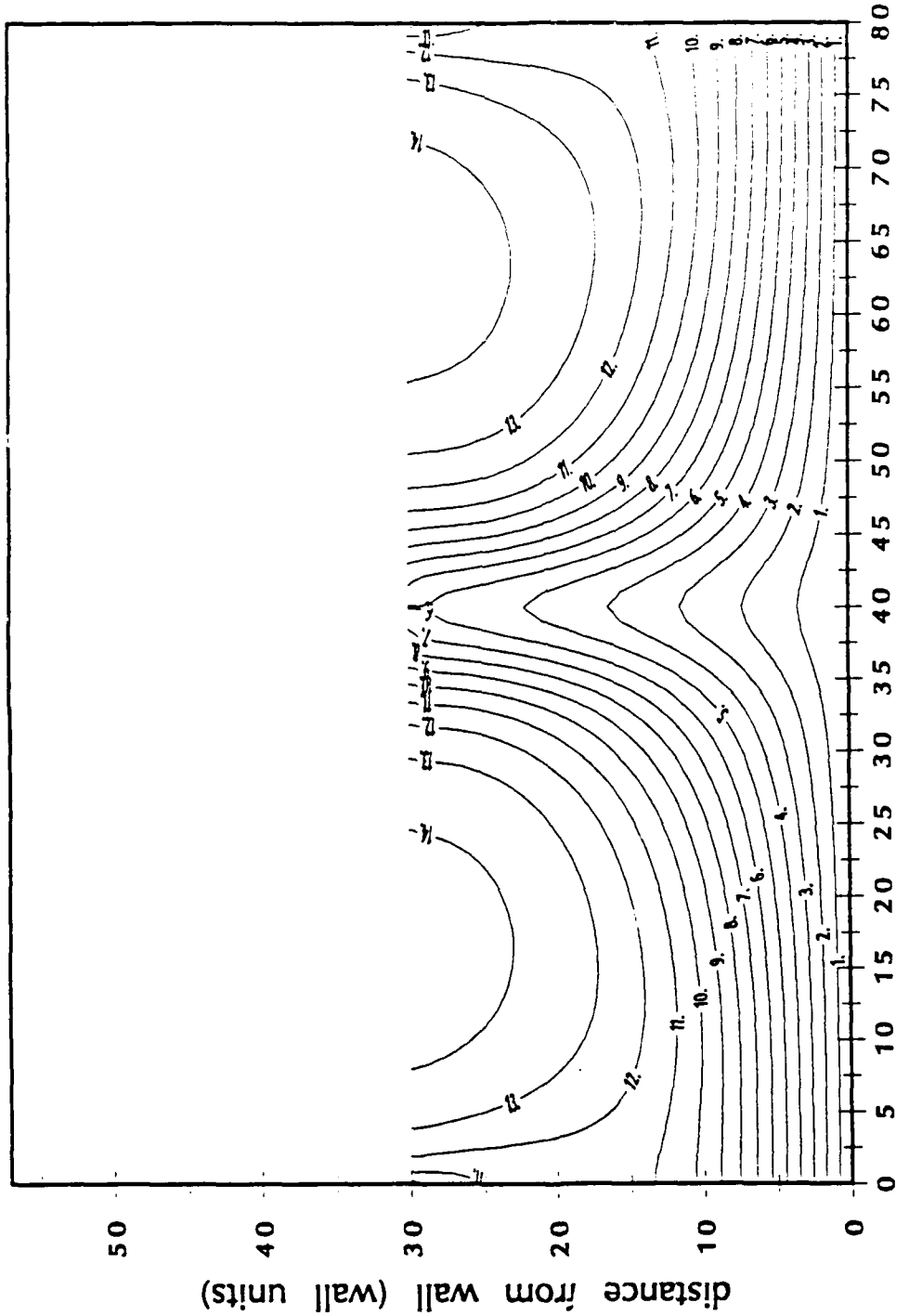

FIGURE 28
Contour Plot of Streamwise Velocity Distribution
Solution of Equation (4.7)

The Reynolds stress distribution is plotted on figure 15 and compared with experimental and empirical data. The model performs very well in the viscous sublayer. Beyond y^+ =12, it markedly overpredicts the Reynolds stress. As noted before, the physics of the flow in the buffer layer is not represented in the model. The random part of the motion, which becomes stronger away from the wall, is also absent from the model.

The next step of this analysis is to look at the value of the correlation coefficient R_{12} for zero streamwise separation and non-zero radial separation. The form of the model makes this task trivial. Indeed, it can be shown simply that the correlation coefficient R_{12} calculated using this model is independant of the radial separation. Recall that the radial component of velocity $v(z,y)$ is separable in two parts:

$$v(z,y) = T(y)cos\left(\pi\frac{z}{W}\right)$$

Then:

$$R_{12}(y;\Delta y) = \frac{\int_0^{2W} u(z,y)v(z,y+\Delta y)\,dz}{\left(\int_0^{2W} u'^2(z,y)\,dz\right)^{1/2}\left(\int_0^{2W} v^2(z,y)\,dz\right)^{1/2}}$$

Substituting the separable form of v, one finds:

$$R_{12}(y;\Delta y) = C\,\frac{\int_0^{2W} u(z,y)\,cos\left(\pi\frac{z}{W}\right)\,dz}{\left(\int_0^{2W} u'^2(z,y)\,dz\right)^{1/2}}$$

where C is a constant. This expression is thus independant of the radial separation Δy.

This result is obviously inaccurate far from the wall, but close examination of the correlation maps shows that for small radial separations, the correlation coefficient varies little when the fixed probe is close to the wall. Based on these observations, we can hypothetize that R_{12} in general tends to a non-zero constant as it approaches the wall.

4.4 Conclusion

With very little quantitative input, the model presented in this chapter was able to reproduce accurately many of the features of the wall region. These results reinforce the picture of the wall region suggested by Bakewell (1966), Kline et al. (1967), and many others. The presence of pairs of counter-rotating vortices is enough to explain the form of the single-point statistics in the wall region.

Chapter 5

CONCLUSIONS AND RECOMMENDATIONS FOR FURTHER STUDIES

5.1 Summary

Measurement of the two-point correlation $R_{12}(y; \Delta x, \Delta y)$ has been made in a fully developed turbulent pipe flow at a Reynolds number slightly below 9000. The high viscosity of glycerine allowed a detailed investigation of the near-wall region. To accomplish the measurements, an LDV system was constructed in which the streamwise velocity was measured by a forward scatter system and the radial velocity was measured by a fiber-optics, backscatter system.

Measurements of the one-point velocity statistics were in excellent agreement with previous investigations of the wall region. The two-point correlation measurements are new, since previous investigators were not able to measure R_{12} in the wall region. The effect of velocity bias on R_{12} was examined, and was found to be small in the conditions of this experiment. A simple model of the flow based on previous experimental results was devised.

5.2 Conclusions

Our results show the existence of elongated structures in the near-wall region, typically a few hundred wall units in length. These structures were found to fill the entire wall region up to $y^+ = 64$. They are inclined at an angle to the wall. The structures close to the wall lie almost parallel to it, while those away from the wall are at a steeper angle.

The correlation contours can not be explained by the presence of two-dimensional structures lying in the plane of the contour maps. The fact that the correlation coefficient is maximum for a non-zero separation distance can only be explained by the presence of three-dimensional structures. A simple explanation, in agreement with previous studies of the wall region, suggests the existence of horseshoe vortices in the wall region. These structures dominate the wall region, with a correlation coefficient between the streamwise and the radial velocity which can be as large as 60%. The interaction between the tip of the vortex and the wall induces the vortex tip to move away from the wall. At the same time, the horseshoe vortex induces a flux of fluid between its legs, which produces strong fluctuations both in the streamwise and radial velocity components. The correlation measurements do not reveal whether this motion is away or toward the wall. Previous studies, however, (e.g., Willmarth and Lu, 1972) show that the distribution is skewed toward the uplift of low velocity fluid from the wall. This observation thus corresponds to a motion of the vortex tip away from the wall. This three-dimensional motion results in a large value of the correlation coefficient R_{12} when the probe measuring the streamwise velocity is between the legs of the vortex, and the probe measuring the radial velocity is at its tip.

The maximum value of the correlation appears for positions of the fixed probe from $y^+ = 9$ to $y^+ = 12$ and positions of the moving probe around $y^+ = 25$. Following the previous interpretation, the location of the maximum value of the correlation is also that of the vortex tip. In this region, the strong mean velocity gradient present in the sublayer, which has strengthened the wall vortices by stretching, is becoming much weaker. It thus loses its ability to counteract viscous forces and the vortices begin to weaken. It is of interest to note that

the corresponding position of the fixed probe, slightly above $y^+ = 10$, is also equal to the position of maximum production of turbulent kinetic energy.

The value of the correlation for zero separation—a non-dimensionalized form of the Reynolds stress—is smaller than the maximum value of the correlation coefficient. It thus appears that the Reynolds stress is just a by-product of the horseshoe vortices. Application of the Biot-Savart law (e.g., Perry and Chong, 1982) would seem more relevant here than direct modeling of the Reynolds stress. In particular, one-point turbulence models, which have been built on data from homogeneous turbulent flows, do not seem appropriate in the near-wall region.

To test the interpretation of the two-point velocity correlation, a simple deterministic model of the flow in the near-wall region was devised. The flow in the cross-plane was modeled as a pair of counter-rotating vortices. The convective terms were dropped in the v- and w- momentum equations. Exact analytical expressions were thus obtained for the spanwise and normal velocity. These expressions were substituted in the streamwise momentum equation from which all nonlinear terms had been dropped. This equation for the streamwise velocity was solved numerically. Based on the observations by Kline et al. (1967) that the spanwise location of the streaks is random, statistics were constructed by using spanwise averaging. One point statistics, including all first-order and second order statistics were calculated and agreement with experimental data is excellent as far as 20 wall units from the wall. These results thus support the picture of the counter-rotating vortices embedded in the near-wall region.

These findings are of fundamental interest for the understanding of the processes of energy transfer in the wall region. The Reynolds stress term $-\rho\overline{uv}$ appearing in the Reynolds-averaged equations is usually interpreted as

a transport term, but there is no rationale for its presence, except the academic argument that it is the result of averaging the nonlinear Navier-Stokes equations. The approach we have followed in this study allows us to give a precise physical meaning to the Reynolds stress. We have been able to identify the eddies which carry the momentum across the wall region, and to understand the way these eddies affect the one-point statistics.

5.3 Recommendations for further studies

This study has been carried out at one particular value of the Reynolds number. It would be interesting to study the effect of the Reynolds number on the structures found in the wall region. Presumably, the scaling of the bursting frequency with inner variables tends to show that these eddies scale on inner variables. However, one should be cautious with using arguments implicitely based on the Taylor hypothesis, and this claim should be verified experimentally.

The question of the origin of the horseshoe vortices is also of fundamental interest. Several theories exist. Some of them attribute their generation to the pressure field from the flow in the outer region. Others see them as a secondary instability of the flow in the buffer layer. The role of pressure in the generation process should be investigated in detail. Time-space correlations of pressure-velocity in the viscous sublayer may reveal interesting features of the flow.

The role of the horseshoe vortices in the near-wall turbulent processes seems to be considerable. It would therefore be of particular interest to study their dynamics. It has been suggested that the flow in the wall region lies on a low-dimensional attractor (Aubry et al., 1988). There are good arguments supporting this hypothesis. The most convincing argument may be the existence

scale, energetic structures, which tends to agree with a deterministic picture of the flow. Inner scaling of the bursting frequency also supports this hypothesis. Experimental studies, using the techniques developed for the study of low-dimensional dynamical systems are necessary to clarify these ideas.

Turbulence control and drag-reduction are two areas of great technological interest. Although some success has been achieved in the control of free shear layers, equivalent success in wall bounded flows is not likely in the foreseeable future. In the area of drag reduction, in spite of good practical results—drag reduction of almost 90% have been obtained in pipes—our understanding of the phenomena is still very limited. Obviously, our ability to control or manipulate turbulent boundary layers depends crucially on our ability to understand how turbulence is generated in the wall region. As in free shear flows, experiments where the turbulent boundary layer is manipulated carefully could allow us to learn more about the turbulent processes, and in particular the flow in the near-wall region.

REFERENCES

Accarlar, M.S. and Smith, C.R. 1987 A Study of Hairpin Vortices in a Laminar Boundary Layer. Part 1: Hairpin Vortices Generated by a Hemisphere Protuberance. *J. Fluid Mech.* **175**, 1.

Adrian, R.J. and Earley, W.L. 1975 Evaluation of LDV Performance Using Mie Scattering Theory. *Minnesota Symposium on Laser Anemometry*, University of Minnesota.

Alfredsson, A.V. and Johansson, P.H. 1984 Time Scales in Turbulent Channel Flow. *Phys. Fluids* **10**, 1974.

Aubry, N., Holmes, P., Lumley, J.L. and Stone, E. 1986 The Dynamics of Coherent Structures in the Wall Region of a Turbulent Boundary Layer. *J. Fluid Mech.* **192**, 115.

Azab, K.A. and McLaughlin, J. 1987 Modeling the Viscous Wall Region. *Phys. Fluids* **30-8**, 2362.

Bakewell, H.P. Jr. 1966 An Experimental Investigation of the Viscous Sublayer in a Turbulent Pipe Flow. Ph. D. Thesis, The Pennsylvania State University.

Blackwelder, R.F. and Haritonidis, J.H. 1983 Scaling of the Bursting Frequency in Turbulent Boundary Layers. *J. Fluid Mech.* **132**, 87.

Blackwelder, R.F. and Kaplan, R.E. 1976 On the Structure of the Turbulent Boundary Layer. *J. Fluid Mech.* **76-1**, 89.

Bradshaw, P. 1978 Discussion of R.S. Brodkey's Paper, *Coherent Structures of Turbulent Boundary Layers*, Ed. C.R. Smith and D.E. Abbott.

Brown, J.L. Jr 1960 Mean-Square Truncation Error in Series Expansion of Random Functions. *J. SIAM*, **8**, 1.

Buchhave, P. 1975 Biasing Errors in Individual Particle Measurements with the LDA Counter Signal Processor. *The Accuracy of Flow Measurements by Laser Doppler Methods*, Proc. LDA Symposium, Copenhagen.

Cantwell, B.J. 1981 Organized Motion in Turbulent Flow. *Ann. Rev. Fluid Mech.* **13**, 457.

Chapman, D.R. and Kuhn, G.D. 1986 The Limiting Behaviour of Turbulence near a Wall. *J. Fluid Mech.* **170**, 265.

Comte-Bellot, G. 1963 Contribution à l'Etude de la Turbulence de Conduite. Ph. D. Thesis. Université de Grenoble, France.

Corino, C.R. and Brodkey, R.S. 1969 A Visual Investigation of the Wall Region in Turbulent Flow. *J. Fluid Mech.* **37-1**, 1.

Dimotakis, P.F. 1976 Single Scattering Particle Laser Doppler Measurements of Turbulence. *AGARD Symp. on Non-intrusive Instrumentation in Fluid Flow Research*, Saint-Louis, France.

Durst, F., Keck, T., Kleine, R. 1985 Turbulence Quantities and Reynolds Stress in Pipe Flow of Polymer Solution. *International Conference on Laser Anemometry - Advances and Applications*, Manchester, UK.

Eckelmann, H. 1974 The Structure of the Viscous Sublayer and the Adjacent Wall Region in a Turbulent Channel Flow. *J. Fluid Mech.* **65-3**, 439.

Edwards, R.V. 1981 A New Look at Particle Statistics in Laser-Anemometer Measurements. *J. Fluid Mech.* **105**, 317.

Einstein, H.A. and Li, H. 1956 The Viscous Sublayer along a Smooth Boundary. *J. of the Eng. Mech. Div. of the ASCE* 82-2, paper 945.

Goldshtik, M.A. 1982 *Structural Turbulence.* Institute of Thermophysics, Novossibirsk.

Grant, H.L. 1958 The Large Eddies of Turbulent Motion. *J. Fluid Mech.* **4-2**, 149.

Hanratty, T.J. 1956 Turbulent Exchange of Mass and Momentum with a Boundary. *AIChe J.* **2-3**, 359.

Harris, V.G., Graham, J.A.H. and Corrsin, S. 1977 Further Experiments in Nearly Homogeneous Turbulent Shear Flow. *J. Fluid Mech.* **81-4**, 657.

Hatziavramidis, D.T. and Hanratty, T.J. 1978 The Interpretation of the Viscous Wall Region as a Driven Flow. *Conference on Coherent Structures of Turbulent Boundary Layers*, Ed. C.R. Smith and D.E. Abbott.

Head, M.R. and Bandyopadhyay, P. 1981 New Aspects of Turbulent Boundary Layer Structure. *J. Fluid Mech.* **107**, 297.

Herzog, S. 1986 The Large Scale Structure in the Near-wall Region of Turbulent Pipe Flow. Ph. D. Thesis, Cornell University.

Hinze, J.O. 1955 Fundamentals of the Hydrodynamic Mechanism of Splitting in Dispersion Processes, *AIChe J.* **1**, 289.

Jang, P.S., Benney, D.J. and Gran, R.L. 1984 On the Origin of Streamwise Vortices in a Turbulent Boundary Layer. *J. Fluid Mech.* **169**, 109.

Johansson, A.V. and Alfredsson P.H. 1981 On the Structure of Turbulent Channel Flow. *J. Fluid Mech.* **122**, 295.

Kim, J. 1983 On the Structure of Wall-Bounded Turbulent Flows. *Phys. Fluids* **26**, 2088.

Kim, H.T., Kline, S.J. and Reynolds, W.C. 1971 The Production of Turbulence near a Smooth Wall in a Turbulent Boundary Layer. *J. Fluid Mech.* **50-1**, 133.

Klebanoff, P.S. 1954 Characteristics of Turbulence in a Boundary Layer with Zero Pressure Gradient. *N.A.C.A. Tech. Note*, no. 3178.

Kline, S.J., Runstadler, P.W. 1959 Some Preliminary Results of Visual Studies of the Flow Model of the Wall Region of the Turbulent Boundary Layer. *Trans. ASME (Ser. E)* **2**, 166.

Kline, S.J. Reynolds, W.C., Schraub, F.A., and Runstadler, P.W. 1967 The Structure of Turbulent Boundary Layers. *J. Fluid Mech.* **30-4**, 741.

Kolmogorov, A.N. 1941 The Local Structure of Turbulence in Incompressible Flows for Very Large Reynolds Number. *C.R. Acad. Sci. USSR* **30**, 301.

Landahl, M.T. 1986 Theoretical Modelling of Coherent Structures in Wall Bounded Shear Flows. *Proceedings of the 1986 Symposium on Turbulence in Liquids*, University of Missouri-Rolla.

Laufer, J. 1954 The Structure of Turbulence in Fully Developed Pipe Flow. *N.B.S. Report*, no. 1174.

Lesieur, M. 1986 *Turbulence in Fluids: Stochastic and Numerical Modelling.* Martinus Nijhoff Ed., Kluwer Academic.

Lu, S.S. and Willmarth, W.W. 1973 Measurements of the Structure of the Reynolds Stress in a Turbulent Boundary Layer. *J. Fluid Mech.* **60-3**, 481.

Luchik, T.S. and Tiederman, W.C. 1987 Timescale and Structure of Ejections and Bursts in Turbulent Channel Flow. *J. Fluid Mech.* **174**, 529.

Luchik, T.S., Walker, D.T., Tiederman, W.G.1985 Injection of Drag Reducing Additives into Turbulent Flows. *Annual Report of the School of Mechanical Engineering* Purdue University.

Lumley, J.L. 1967 The Structure of Inhomogeneous Turbulent Flows. *Atmospheric Turbulence and Radio Wave Propagation*, Moscow, 1967.

Lumley, J.L. 1977 Drag Reduction in Two Phase and Polymer Flows. *Phys. Fluids* **10-2**, 64.

McLaughlin, D.K. and Tiederman, W.G. 1973 Biasing Correction for Individual Realization of Laser Anemometer Measurements of Turbulence, *Phys. Fluids* **16**, 2082.

Moin, P. 1984 Probing Turbulence via Large Eddy Simulation. *Invited Paper, AIAA 22nd Aerospace Meeting*, Reno, Nevada.

Moin, P. and Kim, J. 1982 Numerical Investigation of Turbulent Channel Flow. *J. Fluid Mech.* **118**, 341.

Nagib, H.M. and Guezennec, Y.G. 1986 On the Structure of Turbulent Boundary Layers. *Proceedings of the 1986 Symposium on Turbulence in Liquids*, University of Missouri-Rolla.

Neti, S, Clark, W. 1979 On-Axis Velocity Component Measurement with Laser Velocimeters. *AIAA J.* **17**, 1013.

Orszag, S.A. and Patera, A.T. 1984 Secondary Instability of Wall Bounded Shear Flows. *J. Fluid Mech.* **128**, 347.

Payne, F.R. 1966 Large Eddy Structure of a Turbulent Wake. Ph. D. Thesis, The Pennsylvania State University.

Perry, A.E. and Chong, M.S. 1982 On the Mechanism of Wall Turbulence. *J. Fluid Mech.* **119**, 173.

Rao, K.N., Narasimha, R. and Badri-Narayanan, M.A. 1971 The Bursting Phenomenon in a Turbulent Boundary Layer. *J. Fluid Mech.* **48-2**, 339.

Reynolds, A.A. 1956 *The Structure of Turbulent Shear Flows.* Cambridge University Press.

Sabot, J. 1976 Etude de la Coherence Spatiale et Temporelle de la Turbulence Etablie en Conduite Circulaire, Ph. D. Thesis, Université Claude Bernard de Lyon.

Schlichting, H. 1979 *Boundary Layer Theory.* McGraw-Hill, New York.

Sirovich, L. and Rodriguez, J.D. 1987 Coherent Structures and Chaos: A Model Problem. *Phys. Lett. A* **120**, 5.

Sirovich, L. 1987 Turbulence and The Dynamics of Coherent Structures Part 1: Coherent Structures, Part 2: Symmetries and Transformations, Part 3: Dynamics and Scaling. *Quart. Appl. Math.* **XLV**, 3.

Spalding, D.B. 1961 A Single Formula for the Law of the Wall. *J. of Appl. Mech.* **28**, 455.

Sternberg, J., 1962 A Theory for the Viscous Sublayer of a Turbulent Flow. *J. Fluid Mech.* **13**, 135.

Swearingen, J. and Blackwelder, R.F. 1987 The Growth and Breakdown of Streamwise Vortices in the Presence of a Wall. *J. Fluid Mech.* **182**, 255.

Taylor, G.I. 1915 Eddy Motion in the Atmosphere. *Philos. Trans. R. Soc. London*, **Ser. A 215**, 1.

Tennekes, H. and Lumley, J.L. 1972 *A First Course in Turbulence.* MIT Press

Thermo-Systems Inc., 1982 *System 9100-10 5 Beam, 3 Component Laser Doppler Velocimeter Instruction Manual.*

Thermo-Systems Inc., 1982 *Model 1980-B Counter-type Signal Processor Instruction Manual.*

Townsend, A.A. 1956 *The Structure of Turbulent Shear Flow.* Cambridge University Press.

Willmarth, W.W. and Lu, S.S. 1972 Structure of the Reynolds Stress near the Wall. *J. Fluid Mech.* **55-1**, 65.

Willmarth, W.W. 1978 Survey of Multiple Sensor Measurement and Correlations in Boundary Layers. *Coherent Structures of Turbulent Boundary Layers*, Ed. C.R. Smith and D.E. Abbott.

Willmarth, W.W. and Sharma, L.K. 1984 Study of Turbulent Structure With Hot-Wires Smaller than the Viscous Length. J. Fluid Mech. **142**, 121.

White, F.M., 1974 *Viscous Flow.* McGraw-Hill, New York.

APPENDIX A

THE LDV SYSTEM

A.1 The Fixed Probe System

A.1.1 Operating Principle

The three-component LDV system of the Thomas Garfield Water Tunnel is a standard Thermo-Systems Inc. two-colour, five-beam backward-scatter system. Data acquisition and reduction is accomplished through three counter-processors linked to an IBM PC-AT. We use the blue line and the green line of an 8 W Argon-ion laser from Spectra-Physics.

The multi-line Argon laser beam is separated into a blue beam (488 nm) and a green beam (514.5 nm) with a pair of dispersion prisms. The blue beam is further split into two beams for the measurement of the streamwise velocity component, while the green beam is split into three beams for the measurement of the remaining two orthogonal components. The five beams are focused to the measurement point using a single lens.

The two blue beams lie in the horizontal plane. In order to remove directional ambiguity from the measurement, one of the beams is frequency-shifted by passing it through a 40 MHz Bragg cell. Therefore the signal generated by a particle passing through the control volume has a frequency of 40 MHz $\pm f_{D1}$, where f_{D1} is the Doppler frequency corresponding to the streamwise velocity of the particle:

$$f_{D1} = \frac{u_1}{d_1}$$

and d_1 is the fringe spacing. The output from the photomultiplier is passed through an electronic module which removes the 40 MHz part of the signal. Since counter-processors can only identify positive frequencies, further downmixing is necessary. Several frequencies are available between 2 kHz and 10 MHz. We chose the frequency which gave us the highest data rate, i.e. 2 MHz. The downmixed signal was then sent to the counter-processor for burst detection and determination of the Doppler frequency.

The green color is used for the measurement of the circumferential and radial components of velocity. The circumferential component is perpendicular to the optical axis, while the radial component is along the optical axis. The setup for the measurement of the circumferential component is similar to the one used for the measurement of the streamwise component, except that the two beams used for this operation lie in the vertical plane. The top beam is passed through a 60 MHz Bragg cell, while the bottom beam is passed through a 40 MHz Bragg cell. The signal generated by a particle passing through the control volume has a frequency of 100 MHz $\pm$ f_{D2}, where f_{D2} is the Doppler frequency corresponding to the circumferential velocity u_2. The photomultiplier output is passed through an electronic module which removes the 100 MHz part of the signal, downmixes the Doppler frequency with a 2 MHz frequency and sends it to a second counter-processor.

The measurement of the radial component of velocity involves a third green beam, which is aligned with the optical axis of the system. The radial component is measured as the vector difference between the component of velocity given by the combination of the top and center beams, and that given by the center and

bottom beams (A.1). Since the center beam is not frequency-shifted, the signal generated by the combination (top + center) beams has a frequency:

$$f_{tc} = 60 \text{ MHz} + \frac{u_3 \sin(\phi_{tc}/2)}{d_{tc}} \qquad (a.1)$$

where ϕ_{tc} is the angle between the top and center beams, and d_{tc} is the corresponding fringe spacing. Since, when the system is properly aligned, $\phi_{tc} = \phi_{cb} = \phi$, the fringe spacings d_{tc} and d_{cb} are equal to d_3. Therefore the two fringe patterns cause the same Doppler frequency:

$$f_{D3} = \frac{u_3}{d_3} \qquad (a.2)$$

Substitution into equation (a.1) gives:

$$f_{tc} = 60 \text{ MHz} + f_{D3} \sin(\phi/2)$$

Similarly, the signal corresponding to the combination (center + bottom) beams has a frequency:

$$f_{cb} = 40 \text{ MHz} - f_{D3} \sin(\phi/2)$$

The difference between these two signals is:

$$20 \text{ MHz} + 2 f_{D3} \sin(\phi/2) = 20 \text{ MHz} + f \qquad (a.3)$$

This signal is passed through an electronic module which removes the 20 MHz part of the signal, downmixes it with a 2 MHz frequency and sends it to the third counter-processor. Therefore the frequency f seen by the processor is not the Doppler frequency f_{D3}. Combining equations (a.3) and (a.2) yields for the radial component of velocity the following formula:

$$u_3 = \frac{f\, d_3}{2 \sin(\phi/2)}$$

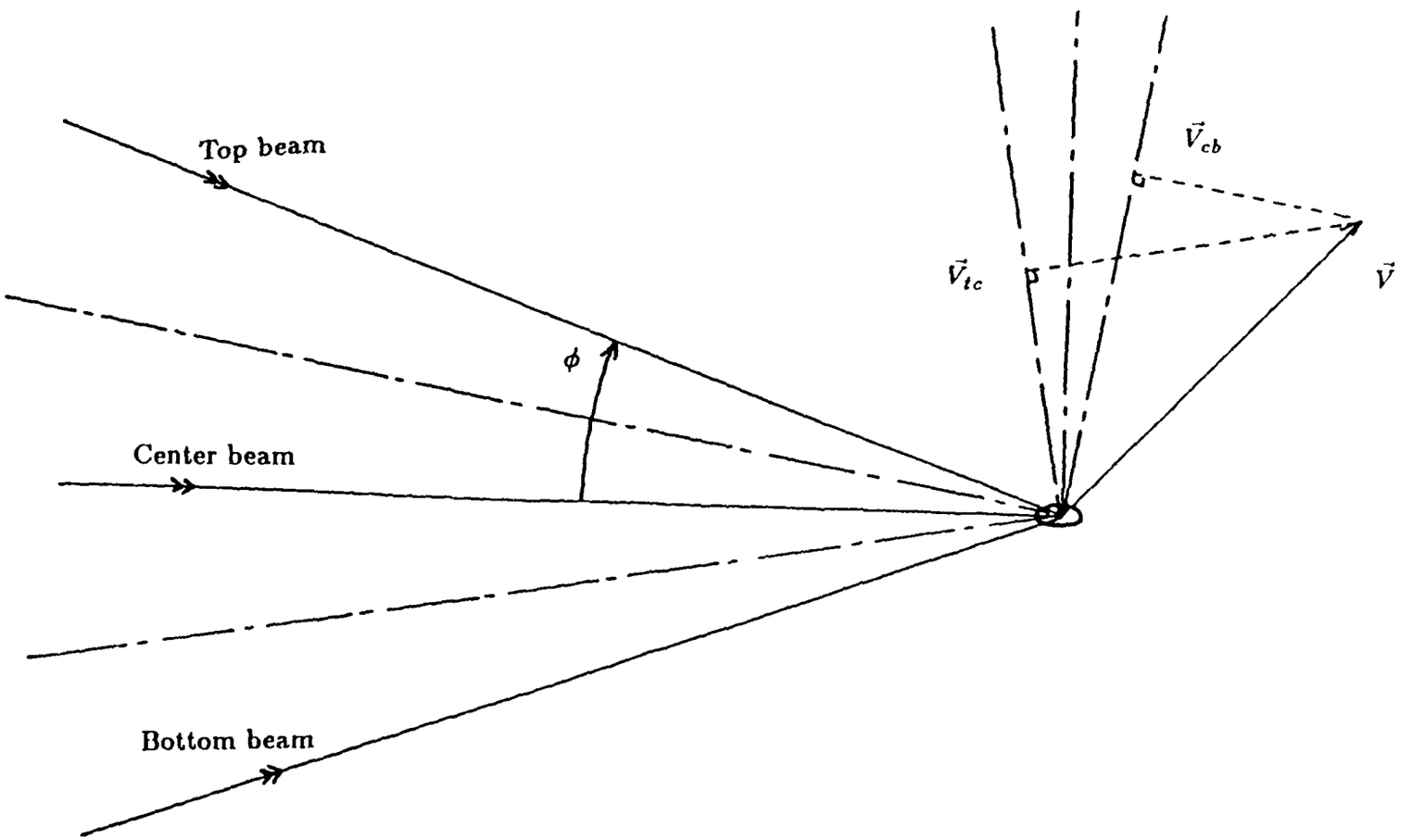

A.1
Beam Setup for the
Measurement of Third Component

For this reason, it is customary to refer to the on-axis velocity measurement as a virtual fringe system, with a virtual fringe spacing d_v equal to:

$$d_v = \frac{d_3}{2\,sin(\phi/2)}$$

A.1.2 Description of the Setup

A complete description of the optical components is given in the TSI system 9100-10 instruction manual. The five beams are focused at the same point using a lens with a 458 mm focal length. In order to reduce the size of the probe and thus to increase the positioning accuracy, a beam expansion module was added to the basic system. The main specifications of the system are the following:

probe diameter..... $d_m = 84\ \mu m$

probe length..... $l_m = 0.61$ mm

beam half-angle..... $\phi = 7.79°$

number of fringes in probe volume... $n = 44$

When the three-component system was moved to or from another facility in the laboratory, the optics had to be tuned to position the beams correctly. Alignment of the beams is a delicate operation, made even more sensitive by the small size of the probe volume. Two days of work were usually required to perform this task.

A.2 The Moving Probe System

In order to measure the two-point velocity correlations, a second velocity probe was necessary. A standard one-component system, coupled to a fiber optics, was used to perform this task. A beam-splitter on the two-component arrangement diverted part of the green beam to this one component system,

which was equipped with a 40 MHz Bragg cell. A TSI coupler was used to focus the beams onto the extremities of two monomode optical fibers. The probe head is a cylinder 135 mm long and 25 mm in diameter. In the probe head, lenses are used to collimate light from the fibers; the collimated laser beams are focused and crossed with a transmitting lens. Scattered light is collected through the same lens and focused onto a multimode fiber. The light from this receiving fiber is coupled into a photodetector. The signal from the photodetector is sent through an electronic downmixing module, then to a counter-processor. The main specifications of the system are the following:

probe diameter.....$d_m = 110\ \mu$m

probe length.....$l_m = 1.6$ mm

beam half-angle.....$\phi = 3.0°$

number of fringes in probe volume... $n = 25$

For the measurement of the two-point correlations, coincidence of the data in the two probe volumes was necessary. To insure coincidence, the counter-processor for the fiber-optics LDV was connected as a third component to the two counter-processors for the two-component LDV. The width of the coincidence time window was adjusted to about 75% of the size of the smallest burst.

A.3 Data Acquisition System

The counter-processors are fully described in the TSI model 1980B counter-type Signal Processor instruction manual. A high-pass and a low-pass filter must be used to eliminate low or high frequency noise from the signal, while a variable gain control is used to amplify the filtered signal into the range of the burst detector. When a burst is detected, the processor measures the transit time taken for a given number of fringe crossings by using a 2 ns resolution clock.

The number of fringe crossings is preselected manually as 2^M, where M can vary between 1 and 5. The transit time is coded in the processor as a number of clock counts. To minimize contributions from background or phase noise, a comparison test is performed between the time for N fringe crossings and the time for $N/2$ (if M = 1,2 or 4) or $5/8\,N$ (if M = 8,16 or 32) fringe crossings. If the ratio of the two times is not equal to the ratio of fringe crossings (i.e. $1/2$ or $5/8$), within a manually preselected percent error, the burst is not accepted. In addition to providing the fringe crossing time, the 1980B processor provides the time between data points (TBD), also coded as a number of clock counts, with one count corresponding to a user selectable number of microseconds from 2^0 to 2^{15}.

These data are transferred in a digital form to an IBM PC-AT microcomputer, via a Direct Memory Access port, using a TSI 1998A Interface. For the transfer, the number of clock counts N_{cc} is coded in 16-bit words. Bits 0 to 11 are occupied by the mantissa N_m, while bits 12 to 15 are occupied by the exponent N_e. Calculation of the number of clock counts involves the following transformation:

$$N_{cc} = N_m\, 2^{N_e}$$

For multicomponent systems, a slave interface can be added to the 1998A interface for each additional channel. This allows data from up to three additional processors to be transferred to the computer. An adjustable coincidence time window in the 1998A interface is used to insure that the data from different processors originated from the same particle.

Data acquisition is controlled from the computer keyboard. The data acquisition software can handle up to 8000 points per channel, with a maximum

of 3 channels. Accepted data are saved on a 30 MB hard-disk, and backed up on high capacity cassettes.

APPENDIX B

SOURCES OF ERROR FOR THE ON THE ON-AXIS COMPONENT OF THE THREE-COMPONENT LDV SYSTEM

B.1 Effect of Misalignment

B.1.1 Instantaneous Velocity

The value of the "on-axis" component of velocity is very sensitive to beam misalignment. In order to provide an estimate of the sensitivity, an analysis was carried out in which only the center beam was assumed to be misaligned. The subscripts t, c and b refer to top, center and bottom beam respectively. The half-angle between the top and bottom beam is called ϕ. Misalignment of the center beam in the horizontal plane is characterized by the angle ψ_h while misalignment in the vertical plane is characterized by the angle ψ_v. The definition and orientation of the axes are shown on B.1.

The unit vectors $\vec{n}_t$ and $\vec{n}_c$ have the following coordinates:

$$\vec{n}_t = (0, sin\phi, cos\phi)$$

and:

$$\vec{n}_b = (0, -sin\phi, cos\phi)$$

The unit vector $\vec{n}_c$ characterizing the direction of the center beam is given by:

$$\vec{n}_c = \frac{1}{\sqrt{sin^2\psi_v + sin^2\psi_h + cos^2\psi_v cos^2\psi_h}}(-sin\psi_v, sin\psi_h, cos\psi_v cos\psi_h)$$

For simplicity, let:

$$\vec{n}_c = (\alpha, \beta, \gamma)$$

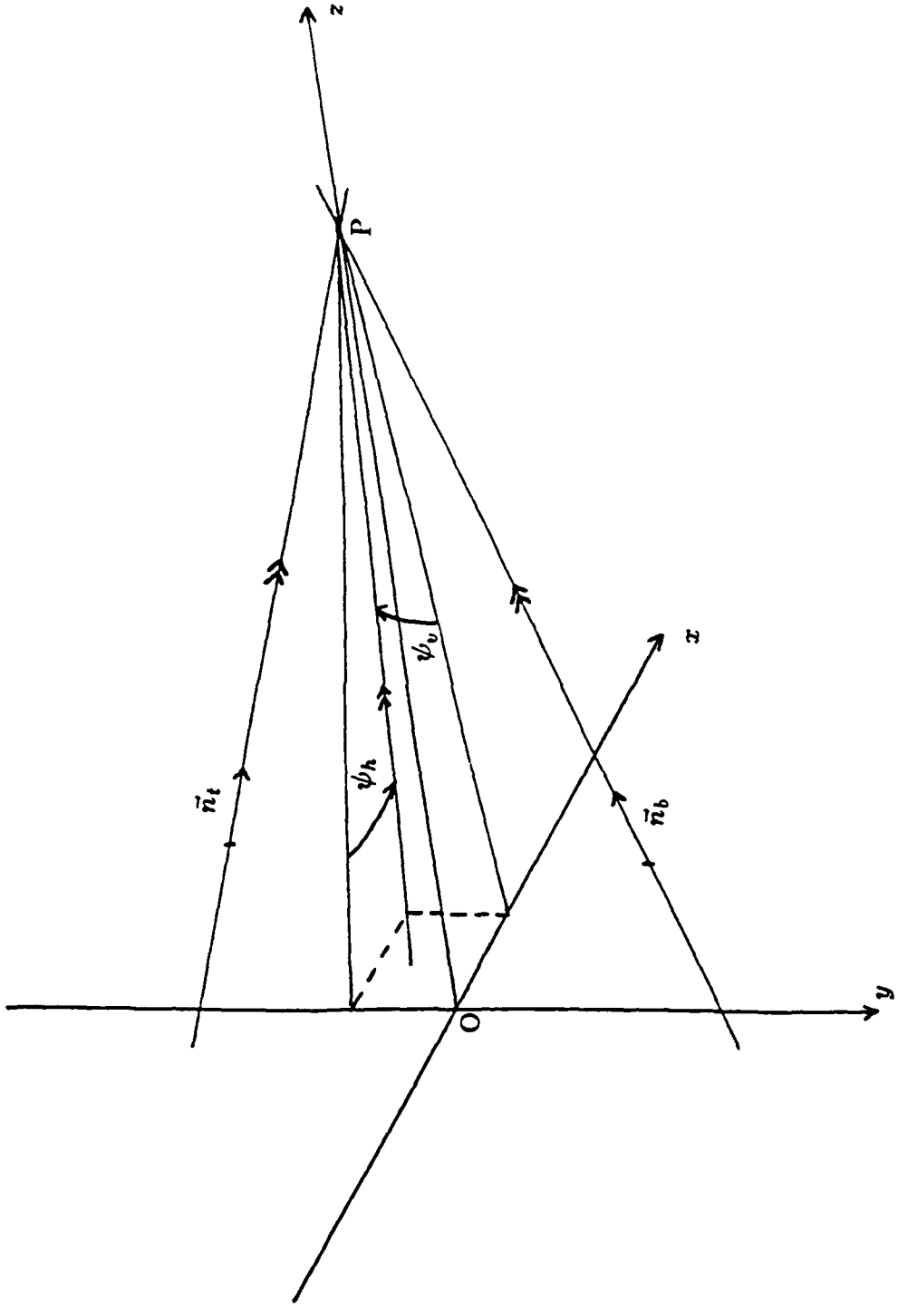

B.1
Definition and Orientation
of the Axis

Then the unit vector $\vec{n}_{tc}$ parallel to the bisector of the top and center beams is:

$$\vec{n}_{tc} = \frac{\vec{n}_c - \vec{n}_t}{||\vec{n}_c - \vec{n}_t||}$$
$$= \frac{1}{\sqrt{\alpha^2 + (\beta - sin\phi)^2 + (\gamma - cos\phi)^2}}(\alpha, \beta - sin\phi, \gamma - cos\phi)$$

Similarly:

$$\vec{n}_{cb} = \frac{1}{\sqrt{\alpha^2 + (\beta + sin\phi)^2 + (\gamma - cos\phi)^2}}(-\alpha, -\beta - sin\phi, -\gamma - cos\phi)$$

Let κ_{ct} be the angle between $\vec{n}_c$ and $\vec{n}_t$. Then:

$$cos\kappa_{ct} = \beta sin\phi + \gamma cos\phi$$

and the interference pattern created by the top and center beams in the probe volume has a fringe spacing d_{ct}:

$$d_{ct} = \frac{\lambda}{2sin(\kappa_{ct}/2)}$$

where λ is the wavelength of the laser beams.

Similarly, let κ_{bc} be the angle between $\vec{n}_b$ and $\vec{n}_c$. Then:

$$cos\kappa_{bc} = -\beta sin\phi + \gamma cos\phi$$

and:

$$d_{bc} = \frac{\lambda}{2sin(\kappa_{bc}/2)}$$

The frequency shift on the top beam being 60 MHz, the signal produced by the combination of the top and center beams has a frequency:

$$f_{ct} = 60 - \frac{\vec{n}_{tc} \cdot \vec{U}}{d_{tc}}$$

where $\vec{U}$ is the velocity of a particle passing through the probe volume. Similarly, the signal produced by the combination of the center and bottom beams has a frequency:

$$f_{bc} = 40 - \frac{\vec{n}_{cb} \cdot \vec{U}}{d_{bc}}$$

since the frequency shift on the bottom beam is 40 MHz.

Therefore the difference between the two signals is:

$$f_{ct} - f_{bc} = 20 - \vec{U} \cdot (\frac{\vec{n}_{tc}}{d_{ct}} - \frac{\vec{n}_{cb}}{d_{cb}})$$

After downmixing this signal with a 20 MHz signal, the frequency f sent to the counter-processor is:

$$f = \vec{U} \cdot (\frac{\vec{n}_{tc}}{d_{tc}} - \frac{\vec{n}_{cb}}{d_{cb}}) \qquad (b.1)$$

For simplicity, let d_v and $\vec{n}_v$ be defined by:

$$\frac{1}{d_v} = ||\frac{\vec{n}_{tc}}{d_{tc}} - \frac{\vec{n}_{cb}}{d_{cb}}|| \qquad (b.2)$$

and:

$$\vec{n}_v = d_v (\frac{\vec{n}_{tc}}{d_{tc}} - \frac{\vec{n}_{cb}}{d_{cb}}) \qquad (b.3)$$

Then:

$$f = \frac{\vec{U} \cdot \vec{n}_v}{d_v} \qquad (b.4)$$

As can be seen, d_v is the virtual fringe spacing, and $\vec{n}_v$ is the direction of the velocity component actually measured.

Let (A, B, C) be the components of $\vec{n}_v$ as defined by equation (b.3). Then from equation (b.4) the measured frequency is:

$$f = \frac{AU + BV + CW}{d_v} \qquad (b.5)$$

If the misalignment of the beam is not taken into account, the on-axis velocity component is computed as:

$$W_m = f\, d_{vm} \qquad (b.6)$$

where the subscript m stands for measured quantities, and d_{vm} is equal to d_v when ψ_h and ψ_v are zero:

$$d_v = \frac{\lambda}{4sin^2(\phi/2)}$$

Substituting for the value of f in equation (b.6) gives:

$$\begin{aligned} W_m &= \frac{AU + BV + CW}{d_v}\, d_{vm} \\ &= \frac{Ad_{vm}}{d_v}U + \frac{Bd_{vm}}{d_v}V + \frac{Cd_{vm}}{d_v}W \end{aligned}$$

Therefore:

$$a = \frac{\partial W_m}{\partial U}(\psi_h, \psi_v) = A\frac{d_{vm}}{d_v}$$

$$b = \frac{\partial W_m}{\partial V}(\psi_h, \psi_v) = B\frac{d_{vm}}{d_v}$$

and

$$c = \frac{\partial W_m}{\partial W}(\psi_h, \psi_v) = C\frac{d_{vm}}{d_v}$$

The coefficients a, b and c have been computed as functions of ψ_h and ψ_v. The algebra is painful but straightforward and will not be given here. We define the coefficients F_1 and F_2 by:

$$F_1 = \sqrt{\frac{1 - \frac{sin\psi_v sin\phi - cos\psi_v cos\psi_h cos\phi}{\sqrt{sin^2\psi_v + sin^2\psi_h + cos^2\psi_v cos^2\psi_h}}}{sin^2\psi_h + (sin\psi_v - sin\phi)^2 + (cos\psi_v cos\psi_h - cos\phi)^2}}$$

$$F_2 = \sqrt{\frac{1 + \frac{sin\psi_h sin\phi - cos\psi_v cos\psi_h cos\phi}{\sqrt{sin^2\psi_h + sin^2\psi_v + cos^2\psi_h cos^2\psi_v}}}{sin^2\psi_v + (sin\psi_h + sin\phi)^2 + (cos\psi_h cos\psi_2 - cos\phi)^2}}$$

Then a, b and c can be expressed as:

$$a = \frac{(F_1 + F_2)sin\psi_v}{\sqrt{2}(1 - cos\phi)}$$

$$b = \frac{(F_1 + F_2)sin\psi_h - (F_1 - F_2)sin\phi}{\sqrt{2}(1 - cos\phi)}$$

and

$$c = \frac{(F_1 + F_2)(cos\psi_v cos\psi_h - cos\phi)}{\sqrt{2}(1 - cos\phi)}$$

When ψ_v and ψ_h are small, a, b and c can be expanded in terms of ψ_v and ψ_h. This results in the following simple expressions:

$$a \simeq \frac{sin\psi_v}{2(1 - cos\phi)}$$

$$b \simeq \frac{sin\psi_h}{2(1 - cos\phi)}$$

and

$$c \simeq \frac{cos\psi_v cos\psi_h - cos\phi}{(1 - cos\phi)}$$

Therefore when ψ_v and ψ_h are small, a, b and c are linear functions of the misalignment angles to first order. As expected, a and b are small, while c is of order 1.

In the present setup, the half-angle ϕ is 7.79°, which gives the following dependancies of a, b and c to the misalignment angles:

$$a \simeq 54.18 sin\psi_v$$

$$b \simeq 54.18 sin\psi_h$$

and

$$c \simeq 108.4(cos\psi_v cos\psi_h - 0.997)$$

As can be seen, the effect of misalignment is not negligible: a misalignment of 0.25° produces a change in the radial component equal to 24% of the streamwise velocity!

B.1.2 Effect on Velocity Statistics

It is also of interest to look at the effect of misalignment on the velocity statistics. The averaging operation being linear, the mean velocity $\overline{w}$ is affected in the same manner as the instantaneous velocity W. However, higher-order moments involving powers of the on-axis component of velocity larger than 1 follow more complicated relations.

The mean part of the on-axis component of velocity is:

$$\overline{w_m} = \overline{au + bv + cw} = a\overline{u} + b\overline{v} + c\overline{w}$$

But $\overline{v}$ and $\overline{w}$ are zero in the pipe flow, so that:

$$\overline{w_m} = a\overline{u}$$

The fluctuating part of the on-axis component of velocity is:

$$w_m = W_m - \overline{w_m} = au + bv + cw$$

The variance of w_m can be evaluated:

$$\overline{w_m^2} = \overline{(au + bv + cw)^2}$$

which yields after some algebra:

$$\overline{w_m^2} = a^2\overline{u^2} + b^2\overline{v^2} + c^2\overline{w^2} + 2ac\overline{uv}$$

A similar calculation gives the expression for the Reynolds stresses:

$$\overline{uw_m} = a\overline{u^2} + c\overline{uw}$$

$$\overline{vw_m} = b\overline{v^2}$$

Equivalent expressions can be found for the third and fourth-order moments. If no other source of systematic error was involved in the measurements, it would be possible to compute the coefficient a from the measurement of the mean velocity alone:

$$a = \frac{\overline{w_m}}{\overline{u}}$$

In a laminar flow, no other coefficient can be deduced. In a turbulent flow, the coefficient b can be computed from the measurement of $\overline{vw_m}$:

$$b = \frac{\overline{vw_m}}{\overline{v^2}}$$

The coefficient c can not be computed directly. However, knowledge of a and b is enough to compute the misalignment angles ψ_h and ψ_v. This in turn allows calculation of c.

B.2 Influence of the Beam Angle on the Accuracy of the On-axis Component

This analysis is based on a study by Neti and Clark (1979) for the on-axis component of a three-component LDV system. Their measurement of the circumferential and on-axis velocity components was achieved by using two pairs of beams of orthogonal linear polarizations.

The present beam setup for the measurement of the circumferential and radial component of velocity is shown on A.1. In the absence of frequency shift, the expressions for the circumferential and on-axis velocity components are:

$$\begin{aligned} v &= V\cos\alpha \\ w &= V\sin\alpha \end{aligned} \qquad (b.7)$$

where α is the angle between the velocity vector $\vec{V}$ and the axis normal to the optical axis of the LDV.

The measured velocities V_1 and V_2 are related to $\vec{V}$ by the relations:

$$\begin{aligned} V_1 &= V cos(\alpha - \phi/2) \\ V_2 &= V cos(\alpha - \phi/2) \end{aligned} \tag{b.8}$$

Eliminating V between (b.7) and (b.8) gives the following expression for w:

$$w = \frac{V_1 - V_2}{2sin(\phi/2)}$$

Assuming that the relative accuracy of V_1 and V_2 is the same, given by $\frac{dV}{V}$, the relative accuracy of the on-axis component is:

$$\begin{aligned} \frac{dw}{w} &= \frac{dV}{V_1 - V_2} \\ &= \frac{dV}{2wsin(\phi/2)} \end{aligned}$$

In the five-beam two-colour setup:

$$dV = dv$$

Therefore:

$$\begin{aligned} \frac{dw}{w} &= \frac{dv}{2wsin(\phi/2)} \\ &= \frac{dv}{v}\frac{v}{w}\frac{1}{2sin(\phi/2)} \end{aligned}$$

In many flows, the order of magnitude of v/w is one. If the beam angle ϕ is small, the previous expression reduces to:

$$\frac{dw}{w} \simeq \frac{1}{\phi}\frac{dv}{v}$$

This shows that the relative uncertainty on the on-axis velocity component is proportional to that for the other components, but more important, it is inversely proportional to the beam-angle. For the on-axis component to have an accuracy of the same order of magnitude as on the other components, the beam angle should be at least 30°. This in turn creates geometrical problems—access through a wind-tunnel window might not be possible—.

In the case of the TSI system, the angle ϕ is 7.79°. Therefore the relative uncertainty on the on-axis component is:

$$\frac{dw}{w} \simeq 9.55 \frac{dv}{v}$$

Thus the relative accuracy on the on-axis component of velocity is found theoretically to be about ten times smaller than for the other components.

APPENDIX C
EFFECT OF VELOCITY BIAS ON MEASUREMENT OF TWO-POINT CORRELATION COEFFICIENT

C.1 Introduction

Since velocity bias was uncovered by McLaughlin and Tiederman in 1973, it has been a subject of controversy. Velocity bias arises in laser Doppler velocimetry because the statistics for the particle arrival times and that for the fluid velocity are not independent. More particles with large velocity are swept past the probe volume than particles with low velocity. Thus velocity statistics calculated directly as averages of particle velocities are skewed towards high values.

Velocity bias has been analyzed in numerous papers, both theoretically and experimentally. McLaughlin and Tiederman (1973) suggested a simple-minded correction factor when the flow is essentially one-dimensional. Dimotakis (1975), Buchhave (1975) and others have given more detailed analyses, taking into account all three components of velocity and the ellipsoidal shape of the probe volume. However, the effect of the bias on two-point correlations has never been considered.

The present analysis is based on a paper by Edwards (1981) who looked at the case of an LDV processor with a fixed sampling rate. This case can be easily extended to the case of a multicomponent system, with a coincidence window of given width $\Delta\tau$.

C.2 Theory

To keep the calculations tractable, a number of assumptions have been made. The major assumption is that the flow we analyze is one-dimensional, with velocity $U = U(x,t)$. This assumption reduces the number of random variables by a factor of three, and avoids the complication introduced by a three-dimensional probe volume.

We measure the velocity at two points A and B and we assume that the two probe volumes are similar. The length of each probe volume is d_m, and the minimum distance that a particle must travel inside a probe volume for a valid measurement is l. The parameter l is sometimes called the effective probe length, and is a function of the frequency shift f_s. If d_f is the fringe spacing, then the relative velocity of the particle with respect to the fringes is:

$$U_{rel} = U + d_f f_s$$

The time between 2 fringe crossings is:

$$\Delta t = \frac{d_f}{U + d_f f_s}$$

and the time to cross the minimum number of fringes N_{min} necessary for validation is:

$$T = \frac{N_{min}\, d_f}{U + d_f f_s}$$

Therefore the minimum distance that the particle must travel for validation is:

$$l = T \times U = \frac{N_{min}\, d_f U}{U + d_f f_s} \qquad \text{(c.1)}$$

In the absence of frequency shifting, we find the classical result that l is independent of U:

$$l = N_{min}\, d_f$$

On the contrary, if the frequency shifting is very large, so that $d_f f_s >> |U|$, then we have:

$$l = \frac{N_{min}|U|}{f_s}$$

The size of the coincidence window $\Delta\tau$ is usually chosen equal to the shortest mean burst duration of the two probes. In the following we will assume that the two mean velocities $\overline{U_A}$ and $\overline{U_B}$ are equal to $\overline{U}$, so that $\Delta\tau$ is unambiguously defined as:

$$\Delta\tau = \frac{d_m}{\overline{U}} \qquad (c.2)$$

We assume that a measurement is made if at least one particle passes through each probe volume during $\Delta\tau$. This assumption neglects all other data rejection devices in the system. If several particles pass in a probe volume during $\Delta\tau$, we assume that only the first one is validated.

Let ρ be the mean concentration of particles per unit length. The particle arrival times follow a Poisson distribution, so that the expected number of particles in any given length L is just ρL. The probability of having at least one particle in L is $(1 - exp(-\rho L))$. The length of fluid swept through l during $\Delta\tau$ is $(|U|\Delta\tau - l)$, since a particle must traverse l to be measured. Therefore the probability of getting one measurement in probe volume A during $\Delta\tau$ is:

$$P_A(U) = \begin{cases} 1 - exp[-\rho(|U|\Delta\tau - l)] & \text{if } |U| > l/\Delta\tau; \\ 0 & \text{otherwise.} \end{cases} \qquad (c.3)$$

As a preliminary discussion of the cause of velocity bias, let us consider the case of a one-dimensional system. The PdF P_A is represented in C.1 (dashed

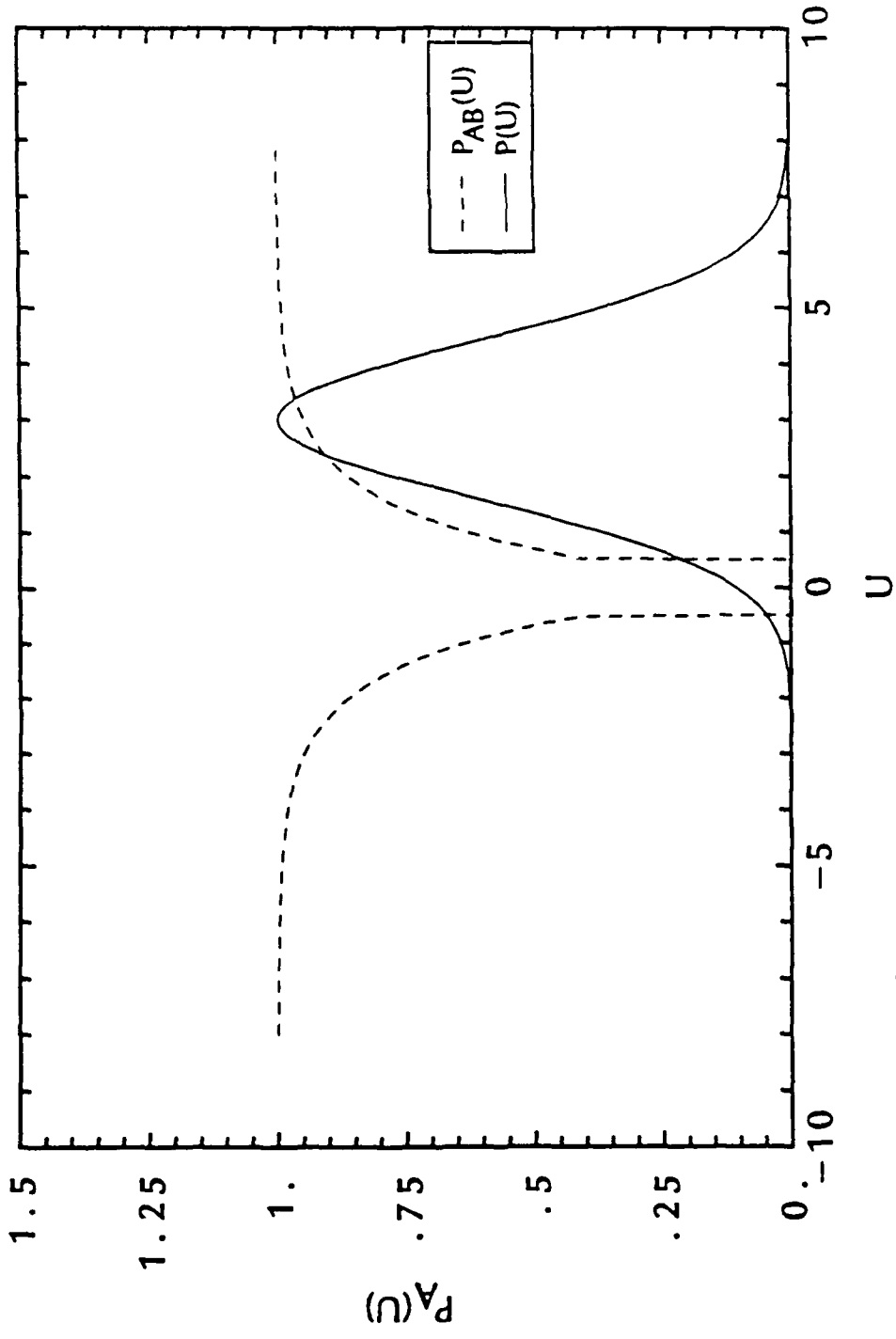

C.1
One-dimensional PdF's
P_{AB} and P

line) together with a velocity PdF (solid line). Velocity bias arises because the probability of measuring a velocity U is given by:

$$P_m(U) = \frac{P(U)\,P_A(U)}{\int_R P(U)\,P_A(U)\,dU}$$

When $P_A(U)$ is close to 1, its effect on $P(U)$ is small. When $P_A(U)$ is small, $P(U)$ is strongly affected. To reduce bias, one thus tries to make $P_A(U)$ as close as possible to 1 wherever $P(U)$ is significantly larger than zero.

Two parameters characterize the PdF P_A: the width w of the bin where P_A is equal to zero, and the rate at which it reaches its asymptotic value 1. Using c.1, we can see that $w = l/\Delta\tau$ is inversely proportional to the frequency shift. Therefore large values of the frequency shift contribute to reduce the dead zone. This phenomenon is usually referred to as fringe bias, and is caused by the fact that particles moving at the velocity of the fringes do not produce any signal. Increasing the frequency shift to values which make the fringe velocity much larger than the particle velocity suppresses this problem. This leads to a practical estimate of the minimum frequency shift to choose: we must choose f_s so that $|U|$ is always greater than $l/\Delta\tau$. Substituting for the value of l given by equation c.1 into equation c.3, we get:

$$f_s > \frac{N_{min}}{\Delta\tau} - \frac{U}{d_f}$$

Therefore a safe choice for the frequency shift would be for example:

$$f_s = 2\left(\frac{N_{min}}{\Delta\tau} - \frac{U_{min}}{d_f}\right)$$

Equation c.3 shows that the rate at which P_A reaches its asymptotic value 1 depends on the particle concentration ρ. If we define the non-dimensional number $n_v = \rho\, d_m$, which represents the average number of particles in the probe volume,

then a high value of n_v corresponds to a high data rate. Equation c.3 shows that when n_v is large, $P_A(U)$ reaches its asymptotic value 1 faster than when it is small. Thus its interaction with the PdF $P(U)$ is reduced and bias is reduced: high data rates diminish the effect of bias. This phenomenon corresponds to velocity bias.

We now assume that the positions of the particles in the fluid are random, so that the particle arrival time statistics for the two probe volumes are independent. The probability of finding at least one particle in each probe volume is:

$$P_{AB}(U_A, U_B) = P_A(U_A)\, P_B(U_B)$$

Consequently the probability of measuring a velocity U_A in probe A and a velocity U_B in probe B is given by:

$$P_m(U_A, U_B) = \frac{P(U_A, U_B)\, P_A(U_A)\, P(U_B)}{\iint_{R^2} P(U_A, U_B)\, P(U_A)\, P(U_B)\, dU_A\, dU_B}$$

where $P(U_A, U_B)$ is the joint PdF of the velocities U_A and U_B, at points A and B respectively.

If $P(U_A, U_B)$ were known, it would be possible to compute $P_m(U_A, U_B)$ and the exact two-point velocity statistics. In practice, this would require the measurement of all three components of velocity at both points, which does not seem feasible for the moment.

In the following, we will assume the form of the joint PdF $P(U_A, U_B)$ and observe the effect of bias on the correlation coefficient. The simplest joint PdF is the bivariate normal PdF. We define u_A and u_B as the instantaneous velocity

fluctuations at A and B, and u'_A and u'_B as their RMS values. Then the bivariate normal PdF $P(U_A, U_B)$ is defined as:

$$P(U_A, U_B) = \frac{1}{2\pi u'_A u'_B (1-r^2)^{1/2}} exp\left[-\frac{\left(\frac{u_A}{u'_A}\right)^2 - 2r\left(\frac{u_A}{u'_A}\right)\left(\frac{u_B}{u'_B}\right) + \left(\frac{u_B}{u'_B}\right)}{2(1-r^2)} \right]$$

where r is the velocity correlation coefficient.

C.3 Discussion

C.2 shows a contour map of the PdF $P_{AB}(U_A, U_B)$ and $P(U_A, U_B)$. As can be seen, many of the features of this plot are similar to those of its one-dimensional version in C.1, and, due to the fact that the two distributions P_A and P_B are independent, the same remarks concerning the effects of particle concentration and frequency shift can be made. The new parameter appearing in this plot is the correlation coefficient r. We now focus our attention on the influence of r on the measured mean velocity and correlation coefficient. In the following, we assume that the frequency shift is large, so that l in the equations for P_A and P_B is neglected.

A program was written to study the effect of the correlation coefficient on bias. The non-dimensional parameters governing the problem are the mean number of particles in each probe volume, the turbulence intensities and the correlation coefficient, i.e., 4 quantities in all. To simplify the presentation, we assumed that the turbulence intensity at both points was the same and equal to 30%, approximately equal to its largest value in a turbulent boundary layer. C.3 shows the mean velocity bias $\Delta U_m = (U_m - U)$ at point A, non-dimensionalized by u'_A, versus the correlation coefficient r, for several values of n_v. The subscript m is used for measured quantities, as opposed to exact quantities appearing

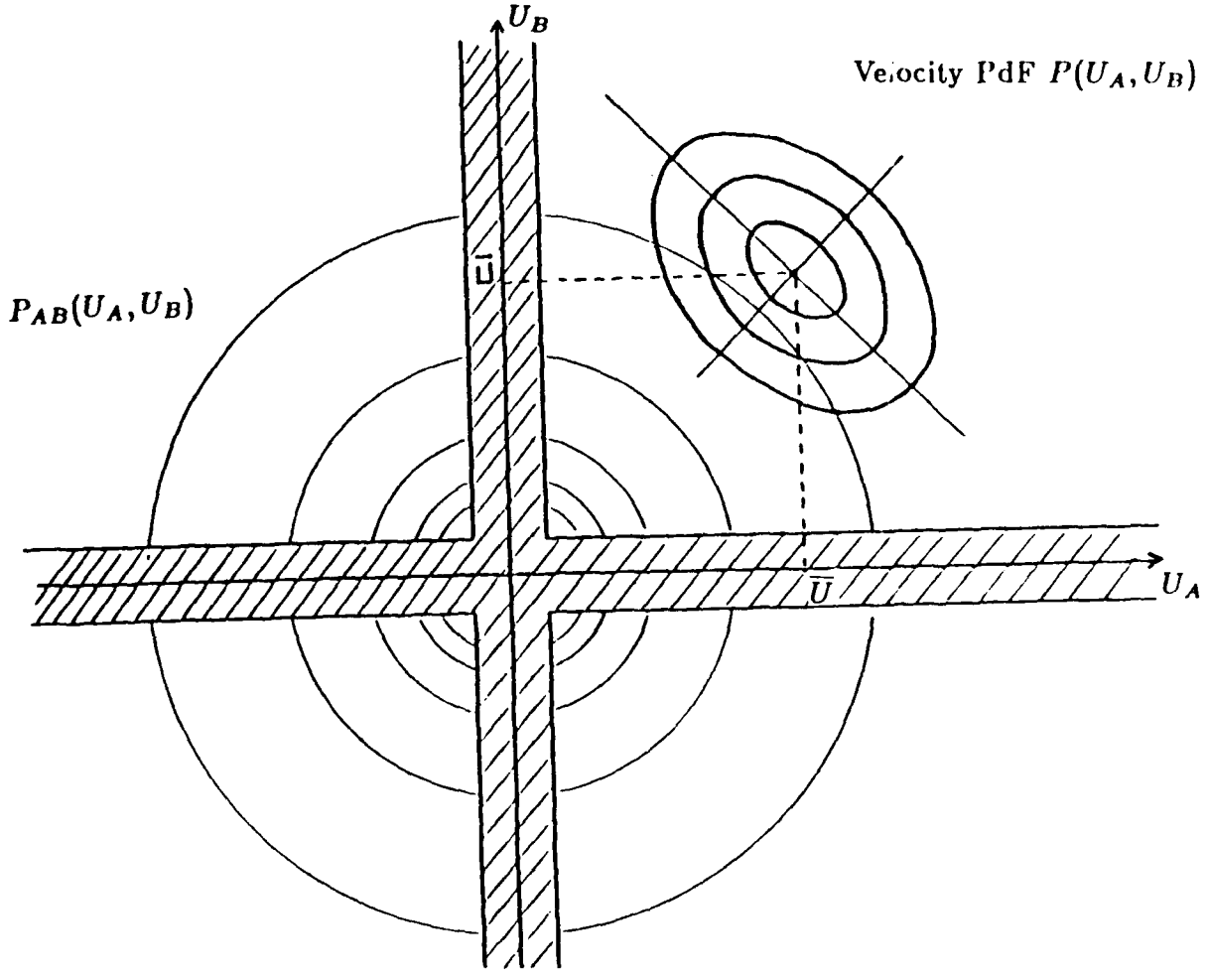

C.2
Two-dimensional Contour Plot
of P_{AB} and P

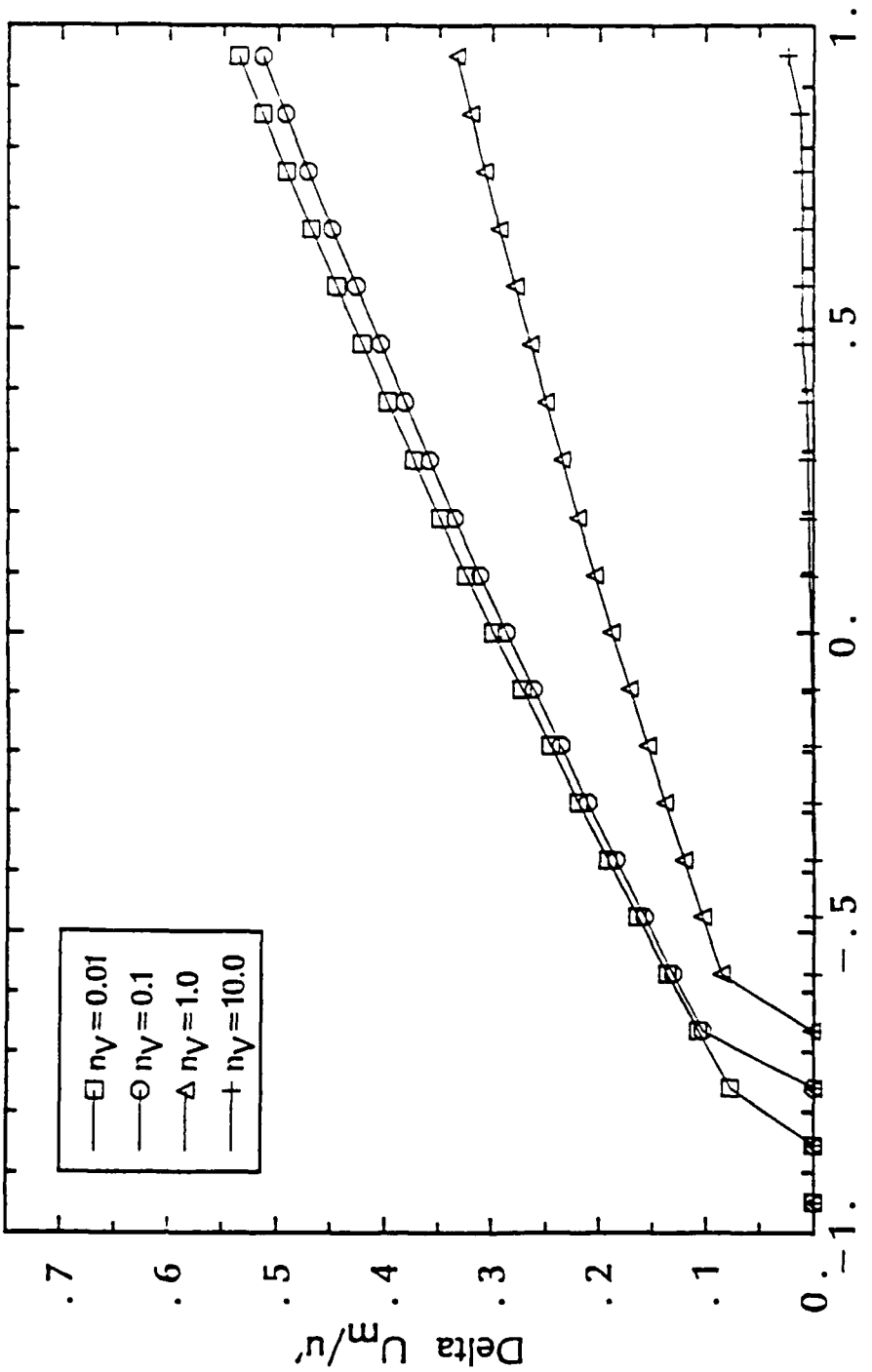

C.3
Influence of velocity bias
on mean velocity

without subscript. C.4 presents the correlation coefficient bias $(r_m - r)$, versus the correlation coefficient r, for several values of n_v.

The numerical results can be interpreted with the help of C.2. The influence of particle concentration on bias is as expected. The mean velocity and the correlation coefficient are barely affected for values of n_V larger than 10. This corresponds to the situation when there is almost always a particle in the probe volume. In this case, the processor is saturated and data acquisition is made at a constant rate. This corresponds to the case where $P_{AB}(U_A, U_B)$ reaches its asymptotic value 1 very fast, and thus interacts very little with the velocity PdF $P(U_A, U_B)$. Note, however, than the situation when there is more than one particle in the probe volume is not desirable if data processing is being made with counter processors.

As the particle concentration is reduced, the bias increases because P_{AB} reaches 1 more slowly and the two distributions P_{AB} and P interact more. Although the calculations in figures C.3 and C.4 indicate that the bias reaches an asymptote for very small values of the particle concentration, these results should be taken with care because they involve numerical integrations of very small quantities (of the order of e^{-10}), and accuracy of the numerical routines may not be sufficient.

The increase of the mean velocity bias with the correlation coefficient is due to the fact that as r increases, the two distributions P and P_{AB} become more closely aligned with each other. When the correlation coefficient is equal to -1, the velocity PdF $P(U_A, U_B)$ lies entirely on the line parallel to the line $U_A = -U_B$, and passing through $(\overline{U}, \overline{U})$. The PdF P is symmetric with respect to the line $U_A = U_B$, like P_{AB}, and the product of the two is also symmetric with respect to

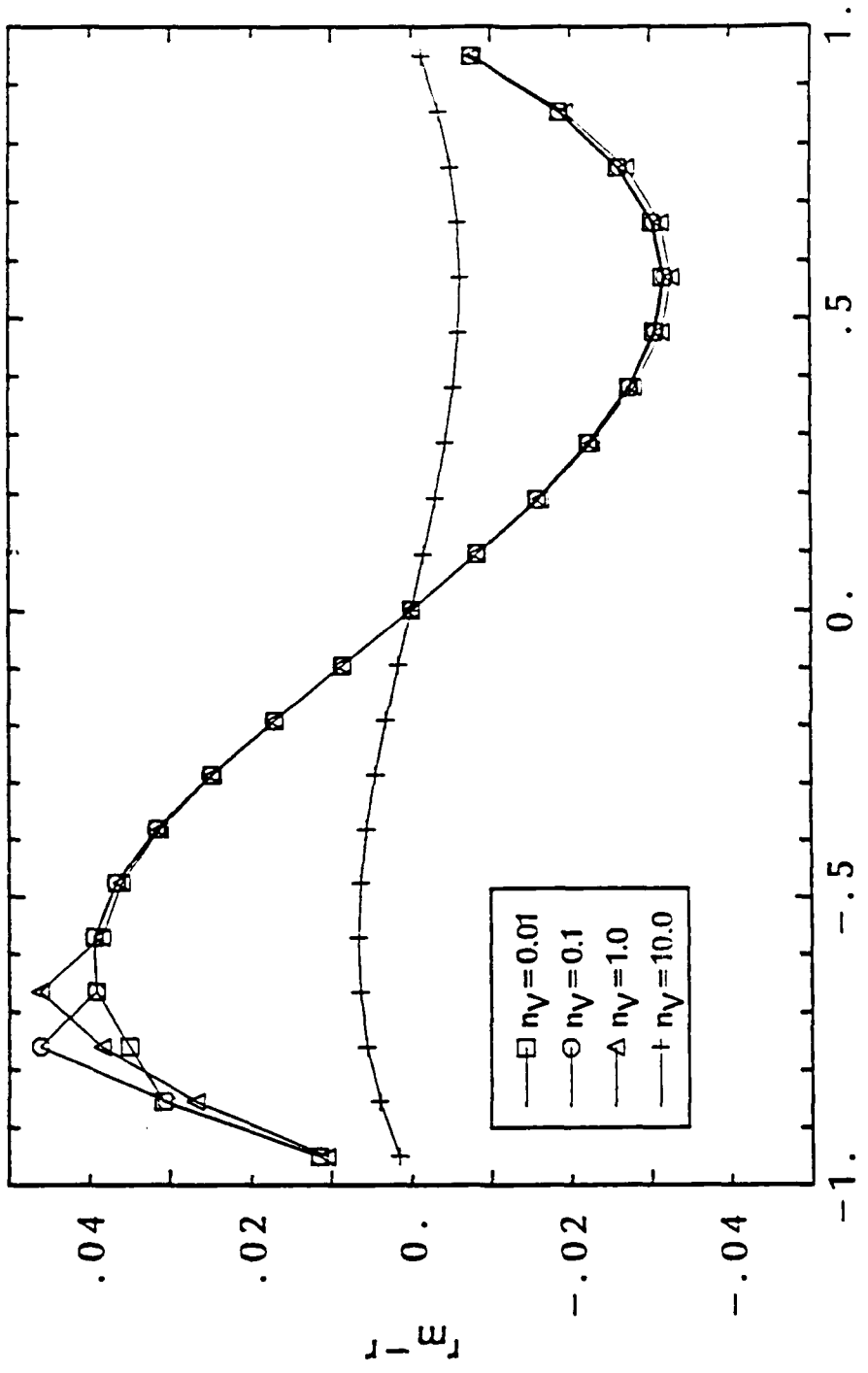

C.4
Influence of velocity bias
on correlation coefficient

this line. Thus the value of the mean velocity is not affected. Physically, this is because the velocity fluctuation at one point is always the exact opposite of that at the other point. Thus when the data rate is low at one point, it is high at the other point, and vice and versa, so that the coincident data rate is a constant on the average, and there is no bias. As the correlation coefficient increases, the PdF P becomes less linear and expands in the direction of the line $U_A = U_B$. Beyond a certain value of the correlation coefficient, the two distributions begin to interact, and bias affects the mean velocity. As r continues to increase, the PdF P_{AB} contaminates the PdF P more. The part of $P(U_A, U_B)$ closer to the origin is more affected than the part away from the origin, so that the mean velocity is pushed away from the origin. ysically, what happens when $r = 1$ is equivalent to what would happen in the one-dimensional case, presented in a previous section.

As can be seen on C.4, the measured correlation coeffficient is not affected by bias at $r = -1$, 0 and 1. At -1 and 1, the PdF P is zero everywhere except in the direction of the lines $U_A = U_B$ or $U_A = -U_B$. Therefore there is no interaction with the PdF P_{AB}. In effect, the PdF is one-dimensional, and multiplication by another PdF leaves it one-dimensional. The correlation coeffiecient therefore remains equal to 1 or -1. The absence of bias on r_m at $r = 0$ is due to the fact that the measured PdF P_m is the product of two two-dimensional PdF's, each with a zero correlation coefficient. Thus it has a correlation coefficient equal to zero. Since the bias is zero for r=1, -1 and 0, it must reach its maximum for intermediate values of the correlation coefficient, around $r = -0.5$ and 0.5. Around, $r = -0.5$, multiplication of P by P_{AB} makes the final distribution leaner in the direction of the line $U_A = -U_B$, thus reinforcing the effect of the correlation coefficient. Around $r = 0.5$, the effect is the same, but this time, it

acts in the direction normal to that characterized by the correlation coefficient, so that r_m is smaller than r.In both cases, the absolute change of the correlation coefficient remains less than 4%.

C.4 Conclusions

It is clear that a high data rate is best for the measurement of the two-point correlation coefficient. This ensure that no bias will affect the results.

If the data rate achieved is small (typically $n_V < 1$), the bias will affect the statistics of the velocity. The effect on the mean velocity can be significant, typically up to half the RMS value of the velocity. The effect on the correlation coefficient remains relatively small. For the case considered in these calculations, the error is not larger than 0.04, which is well within experimental error. The effect is larger for values of the correlation coefficient close to 0.5, but negligible for small values of the correlation coefficient. Thus the general shape of the structures identified by contour plots of the correlation coefficient should not be affected.